NIH Public Access
Author Manuscript
Comput Methods Appl Mech Eng. Author manuscript; available in PMC 2016 February 01.

Published in final edited form as:
Comput Methods Appl Mech Eng. 2015 February 1; 284: 1005–1053. doi:10.1016/j.cma.2014.10.040.

An immersogeometric variational framework for fluid–structure interaction: application to bioprosthetic heart valves

David Kamensky[a], **Ming-Chen Hsu**[b,*], **Dominik Schillinger**[c], **John A. Evans**[d], **Ankush Aggarwal**[a], **Yuri Bazilevs**[e], **Michael S. Sacks**[a], and **Thomas J. R. Hughes**[a]

[a]Center for Cardiovascular Simulation, Institute for Computational Engineering and Sciences, The University of Texas at Austin, 201 East 24th St, Stop C0200, Austin, TX 78712, USA

[b]Department of Mechanical Engineering, Iowa State University, 2025 Black Engineering, Ames, IA 50011, USA

[c]Department of Civil Engineering, University of Minnesota, 500 Pillsbury Drive S.E., Minneapolis, MN 55455, USA

[d]Department of Aerospace Engineering Sciences, University of Colorado at Boulder, 429 UCB, Boulder, CO 80309, USA

[e]Department of Structural Engineering, University of California, San Diego, 9500 Gilman Drive, Mail Code 0085, La Jolla, CA 92093, USA

Abstract

In this paper, we develop a geometrically flexible technique for computational fluid–structure interaction (FSI). The motivating application is the simulation of tri-leaflet bioprosthetic heart valve function over the complete cardiac cycle. Due to the complex motion of the heart valve leaflets, the fluid domain undergoes large deformations, including changes of topology. The proposed method directly analyzes a spline-based surface representation of the structure by immersing it into a non-boundary-fitted discretization of the surrounding fluid domain. This places our method within an emerging class of computational techniques that aim to capture *geometry* on non-boundary-fitted analysis meshes. We introduce the term “immersogeometric analysis” to identify this paradigm.

The framework starts with an augmented Lagrangian formulation for FSI that enforces kinematic constraints with a combination of Lagrange multipliers and penalty forces. For immersed volumetric objects, we formally eliminate the multiplier field by substituting a fluid–structure interface traction, arriving at Nitsche’s method for enforcing Dirichlet boundary conditions on object surfaces. For immersed thin shell structures modeled geometrically as surfaces, the tractions from opposite sides cancel due to the continuity of the background fluid solution space, leaving a penalty method. Application to a bioprosthetic heart valve, where there is a large

© 2014 Elsevier B.V. All rights reserved.

*Corresponding author. jmchsu@iastate.edu (Ming-Chen Hsu).

Publisher's Disclaimer: This is a PDF file of an unedited manuscript that has been accepted for publication. As a service to our customers we are providing this early version of the manuscript. The manuscript will undergo copyediting, typesetting, and review of the resulting proof before it is published in its final citable form. Please note that during the production process errors may be discovered which could affect the content, and all legal disclaimers that apply to the journal pertain.

NIH-PA Author Manuscript
NIH-PA Author Manuscript
NIH-PA Author Manuscript

NIH-PA Author Manuscript

NIH-PA Author Manuscript

NIH-PA Author Manuscript

pressure jump across the leaflets, reveals shortcomings of the penalty approach. To counteract steep pressure gradients through the structure without the conditioning problems that accompany strong penalty forces, we resurrect the Lagrange multiplier field. Further, since the fluid discretization is not tailored to the structure geometry, there is a significant error in the approximation of pressure discontinuities across the shell. This error becomes especially troublesome in residual-based stabilized methods for incompressible flow, leading to problematic compressibility at practical levels of refinement. We modify existing stabilized methods to improve performance.

To evaluate the accuracy of the proposed methods, we test them on benchmark problems and compare the results with those of established boundary-fitted techniques. Finally, we simulate the coupling of the bioprosthetic heart valve and the surrounding blood flow under physiological conditions, demonstrating the effectiveness of the proposed techniques in practical computations.

Keywords

Fluid–structure interaction; Bioprosthetic heart valve; Immersogeometric analysis; Isogeometric analysis; B-splines and NURBS; Nitsche’s method; Weakly enforced boundary conditions; Penalty-based contact

1. Introduction

Heart valves are passive structures that open and close in response to hemodynamic forces, ensuring proper unidirectional blood flow through the heart. At least 280,000 diseased heart valves are surgically replaced annually [1, 2]. By far the most popular surgical replacements are the bioprosthetic heart valves (BHV), which are fabricated from biologically derived materials, with the design goal of mechanical similarity to native valves. Like native valves, BHVs are composed of thin flexible leaflets that are pushed open by blood flow in one direction and closed by flow in the other direction. BHVs have more natural hemodynamics than the older “mechanical” prostheses designs, which are comprised of rigid leaflets and require life-long anticoagulation therapy [2]. However, the durability of a typical BHV remains limited to about 10–15 years, with failure resulting from structural deterioration, mediated by fatigue and tissue mineralization [1–3]. While much effort has gone into developing methods to mitigate mineralization, methods to extend durability remain largely unexplored. A critical part of such efforts to improve the design of BHVs is understanding the stresses acting on leaflets over the complete cardiac cycle.

Some previous computational studies on heart valve mechanics have used (quasi-)static [4, 5] and dynamic [6] structural analysis, with assumed pressure loads on the leaflets. This produces deformation and stress distributions that can be used to understand the mechanical behavior of BHVs. However, the assumed pressure load only crudely approximates the interaction between blood and valvular structures. A purely structural analysis is only applicable to static pressurization of a closed valve, which represents only a portion of the full cardiac cycle. It is therefore important to develop a computational framework that is able to simulate the dynamics of heart valves interacting with hemodynamics—a method for computational fluid–structure interaction (FSI)—which considers the complete mechanical

NIH-PA Author Manuscript

NIH-PA Author Manuscript

NIH-PA Author Manuscript

environment of the valve and applies more accurate tractions to the leaflets during the entire cardiac cycle.

Many FSI methods employ boundary-fitted approaches, where the fluid problem is solved on a mesh that deforms around a Lagrangian structure mesh, matching it at the shared interface. The fluid problem on the deforming domain is said to be posed in an arbitrary Lagrangian–Eulerain (ALE) coordinate system [7–9]. In the FSI literature, the term ALE is sometimes reserved for numerical methods using finite elements in space and finite differences in time, distinguishing them from methods that use space–time finite elements, such as the deforming-spatial-domain/stabilized space–time (DSD/SST) technique [10, 11]. Boundary-fitted FSI methods have been applied to challenging classes of real-world problems, including cardiovascular [12–17], parachute [18–24], and wind turbine [25–27] applications. The history, state-of-the-art, and practical applications of ALE and DSD/SST methods for FSI are covered thoroughly by Bazilevs et al. [28]. Boundary-fitted methods have the advantage of satisfying kinematic constraints by construction but, for scenarios that involve large translational and/or rotational structural motions, the boundary-fitted fluid mesh can become severely distorted if it is continuously deformed from a single reference configuration, harming both the conditioning of the discrete problem and the accuracy of its solution.

Applying boundary-fitted methods to complex engineered systems may therefore require specialized solution strategies to maintain fluid mesh quality. One approach is remeshing, in which all or part of the fluid domain is automatically re-discretized in space when mesh distortion becomes too extreme [29–32]. Mesh management is complicated further if the structure moves into and out of contact with itself, changing the topology of the fluid domain. For some applications, it may be sufficient to use specialized contact algorithms that modify the problem to enforce a small minimum separation between surfaces that would otherwise come into contact [33]. In our application to a heart valve, however, the ability of the structure to close and block flow is an essential aspect of the problem. Recent work [34, 35] has extended DSD/SST methods to include true changes of topology without remeshing, but has so far only been applied to problems in which the boundary motion is known beforehand and prescribed. While the rigid motions of hinged mechanical prosthetic heart valves have been successfully studied with boundary-fitted methods [36, 37], it is our opinion that maintaining mesh quality would become prohibitively difficult in a boundary-fitted simulation of a native or bioprosthetic heart valve, where flexible leaflets deform and contact each other in complex patterns that cannot be parameterized by a small set of variables.

For these reasons, non-boundary-fitted approaches have become a popular alternative for computational FSI [38–44], and are the focus of the present contribution. The first non-boundary-fitted approach to become widely known for computational fluid dynamics (CFD) was Peskin’s immersed boundary method [45, 46]. In non-boundary-fitted methods, a separate structural discretization is arbitrarily superimposed onto (or *immersed* into) a background fluid mesh. Such methods are particularly attractive for applications with complex moving boundaries, because they alleviate the difficulties of deforming the fluid mesh. Non-boundary-fitted methods can also handle change of fluid domain topology (e.g.

NIH-PA Author Manuscript

NIH-PA Author Manuscript

NIH-PA Author Manuscript

structural contact) without special treatment in the fluid subproblem. Contact algorithms [47–50] developed in structural dynamics can be adopted directly for the structure subproblem. However, the non-boundary-fitted approach suffers from reduced accuracy of the solution near the fluid–structure interface. Dirichlet boundary conditions cannot be imposed strongly on the discrete solution space, because this space cannot interpolate functions given on an arbitrary immersed boundary. To apply interface conditions, one must devise a suitable method for weak enforcement.

Another limitation of many non-boundary-fitted FSI techniques developed to-date has been failure to faithfully represent the geometry of the immersed structure, and, consequently, the fluid domain from which it is hewn. The importance of eliminating geometrical error in mechanical analysis has reached broader recognition with the advent of isogeometric analysis (IGA) [51], in which the spline bases used by designers (e.g. NURBS [52] or T-splines [53]) are also used to construct discrete solution spaces for analysis purposes. IGA has already been employed to great effect in conjunction with boundary-fitted FSI technologies [54]. Researchers in the IGA community have begun to tackle the challenge of preserving geometry in non-boundary-fitted computational methods [55, 56], but the current literature on this topic suffers from ambiguous terminology. The cited works interpret the existing terms “immersed boundary”, “fictitious domain”, and “embedded domain” inclusively and use them interchangeably while describing novel technologies for exactly capturing complex design geometries in simple background meshes. Through personal communications with numerous colleagues, however, we have realized that the interpretations of these terms can vary greatly; members of the computational mechanics community at large may or may not associate one or more of these terms with specific problem classes and/or numerical methods. Further, all of these terms predate the more recent goal of precisely capturing immersed *geometry* in a non-boundary-fitted background mesh. We therefore introduce a new term: **immersogeometric analysis**. The present study applies this emerging paradigm to FSI problems, by directly immersing NURBS surface representations of solid objects into a background fluid mesh.

The association between non-boundary-fitted methods and cardiovascular applications goes back to Peskin’s original work [57] in 1972 and has been amplified by many publications in the intervening decades. Borazjani [58] compiled a current and thorough literature review and computed one of the most sophisticated and realistic heart valve analyses to date, using the curvilinear immersed boundary (CURVIB) method [59, 60]. Our work follows most directly from the fictitious domain method devised by Baaijens [61] and applied to heart valves by de Hart [62]. Baaijens and de Hart used Lagrange multipliers to enforce kinematic constraints between finite element discretizations of the fluid and thin immersed structures.

Prior simulations of heart valve FSI have suffered from a number of shortcomings. De Hart’s implementation of the fictitious domain method does not contain any contact model and, while the author notes that the FSI kinematics alone should prevent the structure from self-intersecting, he found that, in practical discretizations, the weak constraint enforcement afforded by Lagrange multipliers still allowed significant penetrations. Further, de Hart’s computations relied on symmetry assumptions that do not hold in the relevant flow regime [58]. Borazjani included contact in a computation of a full valve, but neither author

NIH-PA Author Manuscript

NIH-PA Author Manuscript

NIH-PA Author Manuscript

satisfactorily computed the closed state of the valve, in which the leaflets must oppose a steep pressure gradient to enforce nearly hydrostatic flow.

In this work, we derive several related variational formulations from an augmented Lagrangian framework for FSI proposed by Bazilevs et al. [63]. The variational equations are the sum of fluid and structure subproblems, with additional terms to enforce the kinematic constraint of velocity continuity at the fluid–structure interface. One additional term enforces the constraint through a Lagrange multiplier defined on the interface, while another term augments this constraint enforcement with a penalty to increase convexity of the formulation about the subset of the solution space satisfying the kinematic constraint.

For immersed volumetric objects, we follow the idea given in Bazilevs et al. [63] to formally eliminate the multiplier field, arriving at a method for weak enforcement of Dirichlet boundary conditions. This method of weak enforcement may be viewed as an extension of Nitsche's method [64]. We implement this with an adaptive quadrature rule, to accurately integrate over the fluid domain. As an added benefit, imposing the Dirichlet boundary conditions weakly in fluid dynamics allows the flow to slip on the solid surface when the wall-normal mesh size is relatively large. This effect mimics the thin boundary layer that would otherwise need to be resolved with spatial refinement, allowing more accurate solutions on coarse meshes [65–69]. In a non-boundary-fitted method, the fluid mesh is arbitrarily cut by the structural boundary, producing a boundary layer discretization of inferior quality compared to the boundary-fitted case. Therefore, the weakly enforced Dirichlet boundary conditions are *crucial* to obtaining more accurate fluid solutions when the non-boundary-fitted approach is used.

To model the valve leaflets we utilize immersed shell structures. We study various interpretations of the augmented Lagrangian framework applied to vanishingly-thin structures immersed in non-boundary-fitted fluid discretizations. We find that our extension of Nitsche's method reduces to a penalty method. This penalty method may be sufficient to accurately compute quantities of interest for some problem types, but applications (such as the BHV) with large pressure jumps across the thin shell reveal shortcomings of the penalty approach. To counteract steep pressure gradients through the structure without the conditioning problems that accompany strong penalty forces, we introduce the additional unknowns to approximate the multiplier field. Further, since the fluid discretization is not tailored to the structure geometry, there is an inherent error in the approximation of pressure discontinuities across the shell. Our fluid formulation uses residual-based stabilization derived from a variational multiscale (VMS) analysis [70, 71]. This stabilization interacts with the large pressure error near the shell, leading to problematic compressibility at practical levels of refinement. To counteract this artificial compression, we weaken stabilization near the immersed shell structure.

While the immersogeometric concept does not, in principle, limit the choice of background mesh solution spaces to splines, we elect to use NURBS bases to construct fluid and structure solutions in this work, due to the desirable mathematical properties of these spline functions. NURBS function spaces can have higher continuity than the approximation spaces found in traditional finite element analysis. For the fluid subproblem, this continuity

NIH-PA Author Manuscript

NIH-PA Author Manuscript

NIH-PA Author Manuscript

provides special benefits in turbulent flow simulation [72, 73] and, for the structure subproblem, it eliminates the need for extra rotational degrees of freedom in thin shell formulations [74] and better represents sliding contact between smooth surfaces [75]. The advantages of using spline bases in contact problems were demonstrated in the context of heart valve leaflet coaptation by Morganti et al. [76].

The paper is organized as follows. In Section 2, we introduce the augmented Lagrangian framework for FSI and relate it to Nitsche's method. In Section 3, we employ an adaptive quadrature technique to implement Nitsche's method for flow around immersed geometries, testing it on the benchmark problem of 2D flow over a cylinder. Section 4 addresses the difficulties of enforcing constraints when the structure becomes infinitesimally thin. We discuss the computational methods implied by various interpretations of the augmented Lagrangian in this limit and present results for the benchmark problems corresponding to idealizations of open and closed heart valves. In Section 5, we combine our FSI technology with a penalty-based dynamic contact algorithm for shell structures, allowing us to compute a realistic FSI simulation of a bioprosthetic heart valve. Section 6 draws conclusions and provides a graphical representation (Figure 33) of the interrelations between ideas, methods, and computations presented throughout the paper. The reader may find this conceptual map helpful while navigating the body of the paper.

2. Augmented Lagrangian framework for FSI

Our starting point is the augmented Lagrangian framework for FSI introduced by Bazilevs et al. [63]. We consider $(\Omega_1)_t$ and $(\Omega_2)_t$ to be regions (subsets of $\mathbb{R}^d$, $d \in \{2, 3\}$) occupied by an incompressible fluid and an elastic solid, respectively, at time t, with $(\Gamma_1)_t$ and $(\Gamma_2)_t$ to be their corresponding boundaries. These regions meet at a shared interface, $(\Gamma_I)_t$. Let $\mathbf{u}_1$ and p denote the fluid velocity and pressure, respectively, and $\mathbf{u}_2$ denote the velocity of the structure. We impose the kinematic constraint that $\mathbf{u}_1 = \mathbf{u}_2$ on $(\Gamma_I)_t$ through the addition of the following augmented Lagrangian terms:

$$\int_{(\Gamma_I)_t} \boldsymbol{\lambda} \cdot (\mathbf{u}_1 - \mathbf{u}_2) d\Gamma + \frac{1}{2} \int_{(\Gamma_I)_t} \beta |\mathbf{u}_1 - \mathbf{u}_2|^2 d\Gamma, \quad (1)$$

where $\boldsymbol{\lambda}$ is a Lagrange multiplier and $\beta \geq 0$ is a penalty parameter to increase convexity around the feasible region defined by the constraint. The variational problem is: Find $\mathbf{u}_1 \in \mathscr{S}_u$, $p \in \mathscr{S}_p$, $\mathbf{u}_2 \in \mathscr{S}_d$, and $\boldsymbol{\lambda} \in \mathscr{S}_\ell$ such that for all test functions $\mathbf{w}_1 \in \mathscr{V}_u$, $q \in \mathscr{V}_p$, $\mathbf{w}_2 \in \mathscr{V}_d$, and $\delta\boldsymbol{\lambda} \in \mathscr{V}_\ell$

$$B_1(\{\mathbf{w}_1, q\}, \{\mathbf{u}_1, p\}; \hat{\mathbf{u}}) - F_1(\{\mathbf{w}_1, q\}) + \int_{(\Gamma_I)_t} \mathbf{w}_1 \cdot \boldsymbol{\lambda} d\Gamma + \int_{(\Gamma_I)_t} \mathbf{w}_1 \cdot \beta(\mathbf{u}_1 - \mathbf{u}_2) d\Gamma = 0, \quad (2)$$

$$B_2(\mathbf{w}_2, \mathbf{u}_2) - F_2(\mathbf{w}_2) - \int_{(\Gamma_I)_t} \mathbf{w}_2 \cdot \boldsymbol{\lambda} d\Gamma - \int_{(\Gamma_I)_t} \mathbf{w}_2 \cdot \beta(\mathbf{u}_1 - \mathbf{u}_2) d\Gamma = 0, \quad (3)$$

NIH-PA Author Manuscript

NIH-PA Author Manuscript

NIH-PA Author Manuscript

$$\int_{(\Gamma_1)_t} \delta\boldsymbol{\lambda}\cdot(\mathbf{u}_1-\mathbf{u}_2)d\Gamma=0, \quad (4)$$

where $\mathscr{S}_u$, $\mathscr{S}_p$, $\mathscr{S}_d$, and $\mathscr{S}_\ell$ are the function spaces for the fluid velocity, fluid pressure, structural velocity, and Lagrange multiplier solutions, respectively, and $\mathscr{V}_u$, $\mathscr{V}_p$, $\mathscr{V}_d$, and $\mathscr{V}_\ell$ are the corresponding weighting function spaces. B_1, B_2, F_1, and F_2 are the semi-linear forms and linear functionals corresponding to the fluid and structural mechanics problems, respectively, and are given by

$$B_1(\{\mathbf{w},q\},\{\mathbf{u},p\};\hat{\mathbf{u}})=\int_{(\Omega_1)_t}\mathbf{w}\cdot\rho_1\left(\left.\frac{\partial\mathbf{u}}{\partial t}\right|_{\hat{\mathbf{x}}}+(\mathbf{u}-\hat{\mathbf{u}})\cdot\nabla\mathbf{u}\right)d\Omega+\int_{(\Omega_1)_t}\boldsymbol{\varepsilon}(\mathbf{w}):\boldsymbol{\sigma}_1 d\Omega+\int_{(\Omega_1)_t}q\nabla\cdot\mathbf{u}d\Omega, \quad (5)$$

$$F_1(\{\mathbf{w},q\})=\int_{(\Omega_1)_t}\mathbf{w}\cdot\rho_1\mathbf{f}_1 d\Omega+\int_{(\Gamma_{1\mathrm{h}})_t}\mathbf{w}\cdot\mathbf{h}_1 d\Gamma, \quad (6)$$

$$B_2(\mathbf{w},\mathbf{u})=\int_{(\Omega_2)_t}\mathbf{w}\cdot\rho_2\left.\frac{\partial\mathbf{u}}{\partial t}\right|_{\mathbf{x}} d\Omega+\int_{(\Omega_2)_t}\boldsymbol{\varepsilon}(\mathbf{w}):\boldsymbol{\sigma}_2 d\Omega, \quad (7)$$

$$F_2(\mathbf{w})=\int_{(\Omega_2)_t}\mathbf{w}\cdot\rho_2\mathbf{f}_2 d\Omega+\int_{(\Gamma_{2\mathrm{h}})_t}\mathbf{w}\cdot\mathbf{h}_2 d\Gamma, \quad (8)$$

where ρ_1 and ρ_2 are the fluid and structural densities, respectively, $\hat{\mathbf{u}}$ is the velocity of the fluid domain $(\Omega_1)_t$, $\boldsymbol{\sigma}_1$ and $\boldsymbol{\sigma}_2$ are the fluid and structural Cauchy stresses, respectively, $\boldsymbol{\varepsilon}(\cdot)$ is the symmetric gradient operator given by $\boldsymbol{\varepsilon}(\mathbf{w})=\frac{1}{2}(\nabla\mathbf{w}+\nabla\mathbf{w}^T)$, $\mathbf{f}_1$ and $\mathbf{f}_2$ are the applied body forces and $\mathbf{h}_1$ and $\mathbf{h}_2$ are the applied surface tractions on the fluid and structure, respectively, $(\Gamma_{1\mathrm{h}})_t$ and $(\Gamma_{2\mathrm{h}})_t$ are the boundaries where the surface tractions are specified, $\left.\frac{\partial(\cdot)}{\partial t}\right|_{\hat{\mathbf{x}}}$ is the time derivative taken with respect to the fixed spatial coordinate $\hat{\mathbf{x}}$ in the referential domain (which does not follow the motion of the fluid itself), and $\left.\frac{\partial(\cdot)}{\partial t}\right|_{\mathbf{x}}$ is the time derivative holding the material coordinates $\mathbf{X}$ fixed. The gradient ∇ is taken with respect to the spatial coordinate $\mathbf{x}$ of the current configuration. We assume that the fluid is Newtonian with dynamic viscosity μ, and Cauchy stress $\boldsymbol{\sigma}_1=-p\mathbf{I}+2\mu\boldsymbol{\varepsilon}(\mathbf{u}_1)$.

Bazilevs et al. [63] demonstrate how the multiplier, $\boldsymbol{\lambda}$, may be formally eliminated by substituting an expression for the fluid–structure interface traction in terms of the other unknowns. This leads to the following variational formulation for the coupled problem: find $\mathbf{u}_1\in\mathscr{S}_u$, $p\in\mathscr{S}_p$, and $\mathbf{u}_2\in\mathscr{S}_d$ such that for all $\mathbf{w}_1\in\mathscr{V}_u$, $q\in\mathscr{V}_p$, and $\mathbf{w}_2\in\mathscr{V}_d$

NIH-PA Author Manuscript

NIH-PA Author Manuscript

NIH-PA Author Manuscript

$$
\begin{aligned}
&B_1(\{\mathbf{w}_1, q\}, \{\mathbf{u}_1, p\}; \hat{\mathbf{u}}) \\
&\quad - F_1(\{\mathbf{w}_1, q\}) \\
&\quad + B_2(\mathbf{w}_2, \mathbf{u}_2) \\
&\quad - F_2(\mathbf{w}_2) \\
&\quad - \int_{(\Gamma_I)_t} (\mathbf{w}_1 \\
&\qquad - \mathbf{w}_2) \cdot \boldsymbol{\sigma}_1(\mathbf{u}_1, p)\mathbf{n}_1 d\Gamma \qquad (9) \\
&\quad - \int_{(\Gamma_I)_t} \delta\boldsymbol{\sigma}_1(\mathbf{w}_1, q)\mathbf{n}_1 \\
&\quad \cdot (\mathbf{u}_1 - \mathbf{u}_2) d\Gamma \\
&\quad + \int_{(\Gamma_I)_t} (\mathbf{w}_1 \\
&\qquad - \mathbf{w}_2) \cdot \beta(\mathbf{u}_1 - \mathbf{u}_2) d\Gamma = 0.
\end{aligned}
$$

Further manipulations arrive at a formulation for weak imposition of Dirichlet boundary conditions on the fluid problem,

$$
B_1(\{\mathbf{w}_1, q\}, \{\mathbf{u}_1, p\}; \hat{\mathbf{u}}) - F_1(\{\mathbf{w}_1, q\}) - \int_{(\Gamma_I)_t} \mathbf{w}_1 \cdot \boldsymbol{\sigma}_1 \mathbf{n}_1 d\Gamma - \int_{(\Gamma_I)_t} \delta\boldsymbol{\sigma}_1 \mathbf{n}_1 (\mathbf{u}_1 - \mathbf{u}_2) d\Gamma + \int_{(\Gamma_I)_t} \mathbf{w}_1 \cdot \beta(\mathbf{u}_1 - \mathbf{u}_2) d\Gamma = 0, \qquad (10)
$$

and a traction boundary condition for the structure problem that is a combination of the fluid Cauchy stress and a penalty force:

$$
B_2(\mathbf{w}_2, \mathbf{u}_2) - F_2(\mathbf{w}_2) + \int_{(\Gamma_I)_t} \mathbf{w}_2 \cdot (\boldsymbol{\sigma}_1 \mathbf{n}_1 + \beta(\mathbf{u}_2 - \mathbf{u}_1)) d\Gamma = 0. \qquad (11)
$$

This approach to weak imposition of Dirichlet boundary conditions in fluid mechanics was first proposed by Bazilevs and Hughes [65] and further refined in Bazilevs et al. [66, 67]. It may be interpreted as an extension of Nitsche's method [77], which is a consistent and stabilized method for imposing constraints on the boundaries by augmenting the governing equations with additional constraint equations. While Nitsche's method may be motivated independently of the augmented Lagrangian formulation, we find that some cases require us to revisit Eqs. (2)–(4) and account for the multipliers directly. The solution techniques for the fluid subproblem (10) are discussed in Section 3, which follows.

3. Nitsche's method for flow around immersed geometries

In a non-boundary-fitted method, the elements of the fluid discretization may extend into the interior of an immersed object. Imposing Dirichlet boundary conditions is no longer straightforward given that the basis functions are non-interpolating at the object boundaries. In order to enforce essential boundary conditions, one can either modify the basis functions so they vanish at the interface [78] or augment the governing equations with additional constraint equations. In this work we choose the latter approach.

NIH-PA Author Manuscript

NIH-PA Author Manuscript

NIH-PA Author Manuscript

In this section, we formally eliminate the Lagrange multiplier from Eqs. (2)–(4), as mentioned in Section 2 and detailed by Bazilevs et al. [63], to yield the fluid subproblem (10), which corresponds to an application of Nitsche's method to the boundary condition on the fluid–structure interface. This method has significant shortcomings when the thickness of the structure falls below the element size of the background fluid discretization and a different approach is required to improve our numerical method for the target application of bioprosthetic heart valve analysis. Nevertheless, the elimination of the multiplier field in the current section allows us to develop and test a fully-discrete immersogeometric formulation for the fluid subproblem without immediately facing the various technical complications associated with discretizing the multiplier field and approximating solution kinks and discontinuities induced by thin immersed structures.

3.1. Semi-discrete fluid formulation with weak boundary conditions

Consider a collection of disjoint elements $\{\Omega^e\}$, $\cup_e \Omega^e \subset \mathbb{R}^d$, with closures covering the fluid domain: $\Omega_1 \subset \cup_e \overline{\Omega^e}$. Note that Ω^e is not necessarily a subset of Ω_1. $\{\Omega^e\}$, Ω_1, and Γ_I remain time-dependent, but we drop the subscript t for notational convenience. The mesh defined by $\{\Omega^e\}$ deforms with a velocity field $\hat{\mathbf{u}}^h$ and the boundary Γ_I moves with velocity $\mathbf{u}_2$. We consider discrete velocity and pressure spaces $\mathscr{V}_u^h$ and $\mathscr{V}_p^h$ of both trial and test functions supported on these elements and pose the semi-discrete problem of finding $\mathbf{u}_1^h \in \mathscr{V}_u^h$ and $p^h \in \mathscr{V}_p^h$ such that for all $\mathbf{w}_1^h \in \mathscr{V}_u^h$ and $q^h \in \mathscr{V}_p^h$

NIH-PA Author Manuscript

NIH-PA Author Manuscript

NIH-PA Author Manuscript

$$
\begin{aligned}
&B_1^{\mathrm{VMS}}\left(\{\mathbf{w}_1^h, q^h\}, \{\mathbf{u}_1^h, p^h\}; \hat{\mathbf{u}}^h\right) \\
&\quad - F_1^{\mathrm{VMS}}\left(\{\mathbf{w}_1^h, q^h\}\right) \\
&\quad - \int_{\Gamma_{\mathrm{I}}} \mathbf{w}_1^h \cdot \left(-p^h \mathbf{n}_1 + 2\mu\boldsymbol{\varepsilon}(\mathbf{u}_1^h)\mathbf{n}_1\right) d\Gamma \\
&\quad - \int_{\Gamma_{\mathrm{I}}} \left(2\mu\boldsymbol{\varepsilon}(\mathbf{w}_1^h)\mathbf{n}_1 \right. \\
&\quad \left. + q^h \mathbf{n}_1\right) \\
&\quad \cdot \left(\mathbf{u}_1^h - \mathbf{u}_2\right) d\Gamma \\
&\quad - \int_{(\Gamma_{\mathrm{I}})^-} \mathbf{w}_1^h \cdot \rho_1 \left(\left(\mathbf{u}_1^h \right.\right. \\
&\quad \left.\left. - \hat{\mathbf{u}}^h\right) \cdot \mathbf{n}_1\right) \left(\mathbf{u}_1^h - \mathbf{u}_2\right) d\Gamma \\
&\quad + \int_{\Gamma_{\mathrm{I}}} \tau_{\mathrm{TAN}}^B \left(\mathbf{w}_1^h \right. \\
&\quad \left. - \left(\mathbf{w}_1^h \cdot \mathbf{n}_1\right) \mathbf{n}_1\right) \\
&\quad \cdot \left(\left(\mathbf{u}_1^h \right.\right. \\
&\quad \left.\left. - \mathbf{u}_2 - \left(\left(\mathbf{u}_1^h \right.\right.\right. \right. \\
&\quad \left.\left.\left. \left. - \mathbf{u}_2\right) \cdot \mathbf{n}_1\right) \mathbf{n}_1\right) d\Gamma \\
&\quad + \int_{\Gamma_{\mathrm{I}}} \tau_{\mathrm{NOR}}^B \left(\mathbf{w}_1^h \right. \\
&\quad \left. \cdot \mathbf{n}_1 \left(\left(\mathbf{u}_1^h \right.\right.\right. \\
&\quad \left.\left.\left. - \mathbf{u}_2\right) \cdot \mathbf{n}_1\right) d\Gamma = 0,
\end{aligned}
\tag{12}
$$

where $(\Gamma_{\mathrm{I}})^-$ is the "inflow" part of Γ_{I}, on which $(\mathbf{u}_1^h - \hat{\mathbf{u}}^h) \cdot \mathbf{n}_1 < 0$. Note that Γ_{I} may cut through element interiors. The constants τ_{TAN}^B and τ_{NOR}^B correspond to a splitting of the penalty, β, into the tangential and normal directions, respectively. The forms B_1^{VMS} and F_1^{VMS} are the VMS discretizations of B_1 and F_1, respectively, given by

NIH-PA Author Manuscript NIH-PA Author Manuscript NIH-PA Author Manuscript

$$
\begin{aligned}
&B_1^{\mathrm{VMS}}(\{\mathbf{w},q\},\{\mathbf{u},p\};\hat{\mathbf{u}}) \\
&\quad=\int_{(\Omega_1)_t}\mathbf{w}\cdot\rho_1\left(\left.\frac{\partial\mathbf{u}}{\partial t}\right|_{\hat{\mathbf{x}}}\right. \\
&\qquad\left.+(\mathbf{u}-\hat{\mathbf{u}})\cdot\nabla\mathbf{u}\right)d\Omega \\
&\quad+\int_{(\Omega_1)_t}\boldsymbol{\varepsilon}(\mathbf{w}):\boldsymbol{\sigma}_1 d\Omega \\
&\quad+\int_{(\Omega_1)_t}q\nabla \\
&\quad\cdot\mathbf{u}d\Omega \\
&\quad+\sum_e\int_{\Omega^e\cap\Omega_1}\left((\mathbf{u}-\hat{\mathbf{u}})\cdot\nabla\mathbf{w}+\frac{\nabla q}{\rho_1}\right)\cdot\mathbf{u}'d\Omega \\
&\quad+\sum_e\int_{\Omega^e\cap\Omega_1}\nabla \\
&\quad\cdot\mathbf{w}\rho_1\tau_{\mathrm{C}}\nabla \\
&\quad\cdot\mathbf{u}d\Omega \\
&\quad-\sum_e\int_{\Omega^e\cap\Omega_1}\mathbf{w} \\
&\quad\cdot(\mathbf{u}' \\
&\qquad\cdot\nabla\mathbf{u})d\Omega \\
&\quad-\sum_e\int_{\Omega^e\cap\Omega_1}\frac{\nabla\mathbf{w}}{\rho_1}:(\mathbf{u}'\otimes\mathbf{u}')d\Omega \\
&\quad+\sum_e\int_{\Omega^e\cap\Omega_1}(\mathbf{u}' \\
&\qquad\cdot\nabla\mathbf{w})\bar{\tau} \\
&\quad\cdot(\mathbf{u}'\cdot\nabla\mathbf{u})d\Omega,
\end{aligned}
\tag{13}
$$

and

$$
F_1^{\mathrm{VMS}}(\{\mathbf{w},q\})=F_1(\{\mathbf{w},q\}), \tag{14}
$$

where

$$
\mathbf{u}'=\tau_{\mathrm{M}}\left(\rho_1\left(\left.\frac{\partial\mathbf{u}}{\partial t}\right|_{\hat{\mathbf{x}}}+(\mathbf{u}-\hat{\mathbf{u}})\cdot\nabla\mathbf{u}-\mathbf{f}\right)-\nabla\cdot\boldsymbol{\sigma}_1\right). \tag{15}
$$

Equations (13)–(15) correspond to the ALE–VMS formulation of the Navier–Stokes equations of incompressible flows [79]. The additional terms may be interpreted both as stabilization and as a turbulence model [73, 80–85]. The specific form of VMS stabilization that we use was presented and applied to FSI problems by Bazilevs et al. [54]. The stabilization parameters are

NIH-PA Author Manuscript

NIH-PA Author Manuscript

NIH-PA Author Manuscript

$$\tau_{\mathrm{M}}=\left(\frac{C_t}{\Delta t^2}+(\mathbf{u}-\hat{\mathbf{u}})\cdot\mathbf{G}(\mathbf{u}-\hat{\mathbf{u}})+C_I\nu^2\mathbf{G}:\mathbf{G}\right)^{-1/2}, \quad (16)$$

$$\tau_{\mathrm{C}}=(\tau_{\mathrm{M}}\mathrm{tr}\mathbf{G})^{-1}, \quad (17)$$

$$\bar{\tau}=(\mathbf{u}'\cdot\mathbf{G}\mathbf{u}')^{-1/2}, \quad (18)$$

where Δt is the time-step size, $\nu = \mu/\rho_1$ is the kinematic viscosity, C_I is a positive constant derived from an appropriate element-wise inverse estimate [86–89], **G** generalizes the notion of element size to physical elements mapped from a parametric parent element by $\mathbf{x}(\xi)$:

$$G_{ij}=\sum_{k=1}^{d}\frac{\partial\xi_k}{\partial x_i}\frac{\partial\xi_k}{\partial x_j}, \quad (19)$$

tr**G** is the trace of **G**, and the parameter C_t is typically equal to 4 [73, 82]. Note that we have modified the usual formulation, so that integrals are taken only over intersections of elements with Ω_1. Accurate evaluation of such integrals for general immersed geometries is the primary practical challenge associated with this formulation. An approach to computing these integrals is discussed in Section 3.2.

Remark 1—The fluid mesh motion given by $\hat{\mathbf{u}}^h$ may at first appear superfluous in the context of non-boundary-fitted methods. However, a single computation might gainfully combine a boundary-fitted, deforming-mesh treatment of some structures with a non-boundary-fitted treatment of others. The fluid–solid interface-tracking/interface-capturing technique (FSITICT) proposed in Tezduyar et al. [90] is a more general method in that category. In the FSITICT, the distribution of the fluid–solid interfaces between the interface-tracking (boundary-fitted) and interface-capturing (non-boundary-fitted) techniques can change during the computation. The interface-capturing technique is used wherever and whenever it can be used. The test computations reported in Wick [91] were based on a special-case implementation of the FSITICT, where the distribution of the fluid–solid interfaces between the interface-tracking and interface-capturing methods does not change during the computation. An example of FSITICT relevant to our application would be immersion of non-boundary-fitted heart valve leaflets into a boundary-fitted discretization of the interior of a flexible artery, as first attempted by de Hart [62]. In computations with a fixed background fluid mesh, one can simply set $\hat{\mathbf{u}}^h = \mathbf{0}$ in the above formulations.

Remark 2—The final term of Eq. (13) does not follow from VMS analysis. It is an additional residual-based stabilization term that is included to provided extra stabilizing dissipation near sharp solution gradients, while maintaining variational consistency with the exact solution. It was introduced by Taylor et al. [92] and bears resemblance to the discontinuity-capturing directional dissipation (DCDD) [93] and YZβ [94, 95] stabilization techniques.

NIH-PA Author Manuscript

NIH-PA Author Manuscript

NIH-PA Author Manuscript

The terms from the second to the last line of Eq. (12) are responsible for the weak enforcement of kinematic and traction constraints at the boundaries of the immersed geometries. It was shown in earlier work [65–69] that imposing the Dirichlet boundary conditions weakly in fluid dynamics allows the flow to slip on the solid surface when the wall-normal mesh size is relatively large. This effect mimics the thin boundary layer that would otherwise need to be resolved with spatial refinement, allowing more accurate solutions on coarse meshes. In the non-boundary-fitted method, the fluid mesh is arbitrarily cut by the structural boundary, leaving a boundary layer discretization of inferior quality compared to the boundary-fitted case. Therefore, in addition to imposing the constraints easily in the context of non-boundary-fitted approach, we may obtain more accurate fluid solutions as an added benefit of using the weak boundary condition formulation (12).

Remark 3—Equation (12) includes an "inflow" stabilization term that is not associated with Nitsche's approach. This term is added to better satisfy the inflow boundary condition and to enhance the stability of the formulation, without affecting consistency or adjoint consistency. See Bazilevs et al. [65] for details. To ensure balanced interface tractions between the fluid and structure, we append the corresponding reaction force term

$$\int_{(\Gamma_I)^-} \mathbf{w}_2 \cdot \rho_1 \left(\left(\mathbf{u}_1^h - \hat{\mathbf{u}}^h \right) \cdot \mathbf{n}_1 \right) \left(\mathbf{u}_1^h - \mathbf{u}_2 \right) d\Gamma \quad (20)$$

to the left-hand side of structure subproblem, Eq. (11).

In Eq. (12), the parameters τ^B_{TAN} and τ^B_{NOR} must be sufficiently large to stabilize the formulation, but not so large as to degenerate Nitsche's method into a pure penalty method, which entails the disadvantages of losing variational consistency and having an ill-conditioned stiffness matrix. Based on previous studies of weakly-enforced Dirichlet boundary conditions in fluid mechanics [65–67], we expect these parameters to scale as

$$\tau^B_{(\cdot)} = \frac{C^B_I \mu}{h} \quad (21)$$

where *h* is a measure of the element size at the boundary and C^B_I is a dimensionless constant. However, in the case of an immersed boundary, neither the appropriate definition of *h* nor the principle for deriving C^B_I is straightforward. In subsequent sections, we investigate different penalty values through numerical experiments.

Remark 4—A more sophisticated approach to determine the values of the stabilization parameters for Nitsche's method is to solve local eigenvalue problems. See Hughes and Harari [96], Embar et al. [97], and Ruess et al. [56, 98] for more details.

3.1.1. Backflow stabilization—Unsteady CFD computations may sometimes diverge due to flow reversal on outflow boundaries. This is known as backflow divergence and is frequently encountered in cardiovascular simulations. In some problems studied in this paper, we encounter this backflow divergence and an outflow stabilization method originally proposed in Bazilevs et al. [99] is applied to compensate for it. The backflow stabilization

NIH-PA Author Manuscript

NIH-PA Author Manuscript

NIH-PA Author Manuscript

method was further studied and found to be the least intrusive and computationally expensive of all the techniques examined in Esmaily-Moghadam et al. [100]. The method adds the following term to the left-hand side of Eq. (12):

$$\sum_{a=1}^{n_{\text{out}}} \left(-\gamma \int_{\Gamma_1^a} \mathbf{w}_1^h \cdot \rho_1 \left\{ \left(\mathbf{u}_1^h - \hat{\mathbf{u}}^h \right) \cdot \mathbf{n}_1 \right\}_- \mathbf{u}_1^h d\Gamma \right) \quad (22)$$

where $\{\Gamma_1^a\}_{a=1}^{n_{\text{out}}}$ are the outflow portions of the fluid domain boundary, γ is a dimensionless nonnegative scalar controlling the strength of the stabilization, and

$$\left\{ \left(\mathbf{u}_1^h - \hat{\mathbf{u}}^h \right) \cdot \mathbf{n}_1 \right\}_- = \frac{1}{2} \left(\left(\mathbf{u}_1^h - \hat{\mathbf{u}}^h \right) \cdot \mathbf{n}_1 - \left| \left(\mathbf{u}_1^h - \hat{\mathbf{u}}^h \right) \cdot \mathbf{n}_1 \right| \right) \quad (23)$$

is the component of velocity pointing opposite the outward-facing normal of the fluid domain.

3.1.2. Choice of discrete spaces—The stabilized VMS formulation given by Eq. (13) circumvents the Babuška–Brezzi stability considerations [101, 102] that would otherwise limit the useful choices of discrete spaces for saddle point problems such as incompressible flow [103]. We therefore have great freedom in our choices of $\mathcal{V}_{(\cdot)}^h$. For all computations presented in this paper, we use the same scalar discrete space to represent test and trial functions for the pressure and each Cartesian component of velocity. This scalar space is the span of NURBS or B-spline basis functions defined on one or more *d*-variate knot spaces forming a multi-patch isogeometric mesh. We refer the reader to Piegl and Tiller [52] for a detailed construction of such bases and discussion of their properties.

3.2. The finite cell method and adaptive quadrature

A similar formulation of Nitsche's method for immersed boundary FSI has been studied by Benk et al. [104], who assume that the immersed boundary is a triangulated surface and use methods from computational geometry to decompose the exterior parts of cut fluid elements into polyhedrons with known quadrature rules. We apply instead an adaptive quadrature rule from the finite cell method [105–107] that relies only on a test to determine whether or not an arbitrary point lies inside of an immersed object. This relaxes Benk et al.'s assumption that the immersed boundaries are triangulated.

The finite cell method, introduced by Parvizian et al. [108] and illustrated in Figure 1, is a technique for solving partial differential equations posed on complex geometries by extending the computational domain to a more tractable shape, such as a rectangular prism bounding the original domain. The finite cell method discretizes this extended domain into elements and penalizes the effects of the fictitious extension by modifying the problem's coefficients to have extreme values outside the domain of interest. This introduces discontinuities in coefficients along the boundary of the original domain. Because the extended domain is discretized without respect to the original geometry, these discontinuities may occur within elements. The standard Gaussian quadrature rules typically applied to finite elements [109] assume that a polynomial can accurately approximate the integrand, but this assumption is not true if the integrand is discontinuous. Düster et al. [105]

NIH-PA Author Manuscript

NIH-PA Author Manuscript

NIH-PA Author Manuscript

describe a method of automatically generating more accurate quadrature rules for finite cell computations by dividing cut elements into sub-cells and applying standard quadrature rules within the sub-cells. We apply the same method to the integrals over fluid portions of cut elements in Eq. (13). For completeness, we restate this adaptive quadrature technique, specializing it to the context of immersogeometric FSI. For a summary of recent developments in the finite cell method, we refer the interested reader to Schillinger and Ruess [107].

The quadrature scheme assumes that elements have d-dimensional rectangular parameterizations. The parameter space for each element may be partitioned into 2^d equal sub-cells. Each sub-cell may be likewise divided, as may its children, and so on, yielding a hierarchical 2^d-tree. A sub-cell at any level of this tree has an associated Gaussian quadrature rule. We may construct a quadrature rule for the entire element by summing quadrature rules from disjoint sub-cells covering the element. Not all sub-cells used for this rule need to be from the same level of the tree. Ideally, we would use sub-cells from more refined levels of the hierarchy near the immersed boundary while using larger cells away from the boundary, to reduce the computational cost due to integration. Such an adaptive quadrature rule may be generated by applying the following recursive algorithm, with input $0 \leq l \in \mathbb{Z}$, to a sub-cell covering the entire element:

1. Propose a set of Gaussian quadrature points and weights associated with the current sub-cell.
2. Count the numbers N_{in} and N_{out} of the corners of the sub-cell falling inside and outside of the immersed structure.
3. If $N_{\text{in}} = 0$, $N_{\text{out}} = 0$, or $l = 0$, add the proposed quadrature points falling in the fluid domain to the quadrature rule.
4. Otherwise, if $N_{\text{in}} > 0$, $N_{\text{out}} > 0$, and $l > 0$, discard the proposed points, divide the sub-cell into 2^d children, and apply this algorithm to each child, with input $l - 1$.

Figure 2 illustrates the terminal sub-cells and the adaptive quadrature points that result from applying this algorithm to a 2D circular boundary, with $l = 3$ levels of recursion. The adaptive quadrature points outside the cylinder belong to the fluid domain and are used in the numerical integration. The quadrature points inside the cylinder belong to the fictitious domain extension and are discarded.

Remark 5—In the above algorithm, the geometry of the immersed structure is abstracted behind an inside/outside test that maps spatial positions to truth values. The efficient implementation of this mapping for general geometries is outside the scope of this paper, as we only consider benchmark problems for which it is trivial. A more general implementation could cast rays from a point and count intersections with the closed immersed surface geometry. The operation of ray-surface intersection has been thoroughly optimized within the computer graphics community and was applied to real-time rendering of NURBS surfaces as early as the 1980s [110].

NIH-PA Author Manuscript

NIH-PA Author Manuscript

NIH-PA Author Manuscript

3.2.1. Surface integrals—The surface integrals of Eq. (12) also require special treatment. We employ a variant of the approach used by Düster et al. [105] to integrate immersed boundary traction in finite cell solutions of solid mechanics problems. We define a Gaussian quadrature rule with respect to a parameterization of the boundary of immersed geometry. This parameterization need not be informed by the fluid discretization, but we recommend ensuring that the physical space density of surface quadrature points is reasonably high with respect to the fluid element size. The relevant integrals involve traces of functions defined on the fluid domain. To evaluate these traces, we must be able to locate the quadrature points of the surface in the parameter space of the background mesh. The physical location, $\mathbf{x}_g \in \mathbb{R}^d$, of an integration point can be obtained by evaluating the surface parameterization. Finding the point $\xi_g \in \mathbb{R}^d$ that the fluid mesh parameterization maps to $\mathbf{x}_g$ requires solving a system of d equations to invert the mapping from the fluid mesh parameter space to physical space. If the fluid is represented on a rectangular grid, this inversion is trivial. For more general fluid discretizations, one may apply Newton iteration within parametric elements. It is usually not necessary to attempt this iteration in every fluid element for each surface quadrature point. The searching process can be streamlined by using element bounding boxes and assuming that each surface quadrature point will most likely remain in the same background element or move to a neighboring element between time steps in an unsteady calculation with moving boundaries.

3.3. Time integration of the fluid subproblem

We complete the discretization of the fluid subproblem by applying a time integration scheme to Eq. (12). Our scheme falls within the family of generalized-α integrators, introduced by Chung and Hulbert [111]. The generalized-α framework was first used for the unsteady Navier-Stokes problem by Jansen et al. [112]. The particular integration scheme that we use in the current work is detailed and applied to FSI problems in Bazilevs et al. [54]. The subset of generalized-α methods used in Bazilevs et al. [54] is parameterized by a single number, ρ_∞, where $0 \leq \rho_\infty \leq 1$. Following Bazilevs et al. [73], we use $\rho_\infty = 0.5$ for all computations presented in this paper. The generalized-α time integration is an implicit scheme and requires solution of a nonlinear algebraic problem at each time step. For situations in which only the fluid subproblem is nontrivial (such as the CFD benchmark problem studied in Section 3.4), we directly apply Newton iteration (with an approximate tangent) to converge the residual of this algebraic problem. For coupled FSI, we apply the same time integration scheme, but use more complicated solution strategies for the resulting nonlinear problem. We defer presenting the details of these solution strategies until Section 4.6.

3.4. Flow around an immersed cylinder

In this section, we apply our immersogeometric implementation of Nitsche's method to the classic benchmark problem of 2D flow past a circular cylinder. The problem setup and computational domain are shown in Figure 3. The data given in the diagram is non-dimensional. We use a unit density and define the viscosity in terms of the Reynolds number, $\mu = Re^{-1}$. We strongly enforce the inflow and slip boundary conditions stated in Figure 3. For the no-slip, no-penetration condition $\mathbf{u}_1 = \mathbf{0}$ on the surface of the circular

NIH-PA Author Manuscript

NIH-PA Author Manuscript

NIH-PA Author Manuscript

cylinder, we compare the results of weak enforcement, using our immersogeometric method, with results of strong enforcement, using a boundary-fitted isogeometric mesh.

We expect that, for low Reynolds numbers, this problem will reach a stable steady state and, for moderate Reynolds numbers, it will develop a time-periodic solution. These expectations are characterized more precisely alongside our computed results in Section 6.

3.4.1. Immersogeometric discretizations—We test the Nitsche-based immersogeometric method on two discretizations of the fluid domain. Both meshes use quadratic B-spline elements. The first mesh, abbreviated herein as "M1", contains 12240 elements, with refinement focused around the cylinder as shown in Figure 4. The element size near the cylinder is 0.079. The second mesh, M2, is a uniform *h*-refinement of M1. The inside/outside test required to adaptively generate quadrature rules for the exterior portions of cut cells is, in this case, a trivial distance check from the cylinder's center. The parametric surface used to obtain a quadrature rule for surface integrals over Γ_I, the surface of the cylinder, is a quadratic NURBS circle divided into 256 knot spans in the circumferential direction, with 3-point Gaussian quadrature rules defined on each span. The circumference of this circle is π, giving elements of arc length $\pi/256 \approx 0.012$, which is significantly smaller than the element size in either M1 or M2. For the non-boundary-fitted computations, we consistently use a time-step size of $\Delta t = 0.1$ when steady solutions are anticipated and $\Delta t = 0.05$ when we expect periodicity. This ensures that there will be at least 100 time steps per period in all periodic solutions. The computations are initialized by linearly increasing the inflow velocity from zero to one over some time interval. Details of the initialization procedure should not affect the steady or time-periodic solutions that the system approaches.

Remark 6: We partition the fluid domain into sub-domains, for efficient parallel computation on distributed-memory supercomputers. M1 is decomposed into 12 sub-domains, and M2 into 48. A detailed technical explanation and scalability study of our parallelization strategy may be found in Hsu et al. [113]. In the present computations, we have reduced continuity of the approximation space to C^0 at boundaries between sub-domains. While this is not technically necessary, it minimizes communication bandwidth while maintaining the benefits of higher continuity throughout most of the domain. We find that the impact on quantities of interest is negligible, especially at low Reynolds numbers.

3.4.2. Boundary-fitted reference mesh—The problem at hand has been studied extensively by the CFD community (see, e.g. [114– 121]), but, to control for any discrepancies introduced by differences in fluid formulations or turbulence models, we apply the same VMS formulation (13) to a boundary-fitted discretization of the problem, with a strongly-enforced boundary condition on the surface of the cylinder. We first construct the boundary-fitted mesh BM1 shown in Figure 5, then uniformly refine in space to obtain BM2. Because quantities of interest computed using BM1 and BM2 match to within the precision given in this paper, we consider BM2 to produce reliable reference solutions. BM2 contains 11376 quadratic NURBS elements and the wall-normal element size near the cylinder is 0.0173. The resolution near the cylinder—where the exact solution will vary most rapidly in space and approximations will benefit from *h*-refinement—is significantly greater than that of M1 or M2. By using NURBS elements, we can exactly

NIH-PA Author Manuscript

NIH-PA Author Manuscript

NIH-PA Author Manuscript

represent the circular boundary, completely eliminating geometry error. Time-step sizes in the range of $\Delta t = 0.05$ and 0.025 are selected for the boundary-fitted computations to ensure that there are roughly 200 time steps per period in periodic solutions. The selected Δt's are smaller than those used in non-boundary-fitted computations due to the smaller element sizes near the cylinder compared with that of M2.

Remark 7: At a first glance of Figures 4 and 5, it may seem that the non-boundary-fitted mesh is much more refined than the boundary-fitted one. Zooming closer to the cylinder yet reveal that near the cylinder, the non-boundary-fitted mesh resolution is lower than that of used in the boundary-fitted case. However, due to the tensor-product structure of B-splines (and NURBS), standard *h*-refinement by knot insertion near the immersed cylinder leads to global refinement, which results in a large number of superfluous elements in our immersogeometric discretization.

3.4.3. Comparison of results—We consider four quantities of interest for this problem, although some are relevant only in certain flow regimes. We always measure the drag coefficient, C_D, defined as $2F_D/\rho U^2 d$, where F_D is the drag force or horizontal component of traction integrated over the cylinder surface, ρ is the fluid density, U is the inflow velocity, and d is the diameter of the cylinder. For low Reynolds number cases that reach steady solutions, we consider the bubble recirculation length, L_W. L_W measures how far the stationary vortices occurring at low Reynolds numbers extend downstream of the cylinder. It is defined precisely in Lima E Silva et al. [117]. At higher Reynolds numbers, where flow symmetry breaks, leading to periodic solutions, we consider the lift coefficient, C_L, and the Strouhal number, St. C_L is defined as $2F_L/\rho U^2 d$, where F_L is the lift force or vertical component of traction integrated over the cylinder surface. St is given as $f\,d/U$, where f is the frequency of vortex shedding. The vortex shedding only occurs if the Reynolds number is sufficiently high. We identify the frequency of vortex shedding with the frequency of oscillation in C_L. In periodic solutions, the reported value of C_L is the amplitude of its oscillation and the reported value of C_D is its time average.

The evaluations of C_L and C_D rely on computing the traction at the fluid–structure interface. A naive evaluation of traction from the fluid Cauchy stress, $-\boldsymbol{\sigma}_1\mathbf{n}_1$, will converge poorly to the true traction, so we prefer to use variationally-consistent, conservative definitions of traction [68, 122]. In the case of Nitsche's method, the appropriate discrete traction on surfaces with weakly enforced Dirichlet boundary conditions includes the penalty terms, matching the traction boundary condition of the FSI structural subproblem (11):

$$\mathbf{t}^h = -\boldsymbol{\sigma}_1^h\mathbf{n}_1 - \rho_1\left\{\left(\mathbf{u}_1^h - \hat{\mathbf{u}}^h\right)\cdot\mathbf{n}_1\right\}_-\left(\mathbf{u}_1^h - \mathbf{u}_2\right) + \tau_{\mathrm{TAN}}^B\left(\left(\mathbf{u}_1^h - \mathbf{u}_2\right) - \left(\left(\mathbf{u}_1^h - \mathbf{u}_2\right)\cdot\mathbf{n}_1\right)\mathbf{n}_1\right) + \tau_{\mathrm{NOR}}^B\left(\mathbf{u}_1^h - \mathbf{u}_2\right)\cdot\mathbf{n}_1\mathbf{n}_1, \quad (24)$$

where $\{\cdot\}_-$ denotes the negative part of the bracketed quantity, that is, $\{\mathscr{A}\}_- = \mathscr{A}$ if $\mathscr{A} < 0$ and $\{\mathscr{A}\}_- = 0$ if $\mathscr{A} \geq 0$. In this case, Γ_I is stationary, so $\mathbf{u}_2 = \mathbf{0}$. On a surface with a strongly-enforced Dirichlet condition, as seen in the boundary-fitted computation, the conservative traction must satisfy

NIH-PA Author Manuscript

NIH-PA Author Manuscript

NIH-PA Author Manuscript

$$\int_{(\Gamma_I)^t} \mathbf{w}_1^h \cdot \mathbf{t}^h d\Gamma = B_1^{\mathrm{VMS}}(\{\mathbf{w}_1^h, q^h\}, \{\mathbf{u}_1^h, p^h\}; \hat{\mathbf{u}}^h) - F_1^{\mathrm{VMS}}(\{\mathbf{w}_1^h, q^h\}) \quad (25)$$

for all $\mathbf{w}_1^h$ in an expanded discrete velocity test space that does not strongly enforce the Dirichlet condition. To obtain the i^{th} component of the integral of this conservative traction over the boundary $(\Gamma_I)_t$, we would evaluate the right-hand side of Eq. (25) with $\mathbf{w}_1^h = \mathbf{e}_i$ on $(\Gamma_I)_t$ and $q^h = 0$. The desired $\mathbf{w}_1^h$ is straightforward to construct from shape functions that satisfy the partition of unity property.

First, using three levels of adaptive quadrature, we investigate the effects of different penalty values. We consider only the case in which $\tau^B_{\mathrm{NOR}} = \tau^B_{\mathrm{TAN}} = \tau^B$. In the current non-dimensional setting, we state these penalty values without units. However, they have the physical interpretation of traction per unit difference in speed (between fluid and structure), and the corresponding dimensions of pressure per speed. Further, we would generally expect these values to increase with mesh refinement, so the numbers given here should not be blindly transplanted into other computations without first applying dimensional analysis and considering the relative level of refinement.

Tables 1 and 2 collect the results of applying $\tau^B = 10^2$ and $\tau^B = 10^3$ at various Reynolds numbers for meshes M1 and M2. For comparison, we also give ranges of typical values for these quantities from the CFD literature, specifically [114–121], in Table 3. Figure 6 displays several snapshots of velocity and pressure fields computed using the immersogeometric method with $\tau^B = 10^2$ and $l = 3$ on M1.

From this study, we find that the penalties of the order 10^1 are not consistently stable, while penalties of the order 10^4 and higher become costly to compute with, due to their effect on the conditioning of the problem. This suggests that, while we do not provide a formula for τ^B, it may be chosen from within a wide range of computable values while still providing accurate results. As long as the penalty is chosen such that the computation converges with a reasonable amount of work, our Nitsche-based immersogeometric method achieves good agreement (at the quantity of interest level) with our reference boundary-fitted computation. In some cases on M1 we see slightly worse results with the higher value of τ^B. This is consistent with the idea that approaching strong enforcement of Dirichlet boundary conditions on a mesh that is too coarse to resolve the boundary layer will result in lower quality solutions. Some violation of the no-slip boundary condition can in fact be desirable on a coarse mesh, as it imitates the presence of a boundary layer [65–69].

Finding that the penalty $\tau^B = 10^2$ applied to discretization M2 produces quantities of interest that largely agree with our boundary-fitted reference and results from the literature, we proceed to consider the effect of adaptive quadrature with this value of the penalty parameter. These results are collected in Table 4 and again compared with our reference computation. The degradation of results in the absence of adaptive quadrature demonstrates the effects of error introduced by under-integrating discontinuous functions. This degradation becomes more severe with increased Reynolds number, suggesting that adaptive quadrature would be especially crucial in computations involving turbulent flows. The

NIH-PA Author Manuscript

NIH-PA Author Manuscript

NIH-PA Author Manuscript

agreement of the non-boundary-fitted results with those computed on a refined, boundary-fitted reference mesh shows that the non-boundary-fitted methodology is accurate, even when the boundary layer is composed of larger, haphazardly-cut elements.

Remark 8: The results in Table 4 demonstrate interesting correlations: removal of adaptive quadrature consistently increases drag and decreases lift. This suggests that inadequate integration may tend to overestimate viscous forces and underestimate pressure forces, but we do not investigate that question further in this paper.

4. Immersed shell structures

The preceding example involves flow around a bulky object. We would also like to study flow around extremely thin immersed structures, such as heart valve leaflets. The method developed in Section 3 could be applied if the thin structures were fully modeled as 3D solids and immersed into a sufficiently refined fluid mesh. However, we would prefer a computationally more efficient approach that models the solid as a two-dimensional manifold shell structure. Such a technique would necessarily decouple the fluid resolution from the structure thickness.

This presents a conceptual difficulty. The exact solution for the pressure around a shell structure may be discontinuous at the structure. Since, for practical reasons discussed in Section 1, we are committed to using a non-boundary-fitted method, the fluid discretization cannot be informed by the structure's position. This means that our fluid approximation space cannot be selected in such a way that the pressure basis functions are themselves discontinuous at the immersed boundary. This implies an inherent approximation error in the pressure field. This error will converge slowly for polynomial bases [123]. Nonetheless, we believe that solutions of sufficient accuracy for engineering purposes can be obtained in this fashion and we focus on developing a robust method for obtaining these solutions.

4.1. Reduction of Nitsche's method to the penalty method

Consider integrating the boundary terms of Eq. (12) over both sides of a thin immersed shell structure. If the velocity and pressure approximation spaces are continuous through the vanishing thickness of the shell (and the velocity approximation space is continuously differentiable), then the dependence of the consistency and adjoint consistency terms on the normal vector will cause contributions from opposing sides to cancel one another. The only remaining terms will be the penalty and the inflow stabilization. In the case of an immersed shell structure, we may view the inflow term as a velocity-dependent penalty. The Nitsche-type formulation given in Eq. (12) therefore reduces to the following penalty method

NIH-PA Author Manuscript

NIH-PA Author Manuscript

NIH-PA Author Manuscript

$$
\begin{aligned}
&B_1^{\mathrm{VMS}}\left(\{\mathbf{w}_1^h, q^h\}, \{\mathbf{u}_1^h, p^h\}; \hat{\mathbf{u}}^h\right) \\
&\quad - F_1^{\mathrm{VMS}}\left(\{\mathbf{w}_1^h, q^h\}\right) \\
&\quad - \int_{(\Gamma_{\mathrm{I}})^-} \mathbf{w}_1^h \cdot \rho_1 \left(\left(\mathbf{u}_1^h \right.\right. \\
&\qquad \left.\left. - \hat{\mathbf{u}}^h\right) \cdot \mathbf{n}_1 \left(\mathbf{u}_1^h \right.\right. \\
&\qquad \left.\left. - \mathbf{u}_2\right) d\Gamma \right. \\
&\quad + \int_{\Gamma_{\mathrm{I}}} \tau_{\mathrm{TAN}}^B \left(\mathbf{w}_1^h \right. \\
&\qquad \left. - \left(\mathbf{w}_1^h \cdot \mathbf{n}_1\right) \mathbf{n}_1 \cdot \left(\left(\mathbf{u}_1^h \right.\right.\right. \\
&\qquad \left.\left.\left. - \mathbf{u}_2 - \left(\left(\mathbf{u}_1^h \right.\right.\right.\right. \\
&\qquad\quad \left.\left.\left.\left. - \mathbf{u}_2\right) \cdot \mathbf{n}_1\right) \mathbf{n}_1\right) d\Gamma \right. \\
&\quad + \int_{\Gamma_{\mathrm{I}}} \tau_{\mathrm{NOR}}^B \left(\mathbf{w}_1^h \right. \\
&\qquad \left. \cdot \mathbf{n}_1 \left(\left(\mathbf{u}_1^h \right.\right.\right. \\
&\qquad\quad \left.\left.\left. - \mathbf{u}_2\right) \cdot \mathbf{n}_1\right) d\Gamma = 0
\end{aligned}
\tag{26}
$$

when the approximation spaces $\mathcal{V}_u^h$ and $\mathcal{V}_p^h$ are sufficiently regular around the shell. This may be seen as a thin-body analogue to the L^2 penalization technique studied by Angot et al. [124].

Remark 9—Adaptive quadrature is not necessary for fluid elements intersecting only thin immersed structures that are modeled geometrically as surfaces, because the integrands remain essentially smooth when set to zero on a sub-domain of zero Lebesgue measure.

Remark 10—If the shell structure divides Ω_1 into two sub-domains, Ω_1^A and Ω_1^B, we may solve two independent problems for $(\mathbf{u}_1^A, p^A)$ and $(\mathbf{u}_1^B, p^B)$ but discretize both using the same mesh of Ω_1, in the spirit of the extended domain variant of the fluid–structure interface locator technique (FSILT-ED) proposed by Tezduyar [125]. Each sub-domain could be integrated separately, using the adaptive quadrature rule developed in Section 3.2. This would produce a discontinuous fluid Cauchy stress at the immersed surface, preventing the formulation from degenerating into a penalty method and avoiding the interpolation error inherent to approximating a discontinuous pressure with a continuous function. However, this extended domain technique would require additional technical considerations to apply to general immersed structure geometries, and we do not pursue it further in the present work.

To determine the velocity and pressure about an immersed valve in its closed state, a method must be capable of developing nearly hydrostatic solutions in the presence of large pressure gradients. Penalty forces will only exist if there are nonzero violations of kinematic constraints. A pure penalty method rules out the desired hydrostatic solutions: every term that could resist the pressure gradient to satisfy balance of linear momentum depends on velocity. Increasing β may diminish leakage through a structure, but it is a well-known

NIH-PA Author Manuscript

NIH-PA Author Manuscript

NIH-PA Author Manuscript

disadvantage of penalty methods that extreme values of penalty parameters will adversely affect the numerical solvability of the resulting problem. This motivates us to return to Eqs. (2)–(4) and develop a method that does not formally eliminate the multiplier field.

4.2. Reintroducing the multipliers

Since the introduction of constraints tends to make discrete problems more difficult to solve, we will only reintroduce a scalar multiplier field to strengthen enforcement of the no-penetration part of the FSI kinematic constraint, rather than the vector-valued multiplier field of Eqs. (2)–(4). The viscous, tangential component of the constraint will continue to be enforced by only the penalty τ^B_{TAN}. This may be thought of as a formal elimination of just the tangential component of the multiplier field, which also retains the ability to allow the flow to slip at the boundary, which tends to produce more accurate fluid solutions, as discussed in Section 3.1. For clarity, we redefine the FSI boundary terms on the mid-surface of the shell structure, Γ_t, rather than considering the full boundary, Γ_{I}. This means that constants in the current formulation may differ from those of Eqs. (2)–(4) by factors of two. We arrive, then, at the formulation

$$B_1(\{\mathbf{w}_1,q\},\{\mathbf{u}_1,p\};\hat{\mathbf{u}})-F_1(\{\mathbf{w}_1,q\})+\int_{\Gamma_t}\mathbf{w}_1\cdot(\lambda_n\mathbf{n}_2)d\Gamma+\int_{\Gamma_t}\mathbf{w}_1\cdot\beta(\mathbf{u}_1-\mathbf{u}_2)d\Gamma=0, \quad (27)$$

$$B_2(\mathbf{w}_2,\mathbf{u}_2)-F_2(\mathbf{w}_2)-\int_{\Gamma_t}\mathbf{w}_2\cdot(\lambda_n\mathbf{n}_2)d\Gamma-\int_{\Gamma_t}\mathbf{w}_2\cdot\beta(\mathbf{u}_1-\mathbf{u}_2)d\Gamma=0, \quad (28)$$

$$\int_{\Gamma_t}\delta\lambda_n\mathbf{n}_2\cdot(\mathbf{u}_1-\mathbf{u}_2)d\Gamma=0, \quad (29)$$

where λ_n is the new scalar multiplier field and, to emphasize the relation to Eqs. (2)–(4), the penalty force has not been split into normal and tangential components. The consistency and adjoint consistency terms associated with eliminating the tangential component of the multiplier have been omitted under the assumption that they will vanish after integrating over both sides of the thin shell, as discussed in Section 4.1.

4.2.1. Implementation of the Lagrange multipliers—We wish to implement the constraint between the fluid and structure solutions in a way that is minimally disruptive to the two subproblems, allowing existing methods for computational fluid and solid mechanics to be applied to each. A monolithic solution for the velocities and multipliers would limit our ability to quickly interchange fluid or structure formulations and, as a mixed formulation, would require either special choices of approximation spaces [103] or additional stabilization terms to satisfy the Babuška–Brezzi stability conditions. Appropriate approximation spaces or stabilization terms are not obvious for the current case. Barbosa and Hughes [126] developed a stabilization scheme to circumvent the Babuška–Brezzi conditions when using Lagrange multipliers to enforce Dirichlet boundary conditions on elliptic problems. While this has been successfully applied to enforce kinematic constraints between bulky immersed bodies and Stokes flow [127], several key terms in the formulation are linear in the boundary normal vector, and, for thin immersed bodies, will cancel in the

NIH-PA Author Manuscript

NIH-PA Author Manuscript

NIH-PA Author Manuscript

same manner as the consistency and adjoint consistency terms of Nitsche's method (cf. Section 4.1). This section discusses two alternative solution strategies for implementing the Lagrange multipliers.

The unconstrained problem that follows from considering λ_n to be fixed in Eqs. (27)–(29) is similar to that following from the penalty method. The multiplier simply enters each subproblem as a prescribed boundary traction. We consider, then, an iterative strategy that updates λ_n between solutions of such unconstrained problems.

Our starting point is the iterative method independently introduced by Hestenes [128] and Powell [129] in 1969. This method attempts to minimize an augmented Lagrangian of the form

$$L(x,\lambda)=f(x)+\lambda g(x)+\beta\|g(x)\|^2 \quad (30)$$

where x is the primal variable, λ is the multiplier, $\beta > 0$ is a penalty parameter, and $f(x)$ is an objective function that we seek to minimize, subject to the constraint $g(x) = 0$. The method consists of starting with $\lambda = 0$ and repeating the steps

1. Solve $x \leftarrow \arg\min L(\cdot, \lambda)$, where λ is treated as a fixed parameter.
2. Update the multiplier by $\lambda \leftarrow \lambda + \beta g(x)$,

until $\|g(x)\| < \varepsilon$. This algorithm may be characterized as a more robust implicit version of the well known Uzawa iteration [130]. In Uzawa iteration, penalty forces are not included in the unconstrained minimization of step 1, and the size of β is consequently limited by stability considerations during the multiplier update of step 2, potentially leading to very slow convergence [131–133]. We may attempt to devise a related algorithm for our problem by representing the field λ_n with samples at quadrature points of Γ_t and repeating the following steps:

1. Solve for approximate fluid and structure velocities $\mathbf{u}_1^h$and $\mathbf{u}_2^h$, treating λ_n as fixed data. We discuss specific solution strategies for this unconstrained (but still coupled) problem in Section 4.6.
2. Update the multiplier field by $\lambda_n \leftarrow \lambda_n+\tau^B_{\mathrm{NOR}}(\mathbf{u}_1^h - \mathbf{u}_2^h)\cdot\mathbf{n}_2$, where λ_n and $\mathbf{u}_i^h$ are evaluated at the quadrature points of Γ_t,

until $\left(\int_{\Gamma_t}|(\mathbf{u}_1^h - \mathbf{u}_2^h)\cdot\mathbf{n}_2|^2 d\Gamma\right)^{1/2}<\varepsilon$.

However, if the approximation spaces are not selected in a stable way, there may not be a solution to the discrete problem and the iteration may never converge to arbitrary ε. In the limit that the quadrature rule over Γ_t is exact, it is clear that attainable values of ε will be bounded below by the error inherent to interpolating functions in the structure's discrete velocity space with those in the non-matching trace of the fluid's discrete velocity space. We observe that, in some cases, specifically those discussed in Section 4.4, the iteration converges linearly. However, for more general fluid and structure geometries, the procedure does not appear to converge. It may be possible, and practically effective, to formulate a

NIH-PA Author Manuscript

NIH-PA Author Manuscript

NIH-PA Author Manuscript

variety of *ad hoc* termination criteria, such as *h*-dependent formulas for ε that account for the mismatch between fluid and structure discrete velocity spaces, but, for problems in which the iterative procedure will not converge, we consider only the case of applying a single iteration within each time step and using the updated λ_n as the initial guess for the (severely truncated) iteration within the next time step. In this case, the multiplier becomes an accumulation of penalty tractions from previous time steps. This is equivalent to replacing the multiplier and normal penalty terms

$$\int_{\Gamma_t}(\mathbf{w}_1-\mathbf{w}_2)\cdot(\lambda_n\mathbf{n}_2)d\Gamma+\int_{\Gamma_t}((\mathbf{w}_1-\mathbf{w}_2)\cdot\mathbf{n}_2)\tau^B_{\mathrm{NOR}}((\mathbf{u}_1-\mathbf{u}_2)\cdot\mathbf{n}_2)d\Gamma \quad (31)$$

by a penalization of (a backward Euler evaluation of) the time integral of pointwise normal velocity differences on the immersed surface Γ_t

$$\int_{\Gamma_t}\left\{\frac{\tau^B_{\mathrm{NOR}}}{\Delta t}(\mathbf{w}_1(\mathbf{x},t)-\mathbf{w}_2(\mathbf{x},t))\cdot\mathbf{n}_2(\mathbf{x},t)\int_0^t\left(\mathbf{u}_1(\varphi_\tau(\varphi_t^{-1}(\mathbf{x})),\tau)-\mathbf{u}_2(\varphi_\tau(\varphi_t^{-1}(\mathbf{x})),\tau)\right)\cdot\mathbf{n}_2(\varphi_\tau(\varphi_t^{-1}(\mathbf{x})),\tau)d\tau\right\}d\Gamma, \quad (32)$$

where $\varphi_\tau(\mathbf{X})$ gives the spatial position at time τ of material point $\mathbf{X}\in\Gamma_0$ and the measure $d\Gamma$ corresponds to the integration variable $\mathbf{x}\in\Gamma_t$. That the time integral in Eq. (32) is evaluated using the backward Euler method is demonstrated in the following exposition. First define (at fixed **X**)

$$I(t)=\frac{\tau^B_{\mathrm{NOR}}}{\Delta t}\int_0^t(\mathbf{u}_1(\tau)-\mathbf{u}_2(\tau))\cdot\mathbf{n}_2(\tau)d\tau. \quad (33)$$

The time rate-of-change of the integral *I* will be its integrand

$$\dot{I}=\frac{\tau^B_{\mathrm{NOR}}}{\Delta t}(\mathbf{u}_1-\mathbf{u}_2)\cdot\mathbf{n}_2. \quad (34)$$

We approximate *I* at time $t^{n+1+\alpha f}$ by

$$I^{n+1+\alpha_f}=I^{n+\alpha_f}+\Delta t\dot{I}^{n+1+\alpha_f} \quad (35)$$

where $I^{n+\alpha f}$ is an accumulation of previous single-iteration approximations to λ_n and $\Delta t\dot{I}^{n+1+\alpha f}$ is the current time step's penalty forcing, which is the penalty τ^B_{NOR} times the α-level[1] velocity difference between the structure and fluid. Eq. (35) is precisely the backward Euler algorithm for computing *I*. Thus the term of Eq. (32) is accounted for in a fully implicit manner within the discrete solution process, using a manifestly stable time integrator. An order of accuracy is lost relative to the generalized-α scheme, but, in our application, other considerations have driven the time step down to small enough values for this distinction to have few practical implications; we are primarily concerned with stability.

Integrating a constraint residual in time is not a new concept for approximation of a Lagrange multiplier. The differential equation given in Eq. (34) resembles the method of

[1]See Bazilevs et al. [54] for a discussion of generalized-α time integration using this notation.

NIH-PA Author Manuscript

NIH-PA Author Manuscript

NIH-PA Author Manuscript

artificial compressibility, devised by Chorin [134] in 1967 and widely used since to simulate incompressible flows (see, e.g., Brooks and Hughes [80]). In this method, the approximated Lagrange multiplier p representing the pressure evolves through time in an analogous way to I:

$$\partial_t p = -\frac{1}{\delta}\nabla \cdot \mathbf{u}_1, \quad (36)$$

where the constraint is $\nabla \cdot \mathbf{u}_1 = 0$ (instead of $(\mathbf{u}_1 - \mathbf{u}_2) \cdot \mathbf{n}_2 = 0$), $1/\lambda$ is the penalty parameter, and the difference in sign is due to the arbitrary choice of sign with which λ enters the augmented Lagrangian formulation (1). A physical interpretation of this, similar to Chorin's original formulation of Eq. (36) in terms of a fictitious density variable, is that we are penalizing a displacement penetration of the fluid through the leaflet, using the penalty $\tau^B_{\mathrm{NOR}}/\Delta t$. This interpretation makes clear how penalizing the time integral of velocity prevents the steady creep of flow through a barrier.

4.3. Relation to the feedback method of enforcing Dirichlet boundary conditions

The degeneration of Nitsche's method to a velocity penalty and the continuous interpretation of our algorithm for computing Lagrange multipliers may both be interpreted as special cases of an existing framework for enforcing Dirichlet boundary conditions on the unsteady Navier–Stokes equation. Goldstein et al. [135] proposed to apply concentrated surface forcing of the form

$$\mathbf{f}(\mathbf{x}_s, t) = \alpha \int_0^t \mathbf{u}_1(\mathbf{x}_s, \tau) d\tau + \beta \mathbf{u}_1(\mathbf{x}_s, t), \quad (37)$$

for all $\mathbf{x}_s$ on a stationary solid boundary (i.e. $\mathbf{u}_2 = \mathbf{0}$) with (dimensional) parameters $\alpha \leq 0$ and $\beta \leq 0$. Goldstein et al. interpret this method, which we will refer to as the feedback method, in the context of control theory, arguing heuristically that it provides negative feedback in the case of constraint violation. This method was investigated further by Goldstein et al. [136] and Fadlun et al. [137].

The penalty formulation that follows from applying Nitsche's method to thin immersed structures is the feedback method with $\alpha = 0$ and $\beta < 0$, while the time-continuous interpretation of our single-iteration Lagrange multiplier approximation corresponds to the feedback method with $\alpha < 0$ and $\beta = 0$ in the normal direction and $\alpha = 0$ and $\beta < 0$ in the tangential direction. Because we integrate the feedback terms implicitly, the choice of time step relative to α and β is not subject to the stability restriction given by Goldstein et al. [135, Eq. (5)] for the case of explicit time marching. If the iterative approximation of multipliers is formulated to include a relaxation factor, $r \leq 1$, in the multiplier update (i.e. $\lambda_n \leftarrow \lambda_n + r\tau^B_{\mathrm{NOR}}(\mathbf{u}_1^h - \mathbf{u}_2^h) \cdot \mathbf{n}_2$, as originally proposed by Hestenes [128]), then the time-continuous interpretation of the single iteration case would, for $r < 1$, be the feedback method with $\alpha < 0$ and $\beta < 0$. This possibility may lead to enhanced stability, but is not investigated in the present work.

NIH-PA Author Manuscript

NIH-PA Author Manuscript

NIH-PA Author Manuscript

4.4. Managing pressure approximation error with stabilization

Due to the poor approximation properties of a pressure space that does not allow discontinuities on the surface of the shell, we expect the pressure to converge slowly with refinement. In problems with large pressure jumps, unphysical compression incurred by the poorly-approximated pressure will ruin even the qualitative character of solutions. In Section 4.4.1, we use a model problem to show that this effect becomes practically important in the analysis of heart valves. Then, in Section 4.4.2, we introduce and test a proposed solution.

4.4.1. A demonstration of the effect of pressure approximation error—We now consider a simplified model of a closed valve, with fluid properties and boundary conditions similar to those found in cardiovascular applications. We show that we cannot develop hydrostatic solutions with a reasonable spatial discretization and practical time step.

Consider an axis-aligned 2 cm × 2 cm × 2 cm cube, filled with an incompressible Newtonian fluid of density $\rho_1 = 1.0$ g/cm^3 and viscosity $\mu = 3.0 \times 10^{-2}$ g/(cm s). The vertical faces have a no-slip boundary condition, the bottom has a zero-traction outflow boundary condition, and the top has a pressure traction of 120 mmHg. The length scale, fluid properties, and pressure difference produce conditions comparable to those surrounding a closed aortic valve in diastole. Now consider immersing a rigid, impermeable horizontal plate into this cube, blocking its entire cross section at a distance of 1.1 cm from the bottom. The exact solution for this problem should be hydrostatic, with a discontinuous pressure at the location of the plate. However, in an immersogeometric discretization, the continuity of the pressure approximation functions through the plate means that the discontinuity of the exact solution cannot be reproduced in a computation.

Remark 11: The plate's height of 1.1 cm is deliberately selected so that the plate will never coincide with an element boundary for any uniform division of the cube into 2^n elements in the z-direction. This may be seen by considering the fact that 0.1_{10} is a repeating fraction in binary. Even if a discontinuous pressure basis is used, the discontinuities will not be located on the structure.

We now compute a solution to this problem, starting from homogeneous initial conditions for the velocity and using Lagrange multipliers to enforce the no-penetration condition on the shell. For the mesh, we use a trivariate C^1-continuous quadratic B-spline patch, uniformly refined into 8 × 8 × 32 elements. The quadrature rule for surface integrals over the immersed plate is a sum of Gaussian quadrature rules on 40×40 quadrilaterals, evenly dividing a 3 cm × 3 cm square surface, cutting through the channel as shown in Figure 7. Surface quadrature points falling outside of the channel do not contribute to integrals. We find that, if large flow velocities develop with the given boundary conditions, backflow divergence may occur, and we apply the outflow stabilization discussed in Section 3.1.1 to both traction boundaries, with $\gamma = 0.5$.

We consider the time step $\Delta t = 10^{-4}$ s practical for computing dynamic FSI at the time scale of a cardiac cycle. Computing with this time step and using the iterative multiplier approximation of Section 4.2.1, we see a highly unphysical behavior. Figure 8 shows the

NIH-PA Author Manuscript

NIH-PA Author Manuscript

NIH-PA Author Manuscript

vertical velocity component on a slice of the resulting solution, after the volumetric flow rate through the top of the cube reached a steady value ($t > 0.01$ s). While the Lagrange multipliers enforce the constraint very effectively[2], there is still a significant flow through the top face of the cube. The steady-state volumetric flow rate is 355.2 mL/s, which is unacceptable for simulation of a valve structure that exists primarily to block flow. This would be a typical flow rate through an *open* aortic valve, during systole [138]. The flow rate varies between cross-sections of the channel, which obviously violates the incompressibility condition.[3] The compression caused by local pressure approximation error pollutes the entire velocity solution.

4.4.2. A proposed solution—The pressure gradient is approximated especially poorly in a neighborhood of the immersed surface. It appears in the fine scale velocity of the VMS formulation, where it is scaled by τ_M. We may diminish the influence of this poorly approximated quantity by locally reducing the value of τ_M. Due to the inverse relationship between τ_M and τ_C, this will also increase the penalization of volume loss in a neighborhood of the immersed surface. We therefore modify the definition of τ_M in Eq. (16) to be

$$\tau_M = \left(s \left(\frac{C_t}{\Delta t^2} + (\mathbf{u} - \hat{\mathbf{u}}) \cdot \mathbf{G} (\mathbf{u} - \hat{\mathbf{u}}) + C_I \nu^2 \mathbf{G} : \mathbf{G} \right) \right)^{-1/2}, \quad (38)$$

which affects all quantities defined in terms of τ_M, such as $\mathbf{u}'$ and τ_C. The new factor $s > 1$ is dimensionless and allowed to vary in space. For most of the domain, $s = 1$, but, in an $O(h)$ neighborhood near the shell, we may make it larger, with the effect of reducing τ_M. To smooth the transition between larger and smaller values of s, we define it as a nodal variable, using the pressure approximation space. For nodes corresponding to pressure basis functions with supports intersecting the shell (i.e. containing quadrature points for the integration rule on Γ_t), this nodal variable is set to $s^{\text{shell}} \geq 1$. For all other nodes, it is set to the usual value of 1. If the pressure shape functions form a partition of unity, then s will be uniformly equal to s^{shell} on elements intersecting the shell.

Remark 12: From stability and convergence analysis of analogous stabilized methods for the steady Stokes and Oseen problems, we see that, for stability and asymptotic convergence, τ_M is subject only to upper bounds. It is typically chosen to saturate these bounds, to reduce constants in the error estimate [84]. However, for flow conditions and approximation spaces of interest, we may improve the qualitative character of solutions at coarse discretizations by reducing τ_M in the vicinity of thin immersed structures (by using $s^{\text{shell}} > 1$).

We now test this preliminary solution by applying it to the model problem of the previous section. We investigate the effect of s^{shell} at the practical time-step size of 10^{-4} s. In Table 5,

As discussed in Section 4.2.1, we do not always expect the constraint to fully converge, since we have not selected a stable discretization, but, in this simple problem, the iteration converges at a roughly linear rate. This is not, in general, expected or found in calculations with different immersed geometries.

[3]The VMS formulation discretely satisfies global mass conservation for any reasonable test space (which may be seen by setting $q = 1$ and $\mathbf{w} = \mathbf{0}$ in Eq. (13)). However, we have no guarantee of local mass conservation.

NIH-PA Author Manuscript

NIH-PA Author Manuscript

NIH-PA Author Manuscript

we compare $s^{\text{shell}} = 1$, $s^{\text{shell}} = 10^4$, and $s^{\text{shell}} = 10^8$, finding that volumetric flow scales roughly like $(s^{\text{shell}})^{-1/2}$, tending to zero as s^{shell} increases.

Remark 13: An undesirable consequence of increasing s^{shell} is that the weakened stabilization near the immersed surface harms the conditioning of the discrete problem. Due to the simplistic nature of the blocked tube model problem, conditioning is not a significant issue, but applying the modified stabilization terms to more complex calculations, such as those presented in Section 5.4, increases the cost of sufficient iterative solution of the linear problem at each Newton step. The development of a suitable preconditioner may avert this difficultly, but is beyond the scope of the current work.

4.5. Treatment of shell structure mechanics

In this section, we give concrete form to the structure subproblem (11). We assume that the structure is a thin shell, represented mathematically by its mid-surface. Further, we assume this surface to be piecewise C^1-continuous and apply the Kirchhoff–Love shell formulation and isogeometric discretization studied by Kiendl et al. [74, 139, 140].

4.5.1. Basic kinematics of a Kirchhoff–Love shell—The spatial coordinates of the shell mid-surface in the current and reference configurations are given by the parametric mappings $\mathbf{x}(\xi_1, \xi_2)$ and $\mathbf{X}(\xi_1, \xi_2)$, respectively. Assuming the range $\{1, 2\}$ for Greek letter indices, we define bases

$$\mathbf{g}_\alpha = \frac{\partial \mathbf{x}}{\partial \xi_\alpha}, \quad (39)$$

$$\mathbf{g}_3 = \frac{\mathbf{g}_1 \times \mathbf{g}_2}{\|\mathbf{g}_1 \times \mathbf{g}_2\|}, \quad (40)$$

and

$$\mathbf{G}_\alpha = \frac{\partial \mathbf{X}}{\partial \xi_\alpha}, \quad (41)$$

$$\mathbf{G}_3 = \frac{\mathbf{G}_1 \times \mathbf{G}_2}{\|\mathbf{G}_1 \times \mathbf{G}_2\|}, \quad (42)$$

in the current and reference configurations, which yield metric tensors

$$g_{\alpha\beta} = \mathbf{g}_\alpha \cdot \mathbf{g}_\beta, \quad (43)$$

$$G_{\alpha\beta} = \mathbf{G}_\alpha \cdot \mathbf{G}_\beta, \quad (44)$$

and curvature coefficients

NIH-PA Author Manuscript

NIH-PA Author Manuscript

NIH-PA Author Manuscript

$$b_{\alpha\beta} = -\mathbf{g}_\alpha \cdot \frac{\partial \mathbf{g}_3}{\partial \xi_\beta} = \frac{\partial \mathbf{g}_\alpha}{\partial \xi_\beta} \cdot \mathbf{g}_3, \quad (45)$$

$$B_{\alpha\beta} = -\mathbf{G}_\alpha \cdot \frac{\partial \mathbf{G}_3}{\partial \xi_\beta} = \frac{\partial \mathbf{G}_\alpha}{\partial \xi_\beta} \cdot \mathbf{G}_3. \quad (46)$$

Using kinematic assumptions and mathematical manipulations given in Kiendl [140], we split the in-plane Green-Lagrange strain $E_{\alpha\beta}$ into membrane and curvature contributions

$$E_{\alpha\beta} = \varepsilon_{\alpha\beta} + \xi_3 \kappa_{\alpha\beta}, \quad (47)$$

where

$$\varepsilon_{\alpha\beta} = \frac{1}{2}(g_{\alpha\beta} - G_{\alpha\beta}), \quad (48)$$

$$\kappa_{\alpha\beta} = B_{\alpha\beta} - b_{\alpha\beta}, \quad (49)$$

are the membrane strain and curvature tensors, respectively, at the shell mid-surface, $\xi_3 \in [-h_{\text{th}}/2, h_{\text{th}}/2]$ is the through-thickness coordinate and h_{th} is the shell thickness, which may, in general, be a function of the mid-surface material coordinates.

4.5.2. St. Venant–Kirchhoff material model—For the purposes of this paper, we assume a St. Venant–Kirchhoff material, in which the second Piola-Kirchhoff stress, **S**, is computed from a constant elasticity tensor, $\mathbb{C}$, applied to **E**. We are well aware of the shortcomings of this material model under states of high compression [141], but these are precluded in the current situation, as transverse normal stress is neglected by the Kirchhoff–Love shell model, and the computations presented in this paper do not involve significant in-plane compression. The in-plane stresses due to extension and bending are integrated through the shell thickness to obtain

$$n^{\alpha\beta} = C^{\alpha\beta\gamma\delta} \varepsilon_{\gamma\delta} h_{\text{th}}, \quad (50)$$

$$m^{\alpha\beta} = C^{\alpha\beta\gamma\delta} \kappa_{\gamma\delta} \frac{h_{\text{th}}^3}{12}. \quad (51)$$

Using the above notation, we specialize the generic structural subproblem by defining

$$B_2(\mathbf{w}, \mathbf{u}) = \int_{\Gamma_t} \mathbf{w} \cdot \rho_2 h_{\text{th}} \left.\frac{\partial \mathbf{u}}{\partial t}\right|_{\mathbf{x}} d\Gamma + \int_{\Gamma_0} (\mathbf{n}:\delta\boldsymbol{\varepsilon} + \mathbf{m}:\delta\boldsymbol{\kappa}) d\Gamma, \quad (52)$$

$$F_2(\mathbf{w}) = \int_{\Gamma_t} \mathbf{w} \cdot \rho_2 h_{\text{th}} \mathbf{f} d\Gamma + \int_{\Gamma_t} \mathbf{w} \cdot \mathbf{h}^{\text{net}} d\Gamma, \quad (53)$$

NIH-PA Author Manuscript

NIH-PA Author Manuscript

NIH-PA Author Manuscript

where Γ_0 and Γ_t are the shell mid-surface in the reference and deformed configurations, respectively, $\mathbf{h}^{\text{net}} = \mathbf{h}(\xi_3 = -h_{th}/2) + \mathbf{h}(\xi_3 = +h_{th}/2)$ sums traction contributions from the two sides of the shell. For isotropic materials, the material tensor may be derived from a Young's modulus, E, and Poisson ratio, ν.

4.5.3. Isogeometric shell discretization—We discretize shell structures isogeometrically, using C^1-continuous quadratic B-spline patches to represent both the reference configuration and the approximate displacement solution. The details of this discretization are given in Kiendl et al. [74, 140]. A noteworthy aspect of this discretization is the fact that it requires no rotational degrees of freedom; our C^1-continuous approximation space (for a single patch) is in H^2, so we may directly apply Galerkin's method to the forms defined in Eqs. (52) and (53). It should be noted that for complex structures, the continuity of the geometrical mapping is often reduced to the C^0 level (e.g. geometries comprised of multiple patches). The problem of reduced continuity across patch boundaries can be resolved by applying linear constraint equations for simple geometries [74], or through the bending strip method [139].

4.6. Time integration and fluid–structure coupling

We apply the same implicit generalized-α scheme that we use for the fluid subproblem in Section 3.3 to coupled FSI problems. Given our variational formulation for the coupled problem, it would be possible, in principle, to simultaneously solve for the fluid, structure, and multiplier solutions at each time step, in a monolithic fashion. However, as discussed in Section 4.2.1, we use an iterative scheme for updating the Lagrange multiplier unknowns, wherein an unconstrained problem with a constant multiplier field is solved one or more times within each time step. For the unconstrained problem, we opt to derive separate tangent matrices for the fluid and structure problems, considering the solution variables of each (along with the multipliers) to be constant in the other's linearization. This is not equivalent to a full linearization of the problem, as it discards some information regarding the coupling of the subproblems. However, the ability to isolate the structural tangent makes the method more modular, easing the implementation of new material models.

For the unconstrained problems at each step of the iteration described in Section 4.2.1, we apply what is called, in the terminology of Tezduyar and Sathe [24], a block-iterative approach. This approach alternates between solving for increments of the fluid and structure solutions. Schematically, consider $R_f(u_f, u_s)$ to be the nonlinear residual for the fully-discrete fluid subproblem at a particular time step, which depends on the discrete fluid and structure solutions, u_f and u_s. Likewise, $R_s(u_f, u_s)$ is the residual for the discrete structure subproblem. Then the block-iterative procedure to find a root of (R_f, R_s) is to start with guesses for u_f and u_s, then repeat the steps

1. Assemble $R_f(u_f, u_s)$ and a (typically approximate) tangent matrix, $A_f \approx \partial R_f / u_f$.
2. Solve the linear system $A_f \Delta u_f = -R_f$ for the fluid solution increment.
3. Update the fluid solution: $u_f \leftarrow u_f + \Delta u_f$.
4. Assemble $R_s(u_f, u_s)$ and $A_s \approx \partial R_s / u_s$.

NIH-PA Author Manuscript

NIH-PA Author Manuscript

NIH-PA Author Manuscript

5. Solve $A_s \Delta u_s = -R_s$ for the structure solution increment.
6. Update the structure solution: $u_s \leftarrow u_s + \Delta u_s$.

until R_f and R_s are sufficiently converged. Note that this resembles Newton iteration with an inexact tangent, wherein off-diagonal blocks of the tangent matrix for the combined system,

$$\begin{pmatrix} A_f & (\partial R_f / \partial u_s) \\ (\partial R_s / \partial u_f) & A_s \end{pmatrix} \begin{pmatrix} \Delta u_f \\ \Delta u_s \end{pmatrix} = - \begin{pmatrix} R_f \\ R_s \end{pmatrix}, \quad (54)$$

are neglected. However, the update of the fluid solution in step 3 distinguishes block iteration from an inexact tangent method. For the computations in this paper, we use the generalized minimum residual method (GMRES) [142] to approximate the solution of step 2 and the conjugate gradient method [143] to approximate the solution of step 5. To ensure predictable running times and avoid stagnation in pathological configurations, we typically select the resolution of the nonlinear algebraic solution by choosing a fixed number of iterations rather than a percentage by which the residual must be reduced. This may be interpreted as a predictor–multi-corrector scheme based on Newton's method [54]. While it is possible that error from isolated, poorly-solved time steps can pollute the future of a solution, we find that, within reasonable limits, quantities of engineering interest are typically more sensitive to spatial and temporal discretizations than nonlinear solution tolerance.

Remark 14—The block-iterative procedure is widely held to be applicable only when the structure's density is much higher than that of the fluid, which is not the case in cardiovascular applications. Van Brummelen [144] investigated this issue analytically, using a model problem, and found that subiterative algorithms alternating between solutions of fluid and structure subproblems become unstable if the fluid is too dense. He further determined that refinement in time cannot resolve this instability if the fluid is incompressible. In the present work, we apply block iteration to couple a structure and incompressible fluid of equal density. However, we are applying block iteration to a problem in which the fluid and structure are coupled using a finite penalty rather than a true constraint. Recall that the Lagrange multiplier field is held fixed in the problem to which we apply block iteration. We find that, for this penalty-coupled problem, block iteration remains robust at practically large penalty values. If $\tau^B_{(\cdot)} \to \infty$ at fixed Δt, the procedure becomes ineffective, but our experience indicates that convergence of the block iterative procedure can be improved by simply reducing the time step. An analysis of the continuous interpretation of our fluid–structure coupling algorithm using the model problem established by van Brummelen may provide more precise conditions for the stability of our approach.

4.7. 2D heart valve benchmark

We now test our immersogeometric method for thin-shell FSI on a heart-valve-inspired benchmark problem investigated previously by Gil et al. [145], Hesch et al. [41], and Wick [91]. To test the methods developed in this paper, we compute this problem using both our immersogeometric technique for FSI and strong kinematic constraint enforcement on an isogeometric boundary-fitted fluid mesh.

NIH-PA Author Manuscript

NIH-PA Author Manuscript

NIH-PA Author Manuscript

4.7.1. Description of the problem—The problem consists of two cantilevered elastic beams immersed in a 2D channel filled with incompressible Newtonian fluid, as shown in Figure 9. The fluid and structure have equal densities of $\rho_1 = \rho_2 = 100$. The viscosity of the fluid is $\mu = 10$. Gil et al. studied a variety of material models for the beams while Hesch et al. used a nearly incompressible neo-Hookean material, with Young's modulus $E = 5.6 \times 10^7$ and Poisson ratio $\nu = 0.4$. In this paper we use the St. Venant–Kirchhoff model described in Section 4.5.2 with $E = 5.6 \times 10^7$ and Poisson ratio $\nu = 0.4$. The top and bottom sides of the channel have no-slip boundary conditions, the left end has a prescribed, time-dependent velocity profile, and the right end is a traction-free outflow. The velocity Dirichlet condition on the left end of the channel is given by the formula

$$\mathbf{u}_1(y\mathbf{e}_2, t) = \begin{cases} 5(\sin(2\pi t)+1.1)y(1.61-y)\mathbf{e}_1, & t>0 \\ \mathbf{0}, & \text{otherwise} \end{cases}, \quad (55)$$

where the origin of the spatial coordinate system is at the bottom left corner of the domain. At times $t < 0$, the fluid and structure are at rest. Taking the channel width of 1.61 as a characteristic length scale and the peak inflow speed of 6.8 as a characteristic flow speed, the Reynolds number is approximately 110.

4.7.2. Boundary-fitted reference computation—The mesh for the boundary-fitted reference computation is shown in Figure 10. The fluid domain consists of 7626 quadratic B-spline elements. Each beam consists of 31 quadratic B-spline elements and is coincident with a line of C^0 continuity in the fluid B-spline space, permitting strong enforcement of fluid–structure kinematic constraints. We use a time-step size of $\Delta t = 0.005$ for the boundary-fitted computation. The selected spatial and temporal resolutions ensure that the displacement history of the upper beam tip changes negligibly (~0.001 length units) with further refinement in both space and time.

The fluid mesh deforms according to the solution of a fictitious isotropic linear elastic problem that takes the location of the beam as a displacement boundary condition. The velocity of this deformation enters into the fluid formulation (13) as $\hat{\mathbf{u}}^h$. This velocity is derived from displacements of the mesh in consecutive time steps. Mesh quality is preserved throughout this deformation by stiffening the fictitious material in response to compression: the material tensor is modified such that the mesh Young's modulus, E_{mesh}, scales inversely with the square of the Jacobian determinant, J_ξ, of the mesh's parametric mapping in the previous time step. More detailed discussions of Jacobian-based mesh stiffening can be found in [28, 54, 146–149]. In the present problem, we also find it necessary to soften the fictitious material governing the deformation of elements between the leaflets. This is accomplished by making its Young's modulus (prior to Jacobian-based stiffening) 1000 times smaller than that of the material adjacent to the leaflets. The regions of softened mesh are highlighted in green in Figure 10. A snapshot of the resulting deformed mesh at time $t = 0.5$ is in Figure 11. The non-smooth deformation visibly demonstrates the effect of the jump in fictitious material parameter.

The parabolic inflow profile given by (55) is represented exactly, using the trace space of the B-spline basis functions. Under the assumption that the geometrical mapping from the

NIH-PA Author Manuscript

NIH-PA Author Manuscript

NIH-PA Author Manuscript

B-spline parameter ξ_2 to the physical y-coordinate is time-independent, linear, and invertible at the inflow face of the domain, the velocity profile may be applied by first pre-computing x-direction velocity coefficients for the left-most row of control points such that the resulting B-spline curve interpolates the function $y(1.61 - y)$ at its Greville abscissae. These coefficients may be scaled by $5(\sin(2\pi t) + 1.1)$ during the computation, to obtain the desired velocity profile at time t.

4.7.3. Immersogeometric computations—We test three immersogeometric discretizations of the problem. The first, which we refer to here as M1, evenly divides the fluid domain into 128 × 32 quadratic B-spline elements and each beam into 64 quadratic B-spline elements. The other two discretizations are uniform refinements of M1: M2 contains 256 × 64 fluid elements and 128 shell elements in each beam, while M3 contains 512 × 128 fluid elements and 256 shell elements in each beam. As in the reference computation, the inflow velocity profile is captured exactly on these meshes. We refine in time alongside spatial refinement, using $\Delta t = 0.01$ with M1, $\Delta t = 0.005$ with M2, and $\Delta t = 0.0025$ with M3.

Because the trace of the background discrete fluid velocity function space along the moving immersed beam does not include arbitrary functions from the beam's velocity space, the iterative method described in Section 4.2.1 for computing pointwise values of a Lagrange multiplier field will not converge. We therefore use the single-iteration truncation of this algorithm, which is interpreted as a modified continuous problem and related to the earlier feedback method of Goldstein et al. [135] in Section 4.2.1. Following the guideline given by Eq. (21), we scale the penalty parameters $\tau^B_{(\cdot)}$ inversely with mesh size, choosing $\tau^B_{(\cdot)} = 10^4$ on M1, $\tau^B_{(\cdot)} = 2 \times 10^4$ on M2, and $\tau^B_{(\cdot)} = 4 \times 10^4$ on M3. The stabilization adjustments of Section 4.4.2 are employed, with $s^{\text{shell}} = 10^6$.

4.7.4. Comparison of results—Figure 12 shows the x- and y-direction displacements of the upper beam tip for the boundary-fitted and immersed computations. The displacement histories computed using our immersogeometric method on M1, M2, and M3 converge toward the boundary-fitted result. Comparisons of the pressure contours at time $t = 0.5$ are given in Figure 13, showing agreement between the immersogeometric and boundary-fitted flow fields in regions outside of an $\mathcal{O}(h)$ neighborhood of the immersed beams. Velocity streamlines at $t = 0.5$ for the background mesh M1 are shown in Figure 14, demonstrating that the velocity field remains smooth on this coarse mesh, in spite of the pressure error evident from Figure 13. This is in contrast to the findings of Baaijens [61], who observed excessive pollution effects in the velocity field when discretizing the pressure about an immersed beam with a continuous approximation space. Compare the velocity streamlines of our Figure 14 with Figure 2 of the cited reference. Baaijens concluded that the use of a discontinuous pressure space "appears to be mandatory" [61, p. 749], but, in the present computations, the use of $s^{\text{shell}} > 1$ diminishes the pollution effects of the localized pressure interpolation error, as demonstrated also in Section 4.4.2, allowing acceptable results with continuous and equal-order pressure/velocity pairs.

It is important to remember that the "pressure" plotted in Figure 13 corresponds to the coarse scale solution variable p^h in the semidiscrete VMS formulation. It omits the fine scale

NIH-PA Author Manuscript

NIH-PA Author Manuscript

NIH-PA Author Manuscript

contribution $p' = -\rho_1 \tau_C \nabla \cdot \mathbf{u}_1$, which dominates near the beams for $s^{\text{shell}} = 10^6$. The coarse scale pressure solution p^h cannot be interpreted physically as mechanical pressure (i.e. $-\frac{1}{3}\text{tr}\boldsymbol{\sigma}_1$) in the band of elements immediately adjacent to the immersed shell structure.

5. Application to a bioprosthetic heart valve

In this section, we use the thin shell immersogeometric FSI method developed in Section 4 to simulate an aortic bioprosthetic heart valve (BHV) and the surrounding blood flow during a cardiac cycle. The aortic valve regulates flow between the left ventricle of the heart and the ascending aorta. Figure 15 provides a schematic depiction of its position in relation to the surrounding anatomy. As mentioned in Section 4.5, the weak form of Kirchhoff–Love shell theory requires the shell geometry to be C^1-continuous. We first describe our strategy of mapping a given valve leaflet geometry to a quadratic B-spline patch. We then address the issue of contact between leaflets. A benefit of using an immersogeometric FSI method is that the contact formulation can be added to the structure subproblem without needing to consider the fluid. We develop a penalty-based dynamic contact algorithm in Section 5.2 and test it in Section 5.3 to show that this method is sufficient for our purposes. Finally, we proceed to compute FSI for the BHV in Section 5.4.

5.1. Valve model

We model the geometry of the prosthetic valve using three quadratic B-spline patches—one for each leaflet. The spline surface for a single leaflet is based on a 23-mm BHV design[4] by Edwards Lifesciences, supplied in the form of a quadrilateral mesh. The spline surface, parameterized as a square in the knot space with $(u, v) \in [0, 1] \times [0, 1]$, is specialized for aortic valve leaflets by degenerating the two edges of spline space ($u = 0$ and $u = 1$) to the two commissure points, as illustrated in Figure 16. We fit the physical space of the B-spline patch to the quadrilateral mesh surface in two stages. To avoid oscillations at the edges, we first fit a piecewise C^1-continuous spline curve to the edges, with C^0 points (repeated knots) at the commissure points. We then fit the interior physical space of the B-spline patch to the interior of the leaflet surface, holding the boundary control points fixed.

The fitting of both the edges and the interior is performed by minimizing the ℓ^2-norm of the Euclidean distances between the vertices of the given quadrilateral mesh, $\{x_i\}$, and their projections onto the spline curve or surface, $\{x_i^p\}$. The control points of the fitted spline, $\{C_j\}$, are therefore the solution of

$$\min \sum_i |x_i - x_i^p|^2 \equiv \min \sum_i \left| x_i - \sum_j N_j(\xi_i^p) C_j \right|^2 \quad (56)$$

where N_j is the basis function associated with the j-th control point and ξ_i^p (in $\mathbb{R}$ for curves and $\mathbb{R}^2$ for surfaces) is the parametric location corresponding to the projected point x_i^p. The

[4]This type of pericardial BHV is fabricated from bovine pericardium sheets that are chemically fixed after being die-cut and mounted onto a metal frame to form the leaflets. As a result, the given geometries are without internal stress and can be used directly as stress-free configurations.

NIH-PA Author Manuscript

NIH-PA Author Manuscript

NIH-PA Author Manuscript

parameters of projected points are determined from the condition that the difference between an input point, x_i, and its projection, x_i^p, should be normal to the curve or surface being fit.

Thus ξ_i^p is the solution of the nonlinear system $(x_i - x_i^p) \cdot \frac{\partial x_i^p}{\partial \xi_i^p} = 0$, which can be found by Newton's iteration. To solve the minimization problem of Eq. (56), we start with an initial guess of $\{C_j\}$, then repeat the steps

1. Compute projected points, $\{x_i^p\}$, and their parameters, $\{\xi_i^p\}$, with the control points, $\{C_j\}$, fixed.
2. Solve the linear least-squares problem for $\{C_j\}$ that is implied by holding $\{\xi_i\}$ fixed in Eq. (56),

until a norm of the change in control point values from one iteration to the next is smaller than some tolerance. The control mesh and the physical images of knot spans of the resulting BHV mesh, prior to any refinement (knot insertions) for analysis purposes, are shown in Figure 17. The refined mesh, which is comprised of 1404 quadratic B-spline elements, is shown in Figure 18.

Remark 15—This method of fitting a B-spline patch to the leaflet can be used for patient-specific valve geometries from in-vivo imaging. The degeneration of two edges to the commissure points provides a physical connection that can be used to map the collagen architecture either in a patient-specific way or in an average sense. More details on mapping the collagen architecture and calculating its average using this method can be found in Aggarwal et al. [150].

Remark 16—The use of small, degenerated elements is not intuitively appealing and indeed appears to inhibit convergence of the nonlinear structure subproblem (11) to machine precision, with our relatively straightforward implementations of Galerkin's method and Newton's iteration. In practice, however, we can reduce the residual sufficiently to obtain meaningful simulation results. The absolute residual norm below which convergence breaks down is more than nine orders of magnitude smaller than the norm of typical external forcing on the valve.

5.2. Contact algorithm

Contact between leaflets is an essential feature of a functioning heart valve. We find that it occurs during both the opening and closing phases. While the kinematic constraint of continuous velocity through the fluid and structure should technically obviate any special treatment of structural contact, weak enforcement of the fluid–structure kinematic constraint allows some structural interpenetration and we find that additional enforcement of structural non-penetration improves the quality of solutions. In this section, we describe the penalty method that we use to model contact and address its physical plausibility. The penalty method has been widely used to handle contact problems [48–50, 75, 151] because of its conceptual simplicity and because it is straightforward to implement.

To handle the contact between leaflets using the penalty method, we wish to penalize the penetration of the leaflets. Because the leaflets are modeled as shell structures, it is not

NIH-PA Author Manuscript

NIH-PA Author Manuscript

NIH-PA Author Manuscript

immediately clear how penetration should be defined; a shell has no interior in which to detect penetrating geometry. However, an aortic valve leaflet, operating under normal anatomical conditions, will contact other leaflets on only one side, motivating the following definition of penetration.

Consider leaflets S_1 and S_2 to be smooth parametric surfaces in $\mathbb{R}^3$. For $\mathbf{x}_1 \in S_1$, with surface normal $\mathbf{n}_1$ determining the side on which contact will occur, we say that $\mathbf{x}_1$ contacts leaflet S_2 if the following conditions are met:

1. There exists a point $\mathbf{x}_2 \in S_2$ with normal $\mathbf{n}_2$ such that $(\mathbf{x}_1 - \mathbf{x}_2)$ is perpendicular to S_2. We call $\mathbf{x}_2$ the closest point on S_2 to $\mathbf{x}_1$, but, without additional assumptions on S_2, the defining conditions guarantee neither that $\mathbf{x}_2$ is unique nor that it minimizes $|\mathbf{x}_1 - \mathbf{x}_2|$. In practice, we determine $\mathbf{x}_2$ by iteratively solving the nonlinear problem of finding $\xi = (\xi_1, \xi_2)$ in the parameter space for S_2 such that

$$\begin{cases} (\mathbf{x}_1 - \mathbf{x}_2(\xi)) \cdot \frac{\partial \mathbf{x}_2(\xi)}{\partial \xi_1} = 0 \\ (\mathbf{x}_1 - \mathbf{x}_2(\xi)) \cdot \frac{\partial \mathbf{x}_2(\xi)}{\partial \xi_2} = 0 \end{cases} . \quad (57)$$

2. $|\mathbf{x}_1 - \mathbf{x}_2| < c$, where $c > 0$ is a parameter chosen to avoid false positive contact of distant geometry. We assume that penalties will be strong enough to prevent penetrations larger than c.

For a contacting point $\mathbf{x}_1$, its signed penetration is defined as $d = (\mathbf{x}_2 - \mathbf{x}_1) \cdot \mathbf{n}_2$. We consider $\mathbf{x}_1$ to penetrate S_2 if $d > -h$, where $c > h \geq 0$ indicates a minimum desired distance between the contacting sides of S_1 and S_2. When $d > 0$, we add the condition that $|\mathbf{n}_1 \cdot \mathbf{n}_2| > \alpha$, for some $0 \leq \alpha < 1$. Choosing $\alpha > 0$ allows a hinge-like boundary between S_1 and S_2 that can open through angles larger than 270° without immediately incurring a contact penalty. This notation is illustrated for a pair of contacting points in Figure 19.

Non-penetration is enforced weakly, by penalizing $d > -h$. To motivate our contact algorithm, consider adding the following term

$$\int_{S_1} \left(\left((\mathbf{w}_2)^2 - (\mathbf{w}_2)^1 \right) \cdot \mathbf{n}_2 \right) (kd^+) d\Gamma \quad (58)$$

to the left-hand side of Eq. (11). This term tests a penetration residual against a difference of weighting functions, $(\mathbf{w}_2)^1$ and $(\mathbf{w}_2)^2$, where $(\mathbf{w}_2)^i$ is the structure weighting function on surface i. The term is not a rigorous formulation because the change-of-variables to integrate $(\mathbf{w}_2)^2$ over S_1 is not precisely defined and the definition of d is ambiguous. With some regularity assumptions on S_1 and S_2, and c sufficiently small, we could treat the leaflets as manifolds and use the tubular neighborhood theorem of differential geometry to assert the existence of a well-behaved mapping between contacting regions, but we do not have a constructive estimate for the bound on c, and prefer to disambiguate our formulation in an *ad hoc* manner, by simply detailing our discrete implementation below.

NIH-PA Author Manuscript

NIH-PA Author Manuscript

NIH-PA Author Manuscript

We test for penetration and apply penalty forces at a discrete set of contact points, $\{\mathbf{x}_1^1, \ldots, \mathbf{x}_1^n\} \subset S_1$. For the subset $\{\mathbf{x}_1^{j_k}\}$ contacting $\{\mathbf{x}_2^{j_k}\} \subset S_2$, we apply opposing forces on S_2, conserving linear momentum. To conserve angular momentum, the contact forces between $\mathbf{x}_1$ and $\mathbf{x}_2$ are along their separation $\mathbf{x}_1 - \mathbf{x}_2$, which is, by construction, parallel to $\mathbf{n}_2$. The force on $\mathbf{x}_1$ is $\mathbf{f}_1 = -w(P_k(d))\mathbf{n}_2$ and the force on $\mathbf{x}_2$ is $\mathbf{f}_2 = -\mathbf{f}_1$, where w is a weight associated to $\mathbf{x}_1$ and $P_k(d)$ penalizes penetration. For our computations, we use the penalty function

$$P_k(d) = \begin{cases} \frac{k}{2h}(d+h)^2, & d \in (-h, 0) \\ kh/2 + kd, & d \geq 0 \\ 0, & \text{otherwise} \end{cases}, \quad (59)$$

where k decides the strength of the position penalty. The behavior of P_k on the interval $-h < d < 0$, illustrated in Figure 20, ensures that the penalty activates smoothly as contact begins, helping us to resolve the nonlinearity through Newton's iteration. Motivated by Eq. (58), we choose $\{\mathbf{x}_1^j\}$ to be Gaussian integration points on elements of S_1 and weight forces using the corresponding integration rule. In general, we expect the contact parameters to scale like

$$k = c_1 E/\Delta x \quad (60)$$

$$h = c_2 \Delta x \quad (61)$$

where Δx is a measure of the structural element size. In this paper, however, we focus on a single application and use values determined effective through numerical experiments.

The above method does not preserve geometrical symmetries. To see this, consider contacting planes at an angle; the directions of contact forces depend on the choice of S_1 and S_2, as shown in Figure 21. To ensure that results are independent of this arbitrary distinction, we compute forces with both choices and sum the results. To prevent the introduction of contradictory constraints by this double application of our algorithm, we continuously re-evaluate the contact points $\{\mathbf{x}_2^{j_k}\}$ over time and throughout the nonlinear iteration[5] at each time step.

Remark 17—In the terminology of Sauer and De Lorenzis [152], our method of symmetrizing the contact forces is a classical two-pass contact algorithm. We could alternatively consider omitting the forces on $\{\mathbf{x}_2^{j_k}\}$ during each application of the contact algorithm, which would correspond to the double half-pass technique proposed by Sauer and De Lorenzis [152]. This does not, in general, enforce momentum balance, but the cited study found the double half-pass algorithm to be more stable and computationally efficient, while recovering momentum balance to high accuracy at reasonable levels of refinement.

[5]Our linearization does not account for nonlinearity arising from the dependence of the parameters of the closest point on the displacement solution, but the resulting inexact tangent appears practically effective in spite of this omission.

NIH-PA Author Manuscript

NIH-PA Author Manuscript

NIH-PA Author Manuscript

5.3. Dynamic simulation of a heart valve, with prescribed pressure loading

To test the suitability of our contact algorithm for the simulation of an aortic valve, we apply a physiological transvalvular pressure load in a dynamic simulation of a BHV. This eliminates the complexity associated with FSI while exercising the contact method at appropriate velocities and pressures. Further, we can expect to produce symmetrical results in this simplified setting, while the same cannot be assumed of FSI calculations [58]. Our testing loosely emulated the dynamic simulation by Kim et al. [6], but, due to differences in geometry and material parameters, we do not expect to precisely reproduce the results of the cited study.

5.3.1. Description of the problem—This simulation uses the valve geometry discussed in Section 5.1 and an isotropic St. Venant– Kirchhoff material with $E = 10^7$ dyn/cm^2 and $\nu = 0.45$. The order of magnitude of the Young's modulus is chosen to give a comparable stiffness (at small strains) to the Fung model assumed by Kim et al. [6]. The Poisson ratio is chosen to approximate incompressibility. The thickness of the leaflets is 0.0386 cm and the density is 1.0 g/cm^3. We use the contact algorithm discussed in Section 5.2, setting the parameters to $k = 10^8$ dyn/cm^3, $h = 0.005$ cm, $\alpha = 0.7$, and $c = 0.1$ cm. The time-step size used in the dynamic simulation is 0.0001 s and the pinned boundary condition is applied to the leaflet attachment edge as shown in Figure 18.

In accordance with the expected contact pattern and the convention established in Section 5.2, the surface normal, **n**, points from the aortic to the ventricular side of each leaflet. We model the transvalvular pressure (i.e. pressure difference between left ventricle and aorta) with the traction $-P(t)\mathbf{n}$, where $P(t)$ is the pressure difference at time t, taken from the profile used by Kim et al. [6] and reproduced in Figure 22. The duration of a single cardiac cycle is 0.76 s.

As in the computations of Kim et al. [6], we use damping to model the viscous and inertial resistance of the surrounding fluid. We apply a traction of $-C\mathbf{v}$, where **v** is the leaflet velocity and $C = 80$ g/(cm^2 s). This value of C is selected to ensure that the valve opens at a physiologically reasonable time scale when the given pressure is applied.

5.3.2. Results and discussion—The deformation and strain distribution of the leaflets at several points in the cardiac cycle (after reaching a periodic solution) is illustrated in Figure 23. The opening begins in a manner that is qualitatively similar to the results computed by Kim et al. [6], but the fully-open state differs, in that the belly regions of the leaflets do not snap through to become concave toward the ventricular side. We find that this snap-through behavior (with our choice of constitutive model) is sensitive to the level of damping and slight variations in the leaflet geometry. The purpose of the present computation, however, is largely to test the robustness of the contact algorithm in the impacting and closed states, so we do not dwell on the details of the fully-open configuration. The pressurized diastolic state exhibits much greater sagging of the belly region; this is presumably because our simplified material neglects the stiffening of true tissue under strain. The important conclusion for our contact algorithm is that the results do not show noticeable penetrations under physiological pressure levels and there are no

NIH-PA Author Manuscript

NIH-PA Author Manuscript

NIH-PA Author Manuscript

spurious asymmetries. Note that in our computation, no symmetry planes are assumed between the leaflets. The symmetric pattern is obtained as a result of the symmetric implementation of the contact algorithm described at the end of Section 5.2. We may therefore proceed to FSI simulation with the same contact parameters and conclusively attribute any asymmetries in the FSI results to the effects of the fluid.

5.4. FSI simulation

In this section, we immerse the BHV model of Section 5.1 into a pressure-driven incompressible flow through a rigid channel. The fluid properties are the same as those used in the blocked channel model problem of Figure 7: $\rho_1 = 1.0$ g/cm^3 and $\mu = 3.0 \times 10^{-2}$ g/(cm s). These parameters model the physical properties of human blood[153, 154]. As in the structural dynamics computation of Section 5.3, the valve leaflets have material properties $E = 10^7$ dyn/cm^2 and $\nu = 0.45$. The thickness and density of the leaflets are again 0.0386 cm and 1.0 g/cm^3, respectively.

5.4.1. Parameters of the numerical scheme—In this study, we compare the results of using $\Delta t = 1.0 \times 10^{-4}$ s and $\Delta t = 0.5 \times 10^{-4}$ s. The results of Section 4.4 indicate that, to compute solutions without excessive volume loss, we must modify s^{shell}. Taking Table 5 as a guide for the effects of s^{shell} on volumetric flow through a closed valve, we choose $s^{\text{shell}} = 10^6$. With the complex time-dependent geometry of the immersed leaflets, the iterative approximation of Lagrange multipliers discussed in Section 4.2.1 does not converge. We therefore opt to use the single-iteration approximation of multipliers. Section 4.2.1 discusses this approximation and compares it to the method of artificial compressibility for incompressible flows and also to a penalization of the displacement difference between the fluid and structure. We find that results are relatively insensitive to the tangential FSI penalty, τ^B_{TAN}, but conditioning and nonlinear convergence improve with lower values. For the heart valve, we use a value of $\tau^B_{\text{TAN}} = 2.0 \times 10^2 \text{g}/(\text{cm}^2\text{s})$. The no-penetration boundary condition is more critical to the valve's behavior, and, in the computations that follow, we use the higher value of $\tau^B_{\text{NOR}} = 2.0 \times 10^3 \text{g}/(\text{cm}^2\text{s})$.

5.4.2. Channel geometry—The channel geometry, shown in Figure 24, is a circular tube of diameter 2.3 cm and length 16 cm, with a three-lobed dilation near the valve to model the aortic sinus. It is comprised of quadratic NURBS patches, allowing us to exactly represent the circular portions. We use a multipatch design to avoid including a singularity at the center of the cylindrical sections. Cross-sections of this multi-patch design are shown in Figure 25. The mesh contains a total of 57600 quadratic NURBS elements. Refinement is focused near the valve and sinus, as shown in Figure 24. The mesh is also clustered towards the wall to better capture boundary-layer phenomena. The modeling of the sinus, magnified in Figure 26, does not include the flexible wall in the human aorta, but the experiments of Bellhouse and Bellhouse [155] determined that the presence of such a channel dilation near the valve plays an important role in the valve's dynamics.

Remark 18: As in the benchmark computations of Sections 4.7 and 4.4.1, we use comparable spatial resolutions for the fluid and structure meshes. The shell structure

NIH-PA Author Manuscript

NIH-PA Author Manuscript

NIH-PA Author Manuscript

elements are used to define the surface quadrature rule for fluid–structure interface integrals in Eq. (12).

5.4.3. Boundary and initial conditions—The nominal outflow boundary is 11 cm downstream of the valve, located at the right end of the channel, based on the orientation of Figure 24. The nominal inflow is located 5 cm upstream at the left end of the channel. The designations of inflow and outflow are based on the prevailing flow direction during systole, where the valve is open and the majority of flow occurs. In general, fluid may move in both directions and there is typically some regurgitation during diastole. An idealized left ventricular pressure profile, shown in Figure 27, is applied as a traction boundary condition at the inflow. The duration of a single cardiac cycle used in the FSI computation is 0.86 s. The traction $-(p_0 + RQ)\mathbf{n}_1$ is applied at the outflow, where p_0 is a constant physiological pressure level, Q is the volumetric flow rate through the outflow (with the convention that $Q > 0$ indicates flow leaving the domain), $R > 0$ is a resistance constant, and $\mathbf{n}_1$ is the outward facing normal of the fluid domain. This resistance boundary condition and its implementation are discussed in Bazilevs et al. [99]. In the present computation, we use $p_0 =$ 80 mmHg and $R = 70$ (dyn s)/cm^5. These values ensure a realistic transvalvular pressure difference of 80 mmHg in the diastolic steady state (where Q is nearly zero) while permitting a reasonable flow rate during systole. Such boundary conditions are sufficient to demonstrate the robustness of our thin shell FSI and contact methodologies under the range of relevant flow regimes, but the resistance outflow boundary condition is relatively crude, neglecting several important physical phenomena. Section 5.4.4 points out how this simplified outflow boundary condition affects our solution. For a discussion of more realistic cardiovascular outflow boundary conditions, see Vignon-Clementel et al. [156]. At both inflow and outflow, we apply the backflow stabilization discussed in Section 3.1.1, with $\gamma = 0.5$. On the walls of the channel, we strongly enforce the Dirichlet condition $\mathbf{u}_1 = \mathbf{0}$.

The left ventricular pressure profile of Figure 27 deliberately coincides with p_0 at $t = 0$. In this way, we may begin from an initial condition of $\mathbf{u}_1 = \mathbf{0}$, $\mathbf{u}_2 = \mathbf{0}$, and $\lambda_n = 0$: a stationary, stress-free state. While the fluid–structure interface multiplier, λ_n, is independent of previous history in the continuous formulations (27)–(29), our use of the previous time step's fluid–structure traction as 56 an initial (and, in the single-iteration scheme, only) guess for the multiplier introduces a history dependence, so the initial value of λ_n becomes significant.

To properly seal the gap between the pinned edge of the valve and the channel wall, we extend the pinned edges of the valve leaflets with a rigid stent, as shown in Figure 26. It is important to note that our immersogeometric method does not require this stent to exactly match the channel wall; it extends outside of the fluid domain, much like the rigid plate in the model problem of Section 4.4.

5.4.4. Results and discussion—We now discuss the results of computing with the setup described above. We compute for several cycles from the homogeneous initial condition, until reaching a time-periodic solution. We first consider the volumetric flow through the channel and how its features follow from our boundary conditions. Next, we examine finer features of the fluid solution field. Finally, we compare the deformations of

NIH-PA Author Manuscript

NIH-PA Author Manuscript

NIH-PA Author Manuscript

the valve leaflets to the results of the pressure-driven structural dynamics computation of Section 5.3.

Figure 28 shows the volumetric flow rate through the top of the tube throughout the cardiac cycle. Magnitudes of computed flow rate during systole and diastole are comparable to typical aortic flow rates, but we discuss below several unusual features of the computed profile. The most striking feature of the computed flow profile is the oscillation during diastole. This is a reverberation of the fluid hammer impact on the closing valve. This is a physical phenomenon, not a computational artifact, and is the source of the S2 heart sound, marking the beginning of diastole [157, 158]. A similar decaying flow rate oscillation has been observed *in vitro* with flow loop experiments [159–161]. Further, the frequency of the computed oscillation (about 40 Hz) is within the range of observed aortic heart sound frequencies in patients with recently-implanted bioprosthetic aortic valves [162]. However, the magnitude of our computed oscillation is larger and it decays more slowly.

One may suspect that this prominent oscillation is the result of insufficient fluid–structure coupling, but, if this was the source of the oscillation, we would expect a significant difference between the computations with $\Delta t = 1.0 \times 10^{-4}$ s and $\Delta t = 0.5 \times 10^{-4}$ s, due to the twofold stiffening of the "displacement" penalty coefficient, $\tau^{B}_{\mathrm{NOR}}/\Delta t$, at the smaller time step. With the simplified fluid boundary conditions that we have applied, the oscillation in flow rate is most plausibly a consequence of the physical model, not the numerical method. In the analysis of closed hydraulic systems (such as the cardiovascular system), it is common to consider analogous electrical circuits [163]. The "circuit" that we are modeling is shown in Figure 29. The closed elastic valve acts as a hydraulic accumulator, which is analogous to an electrical capacitor[6]. The inertia of the fluid acts like an inductor. These components, in series with the resistance of viscous forces and the boundary condition, are driven by a pressure difference, which fills the role of a time-varying voltage source in the electrical analogy. The exponentially decaying current oscillation observed in Figure 28 is qualitatively similar to the transient response of the corresponding RLC circuit to a sudden change in voltage. A more sophisticated model might include inductance and capacitance in the boundary conditions, to represent the inertia of blood outside of the computational domain and the Windkessel effect from large elastic arteries. The amplitude of the oscillation may also be exaggerated by our leaflet material model, which approximates the stiffness of a bioprosthetic valve about zero strain. The recruitment of collagen fibers in biological soft tissue leads to an exponential stiffening with strain that we have not attempted to model in this work, so the storage of a given amount of energy requires greater strain with our simplified valve.

Another physiologically unrealistic feature of the computed flow profile is the relatively flat flow rate during systole. Typically, the aortic flow rate reaches a rounded peak. This discrepancy may again be attributed to the simplified boundary conditions. Because the left ventricular pressure in our idealized pressure profile is constant for most of systole and the external flow loop is modeled only by a resistance and pressure difference, we expect the

[6]When current reverses and the valve opens, it will behave more like a resistor. Its overall behavior is not like that of any standard electrical circuit component; the typical analogy between valves and diodes would omit the capacitance in the closed state.

NIH-PA Author Manuscript

NIH-PA Author Manuscript

NIH-PA Author Manuscript

velocity of flow to asymptotically approach a terminal value at which the resistance of viscous forces and the boundary condition exactly balance the difference between the left ventricular pressure and p_0. This is in contrast to the physiological setting, in which flow contributes to a stored pressure as large arteries temporarily expand to accommodate the systolic output of the left ventricle. In the electrical analogy, these arteries act like a reservoir capacitor, smoothing the cardiac output.

The small rise in flow rate at the end of the cycle may seem counter-intuitive, given that the left ventricular pressure is still less than p_0. However, this flow corresponds to the valve returning to its stress-free configuration as the transvalvular pressure goes back to zero. In the electrical analogy, this corresponds to the current released by the capacitor (valve) discharging as the external voltage (pressure) difference is removed.

We now look at the details of the fluid solution fields. In Figure 30, we show several snapshots of the fluid velocity field computed with the smaller time-step size of $\Delta t = 0.5\times10^{-4}$ s. As the valve opens, we see a transition to turbulent flow. This turbulence is exaggerated, in comparison to the physiological case [164], by the flow rate plateau at peak ejection. The valve begins to close under forward flow, as shown by the snapshot at $t = 0.32$ s. The snapshot at $t = 0.35$ s illustrates the fluid hammer effect that initially excites the oscillation evident in the flow rate. After 0.7 s, the S_2 heart sound is decayed and the solution becomes effectively hydrostatic. The fluid solution at $t = 0.7$ s is, however, not trivial. In Figure 31, we show a slice and iso-surface of the corresponding pressure field. The pressure below the valve is nearly zero, as prescribed by the left ventricular profile, and the pressure above the valve is around 106000 dyn/cm^2 (80 mmHg), which is the value chosen for p_0 in the outflow boundary condition. The iso-surface is at $p = 40$ mmHg, halfway between the pressures above and below the valve. It clearly displays the shape of the closed tri-leaflet valve and rigid stent. A careful examination of this figure reveals small pressure oscillations near the valve, visible in both the slice and iso-surface.

This is possibly a result of the weakened fluid stabilization near the structure. The loading produced by the fluid differs significantly from the uniform pressure load prescribed in the computation of Section 5.3. Figure 32 shows the deformations and strain fields of the leaflets at several points during the cardiac cycle. The deformations during systole are markedly different from those computed using only structural dynamics. Specifically, the leaflets remain partially in contact while opening in the FSI simulation, whereas they immediately separate when a pressure load is applied in the structural dynamics computation. The strain field at time $t = 0.35$ s is also interesting in that the strain near the commissure points is significantly higher than it is at $t = 0.7$ s. This is due to the effect of the fluid hammer striking the valve as it initially closes. This phenomenon is completely neglected by both quasi-static and pressure-driven dynamic computations, as neither accounts for the inertia of the fluid. The FSI solution does not preserve the geometrical symmetry of the initial data. This loss of symmetry is typical of turbulent flow and was observed as well in the heart valve FSI computations of Borazjani [58]. This result underscores the importance of computing FSI for the entire valve, without symmetry assumptions.

NIH-PA Author Manuscript

NIH-PA Author Manuscript

NIH-PA Author Manuscript

6. Conclusions

This paper develops several variations of immersogeometric FSI within a variational framework based on the augmented Lagrangian Eq. (1). Prior work has connected this framework to an extension of Nitsche's method for fluid mechanics [63]. We apply this formulation to the CFD benchmark of 2D flow over a cylinder in Section 3.4. When applied to FSI for thin shell structures, modeled geometrically as surfaces, our immersogeometric implementation of Nitsche's method reduces to the penalty method. The penalty method may be effective for some problems, where pressure gradients are not too large. However, we find that for applications such as heart valves, where large pressure gradients develop across thin structures, the penalty method has undesirable properties. We attempt to correct its deficiencies by retaining the Lagrange multiplier as a solution variable. We consider an iterative approximation of the multiplier, based on the work of Hestenes [128] and Powell [129]. For computations in which this method does not converge, we reduce it to the degenerate case of a single iteration in each time step. In that limit, it becomes analogous to Chorin's method of artificial compressibility [134], where the multiplier field solves an auxiliary differential equation in time. The forcing due to the immersed structure may also be interpreted as an application of the feedback method of Goldstein et al. [135].

We find that the approximation error that comes from representing a pressure discontinuity with continuous basis functions leads to poor local mass conservation near the discontinuity. This allows large velocity errors to develop in the rest of the domain. In Section 4.4, we introduce a preliminary work-around that modifies stabilization terms near the immersed structure. This appears to limit local compression without rendering the formulation unstable.

Figure 33 summarizes the interrelationships between the various FSI technologies developed in this work. Combined with a penalty-based contact algorithm for shell structures, these technologies allow us to simulate the dynamics of a BHV immersed and coupled in a cyclic, pressure-driven flow, with physiologically realistic pressure differences. We note that as is typically the case in FSI, different problem features demand different computational strategies.

6.1. Limitations and further work

The current work motivates a number of refinements and extensions that we allude to throughout the body of the paper and summarize below.

- The FSI methods of this paper rely on penalty parameters. We have suggested guidelines, such as Eq. (21), for scaling these penalties with the approximation spaces and physical parameters, but we have not introduced explicit formulas. The appropriate definition of mesh size, "h", is not clear for the case of immersed boundaries. We have, in the computations of this paper, simply used constant penalties deemed effective through numerical experiments.
- We would like to develop a stable formulation to solve for the fluid–structure interface multiplier. As noted above, there is no obvious way to develop an inf-sup

NIH-PA Author Manuscript

NIH-PA Author Manuscript

NIH-PA Author Manuscript

stable approximation space for the multiplier field, but we may be able to work within the framework of stabilized methods [126].

- The suppression of momentum stabilization near immersed shell structures that we develop in Section 4.4 is practically effective but aesthetically unappealing and not thoroughly studied. A theoretical study of the underlying approximation issue may reveal a more elegant solution. Alternatively, because the methods from this paper for enforcing the fluid–structure kinematic constraint are largely independent of the specific formulation for the fluid subproblem, they may easily be combined with variational fluid solvers that do not directly invoke the pressure. For example, the use of a divergence-conforming approximation space for the fluid velocity could be modified to include concentrated boundary forces, while completely eliminating the problem of poor pressure approximation. The Lagrange multiplier (pressure) would no longer be needed to enforce a constraint that is built directly into the solution space. The emerging technology of divergence-conforming B-splines has been successfully applied to unsteady Navier–Stokes and would allow us to combine the advantages of isogeoemetric discretization with pointwise mass conservation [165].
- We discuss the lack of physical realism in our heart valve model at length in Section 5.4.4. To experimentally validate our method for valve simulation, we will need to introduce a more realistic material model for the valve leaflets and more sophisticated boundary conditions for the fluid domain.
- We also plan to use the hierarchical B-spline or NURBS refinement [55]. By hierarchically refining near the structure, one would be able to better resolve the pressure jump and the boundary layer. This could lead to improved results.
- As explained in Remark 1, the proposed immersogeometric framework may be combined with boundary-fitted ALE FSI, to study a BHV implanted in an elastic artery. Preliminary results have been reported in Hsu et al. [166].

Supplementary Material

Refer to Web version on PubMed Central for supplementary material.

Acknowledgements

Funding for this work was supported by NIH/NHLBI grants R01 HL108330 and HL119297, and FDA contract HHSF223201111595P. T.J.R. Hughes was supported by grants from the Office of Naval Research (N00014-08-1-0992), the National Science Foundation (CMMI-01101007), and SINTEF (UTA10-000374) with the University of Texas at Austin. M.-C. Hsu and Y. Bazilevs were partially supported by ARO grant No. W911NF-14-1-0296. D. Kamensky was partially supported by the CSEM Graduate Fellowship. D. Schillinger was partially supported by the German Research Foundation (Deutsche Forschungsgemeinschaft, DFG) under grants SCHI 1249/1-1 and SCHI 1249/1-2. We thank the Texas Advanced Computing Center (TACC) at the University of Texas at Austin for providing HPC resources that have contributed to the research results reported in this paper. We would also like to thank Dr. Laura De Lorenzis at Technische Universität Braunschweig for helpful discussions on the contact problem and related algorithms.

NIH-PA Author Manuscript

NIH-PA Author Manuscript

NIH-PA Author Manuscript

References

1. Schoen FJ, Levy RJ. Calcification of tissue heart valve substitutes: progress toward understanding and prevention. Ann. Thorac. Surg. 2005; 79(3):1072–1080. [PubMed: 15734452]
2. Pibarot P, Dumesnil JG. Prosthetic heart valves: selection of the optimal prosthesis and long-term management. Circulation. 2009; 119(7):1034–1048. [PubMed: 19237674]
3. Siddiqui RF, Abraham JR, Butany J. Bioprosthetic heart valves: modes of failure. Histopathology. 2009; 55:135–144. [PubMed: 19694820]
4. Sun W, Abad A, Sacks MS. Simulated bioprosthetic heart valve deformation under quasi-static loading. J Biomech Eng. 2005; 127(6):905–914. [PubMed: 16438226]
5. Auricchio F, Conti M, Ferrara A, Morganti S, Reali A. Patient-specific simulation of a stentless aortic valve implant: the impact of fibres on leaflet performance. Computer Methods in Biomechanics and Biomedical Engineering. 2014; 17(3):277–285. [PubMed: 22553900]
6. Kim H, Lu J, Sacks MS, Chandran KB. Dynamic simulation of bioprosthetic heart valves using a stress resultant shell model. Annals of Biomedical Engineering. 2008; 36(2):262–275. [PubMed: 18046648]
7. Hughes TJR, Liu WK, Zimmermann TK. Lagrangian–Eulerian finite element formulation for incompressible viscous flows. Computer Methods in Applied Mechanics and Engineering. 1981; 29:329–349.
8. Donea J, Giuliani S, Halleux JP. An arbitrary Lagrangian–Eulerian finite element method for transient dynamic fluid-structure interactions. Computer Methods in Applied Mechanics and Engineering. 1982; 33(1–3):689–723.
9. Donea, J.; Huerta, A.; Ponthot, J-P.; Rodriguez-Ferran, A. Encyclopedia of Computational Mechanics, Volume 3: Fluids. Vol. chapter 14. John Wiley & Sons; 2004. Arbitrary Lagrangian–Eulerian methods.
10. Tezduyar TE, Behr M, Liou J. A new strategy for finite element computations involving moving boundaries and interfaces – the deforming-spatial-domain/space–time procedure: I. The concept and the preliminary numerical tests. Computer Methods in Applied Mechanics and Engineering. 1992; 94(3):339–351.
11. Tezduyar TE, Behr M, Mittal S, Liou J. A new strategy for finite element computations involving moving boundaries and interfaces – the deforming-spatial-domain/space–time procedure: II. Computation of free-surface flows, two-liquid flows, and flows with drifting cylinders. Computer Methods in Applied Mechanics and Engineering. 1992; 94(3):353–371.
12. Figueroa A, Vignon-Clementel IE, Jansen KE, Hughes TJR, Taylor CA. A coupled momentum method for modeling blood flow in three-dimensional deformable arteries. Computer Methods in Applied Mechanics and Engineering. 2006; 195:5685–5706.
13. Torii R, Oshima M, Kobayashi T, Takagi K, Tezduyar TE. Fluid–structure interaction modeling of blood flow and cerebral aneurysm: Significance of artery and aneurysm shapes. Computer Methods in Applied Mechanics and Engineering. 2009; 198:3613–3621.
14. Bazilevs Y, Hsu M-C, Zhang Y, Wang W, Kvamsdal T, Hentschel S, Isaksen J. Computational fluid–structure interaction: Methods and application to cerebral aneurysms. Biomechanics and Modeling in Mechanobiology. 2010; 9:481–498. [PubMed: 20111978]
15. Takizawa K, Bazilevs Y, Tezduyar TE. Space–time and ALE-VMS techniques for patient-specific cardiovascular fluid–structure interaction modeling. Archives of Computational Methods in Engineering. 2012; 19:171–225.
16. Long CC, Hsu M-C, Bazilevs Y, Feinstein JA, Marsden AL. Fluid–structure interaction simulations of the Fontan procedure using variable wall properties. International Journal for Numerical Methods in Biomedical Engineering. 2012; 28:512–527.
17. Torii R, Oshima M, Kobayashi T, Takagi K, Tezduyar TE. Computer modeling of cardiovascular fluid–structure interactions with the Deforming-Spatial-Domain/Stabilized Space–Time formulation. Computer Methods in Applied Mechanics and Engineering. 2006; 195:1885–1895.
18. Takizawa K, Moorman C, Wright S, Spielman T, Tezduyar TE. Fluid–structure interaction modeling and performance analysis of the Orion spacecraft parachutes. International Journal for Numerical Methods in Fluids. 2011; 65:271–285.

NIH-PA Author Manuscript

NIH-PA Author Manuscript

NIH-PA Author Manuscript

19. Takizawa K, Wright S, Moorman C, Tezduyar TE. Fluid–structure interaction modeling of parachute clusters. International Journal for Numerical Methods in Fluids. 2011; 65:286–307.
20. Takizawa K, Spielman T, Tezduyar TE. Space–time FSI modeling and dynamical analysis of spacecraft parachutes and parachute clusters. Computational Mechanics. 2011; 48:345–364.
21. Takizawa K, Tezduyar TE. Computational methods for parachute fluid–structure interactions. Archives of Computational Methods in Engineering. 2012; 19:125–169.
22. Tezduyar TE, Sathe S, Keedy R, Stein K. Space–time finite element techniques for computation of fluid–structure interactions. Computer Methods in Applied Mechanics and Engineering. 2006; 195:2002–2027.
23. Tezduyar TE, Sathe S, Pausewang J, Schwaab M, Christopher J, Crabtree J. Interface projection techniques for fluid–structure interaction modeling with moving-mesh methods. Computational Mechanics. 2008; 43:39–49.
24. Tezduyar TE, Sathe S. Modelling of fluid–structure interactions with the space–time finite elements: Solution techniques. International Journal for Numerical Methods in Fluids. 2007; 54(6–8):855–900.
25. Bazilevs Y, Hsu M-C, Kiendl J, Wüchner R, Bletzinger K-U. 3D simulation of wind turbine rotors at full scale. Part II: Fluid–structure interaction modeling with composite blades. International Journal for Numerical Methods in Fluids. 2011; 65:236–253.
26. Hsu M-C, Bazilevs Y. Fluid–structure interaction modeling of wind turbines: simulating the full machine. Computational Mechanics. 2012; 50:821–833.
27. Korobenko A, Hsu M-C, Akkerman I, Bazilevs Y. Aerodynamic simulation of vertical-axis wind turbines. Journal of Applied Mechanics. 2014; 81:021011.
28. Bazilevs, Y.; Takizawa, K.; Tezduyar, TE. Computational Fluid–Structure Interaction: Methods and Applications. Wiley: Chichester; 2013.
29. Johnson AA, Tezduyar TE. Parallel computation of incompressible flows with complex geometries. International Journal for Numerical Methods in Fluids. 1997; 24:1321–1340.
30. Tezduyar, T.; Aliabadi, S.; Behr, M.; Johnson, A.; Mittal, S. Massively parallel finite element computation of 3D flows – mesh update strategies in computation of moving boundaries and interfaces. In: Ecer, A.; Hauser, J.; Leca, P.; Periaux, J., editors. Parallel Computational Fluid Dynamics – New Trends and Advances. Elsevier: 1995. p. 21-30.
31. Johnson AA, Tezduyar TE. 3D simulation of fluid-particle interactions with the number of particles reaching 100. Computer Methods in Applied Mechanics and Engineering. 1997; 145:301–321.
32. Johnson AA, Tezduyar TE. Advanced mesh generation and update methods for 3D flow simulations. Computational Mechanics. 1999; 23:130–143.
33. Sathe S, Tezduyar TE. Modeling of fluid–structure interactions with the space-time finite elements: Contact problems. Computational Mechanics. 2008; 43:51–60.
34. Takizawa K, Tezduyar TE, Buscher A, Asada S. Space–time interface-tracking with topology change (ST-TC). Computational Mechanics. 2013; 54:955–971.
35. Takizawa K, Tezduyar TE, Buscher A, Asada S. Space–time fluid mechanics computation of heart valve models. Computational Mechanics. 2014; 54:973–986.
36. Cheng R, Lai YG, Chandran KB. Three-dimensional fluid-structure interaction simulation of bileaflet mechanical heart valve flow dynamics. Annals of Biomedical Engineering. 2004; 32(11): 1471–1483. [PubMed: 15636108]
37. Lai YG, Chandran KB, Lemmon J. A numerical simulation of mechanical heart valve closure fluid dynamics. Journal of Biomechanics. 2002; 35(7):881–892. [PubMed: 12052390]
38. Zhang L, Gerstenberger A, Wang X, Liu WK. Immersed finite element method. Computer Methods in Applied Mechanics and Engineering. 2004; 193:2051–2067.
39. Yu Z. A DLM/FD method for fluid/flexible-body interactions. Journal of Computational Physics. 2005; 207:1–27.
40. Gerstenberger A, Wall WA. An eXtended Finite Element Method/Lagrange multiplier based approach for fluid-structure interaction. Computer Methods in Applied Mechanics and Engineering. 2008; 197:1699–1714.

NIH-PA Author Manuscript

NIH-PA Author Manuscript

NIH-PA Author Manuscript

41. Hesch C, Gil AJ, Arranz Carreño A, Bonet J. On continuum immersed strategies for fluid-structure interaction. Computer Methods in Applied Mechanics and Engineering. 2012; 247–248:51–64.
42. Wick T. Fully Eulerian fluid–structure interaction for time-dependent problems. Computer Methods in Applied Mechanics and Engineering. 2013; 255:14–26.
43. Rüberg T, Cirak F. A fixed-grid B-spline finite element technique for fluid–structure interaction. International Journal for Numerical Methods in Fluids. 2014; 74:623–660.
44. Sotiropoulos F, Yang X. Immersed boundary methods for simulating fluid–structure interaction. Progress in Aerospace Sciences. 2014; 65:1–21.
45. Peskin CS. The immersed boundary method. Acta Numerica. 2002; 11:479–517.
46. Mittal R, Iaccarino G. Immersed boundary methods. Annual Review of Fluid Mechanics. 2005; 37:239–261.
47. Hallquist JO, Goudreau GL, Benson DJ. Sliding interfaces with contact-impact in large-scale Lagrangian computations. Computer Methods in Applied Mechanics and Engineering. 1985; 51:107–137.
48. Wriggers P. Finite element algorithms for contact problems. Archives of Computational Methods in Engineering. 1995; 2:1–49.
49. Wriggers, P. Computational Contact Mechanics, 2nd ed. Berlin Heidelberg: Springer-Verlag; 2006.
50. Laursen, TA. Computational Contact and Impact Mechanics: Fundamentals of Modeling Interfacial Phenomena in Nonlinear Finite Element Analysis. Berlin Heidelberg: Springer-Verlag; 2003.
51. Hughes TJR, Cottrell JA, Bazilevs Y. Isogeometric analysis: CAD, finite elements, NURBS, exact geometry, and mesh refinement. Computer Methods in Applied Mechanics and Engineering. 2005; 194:4135–4195.
52. Piegl, L.; Tiller, W. The NURBS Book (Monographs in Visual Communication), 2nd ed. New York: Springer-Verlag; 1997.
53. Sederberg TW, Zheng J, Bakenov A, Nasri A. T-splines and T-NURCCS. ACM Transactions on Graphics. 2003; 22(3):477–484.
54. Bazilevs Y, Calo VM, Hughes TJR, Zhang Y. Isogeometric fluid–structure interaction: theory, algorithms, and computations. Computational Mechanics. 2008; 43:3–37.
55. Schillinger D, Dedè L, Scott MA, Evans JA, Borden MJ, Rank E, Hughes TJR. An isogeometric design-through-analysis methodology based on adaptive hierarchical refinement of NURBS, immersed boundary methods, and T-spline CAD surfaces. Computer Methods in Applied Mechanics and Engineering. 2012; 249–252:116–150.
56. Ruess M, Schillinger D, Bazilevs Y, Varduhn V, Rank E. Weakly enforced essential boundary conditions for nurbs-embedded and trimmed nurbs geometries on the basis of the finite cell method. International Journal for Numerical Methods in Engineering. 2013; 95:811–846.
57. Peskin CS. Flow patterns around heart valves: A numerical method. Journal of Computational Physics. 1972; 10(2):252–271.
58. Borazjani I. Fluid–structure interaction, immersed boundary-finite element method simulations of bio-prosthetic heart valves. Computer Methods in Applied Mechanics and Engineering. 2013; 257(0):103–116.
59. Ge L, Sotiropoulos F. A numerical method for solving the 3D unsteady incompressible Navier–Stokes equations in curvilinear domains with complex immersed boundaries. Journal of Computational Physics. 2007; 225(2):1782–1809. [PubMed: 19194533]
60. Borazjani I, Ge L, Sotiropoulos F. Curvilinear immersed boundary method for simulating fluid structure interaction with complex 3D rigid bodies. Journal of Computational Physics. 2008; 227(16):7587–7620. [PubMed: 20981246]
61. Baaijens FPT. A fictitious domain/mortar element method for fluid–structure interaction. International Journal for Numerical Methods in Fluids. 2001; 35(7):743–761.
62. de Hart, J. Ph.D. thesis. Eindhoven, Netherlands: Technische Universiteit Eindhoven; 2002. Fluid–Structure Interaction in the Aortic Heart Valve: a three-dimensional computational analysis.

NIH-PA Author Manuscript

NIH-PA Author Manuscript

NIH-PA Author Manuscript

63. Bazilevs Y, Hsu M-C, Scott MA. Isogeometric fluid–structure interaction analysis with emphasis on non-matching discretizations, and with application to wind turbines. Computer Methods in Applied Mechanics and Engineering. 2012; 249–252:28–41.
64. Juntunen J, Stenberg R. Nitsche's method for general boundary conditions. Mathematics of Computation. 2009; 78:1353–1374.
65. Bazilevs Y, Hughes TJR. Weak imposition of Dirichlet boundary conditions in fluid mechanics. Computers and Fluids. 2007; 36:12–26.
66. Bazilevs Y, Michler C, Calo VM, Hughes TJR. Weak Dirichlet boundary conditions for wall-bounded turbulent flows. Computer Methods in Applied Mechanics and Engineering. 2007; 196:4853–4862.
67. Bazilevs Y, Michler C, Calo VM, Hughes TJR. Isogeometric variational multiscale modeling of wall-bounded turbulent flows with weakly enforced boundary conditions on unstretched meshes. Computer Methods in Applied Mechanics and Engineering. 2010; 199:780–790.
68. Bazilevs Y, Akkerman I. Large eddy simulation of turbulent Taylor–Couette flow using isogeometric analysis and the residual–based variational multiscale method. Journal of Computational Physics. 2010; 229:3402–3414.
69. Hsu M-C, Akkerman I, Bazilevs Y. Wind turbine aerodynamics using ALE–VMS: Validation and the role of weakly enforced boundary conditions. Computational Mechanics. 2012; 50:499–511.
70. Hughes TJR, Feijóo GR, Mazzei L, Quincy JB. The variational multiscale method–A paradigm for computational mechanics. Computer Methods in Applied Mechanics and Engineering. 1998; 166:3–24.
71. Hughes TJR, Mazzei L, Jansen KE. Large-eddy simulation and the variational multiscale method. Computing and Visualization in Science. 2000; 3:47–59.
72. Akkerman I, Bazilevs Y, Calo VM, Hughes TJR, Hulshoff S. The role of continuity in residual-based variational multiscale modeling of turbulence. Computational Mechanics. 2008; 41:371–378.
73. Bazilevs Y, Calo VM, Cottrel JA, Hughes TJR, Reali A, Scovazzi G. Variational multiscale residual-based turbulence modeling for large eddy simulation of incompressible flows. Computer Methods in Applied Mechanics and Engineering. 2007; 197:173–201.
74. Kiendl J, Bletzinger K-U, Linhard J, Wüchner R. Isogeometric shell analysis with Kirchhoff-Love elements. Computer Methods in Applied Mechanics and Engineering. 2009; 198:3902–3914.
75. De Lorenzis L, Temizer İ, Wriggers P, Zavarise G. A large deformation frictional contact formulation using NURBS-based isogeometric analysis. International Journal for Numerical Methods in Engineering. 2011; 87:1278–1300.
76. Morganti S, Auricchio F, Benson DJ, Gambarin FI, Hartmann S, Hughes TJR, Reali A. Patient-specific isogeometric structural analysis of aortic valve closure. Computer Methods in Applied Mechanics and Engineering. 2014
77. Nitsche J. Uber ein variationsprinzip zur losung von Dirichlet-problemen bei verwendung von teilraumen, die keinen randbedingungen unterworfen sind. Abh. Math. Univ. Hamburg. 1971; 36:9–15.
78. Höllig, K. Finite Element Methods with B-Splines. Philadelphia, Pennsylvania, USA: SIAM; 2003.
79. Bazilevs Y, Hsu M-C, Takizawa K, Tezduyar TE. ALE–VMS and ST–VMS methods for computer modeling of wind-turbine rotor aerodynamics and fluid–structure interaction. Mathematical Models and Methods in Applied Sciences. 2012; 22:1230002.
80. Brooks AN, Hughes TJR. Streamline upwind/Petrov-Galerkin formulations for convection dominated flows with particular emphasis on the incompressible Navier-Stokes equations. Computer Methods in Applied Mechanics and Engineering. 1982; 32:199–259.
81. Tezduyar TE. Stabilized finite element formulations for incompressible flow computations. Advances in Applied Mechanics. 1992; 28:1–44.
82. Tezduyar TE, Osawa Y. Finite element stabilization parameters computed from element matrices and vectors. Computer Methods in Applied Mechanics and Engineering. 2000; 190:411–430.
83. Hughes TJR, Mazzei L, Oberai AA, Wray A. The multiscale formulation of large eddy simulation: Decay of homogeneous isotropic turbulence. Physics of Fluids. 2001; 13:505–512.

NIH-PA Author Manuscript NIH-PA Author Manuscript NIH-PA Author Manuscript

84. Hughes, TJR.; Scovazzi, G.; Franca, LP. Multiscale and stabilized methods. In: Stein, E.; de Borst, R.; Hughes, TJR., editors. Encyclopedia of Computational Mechanics, Volume 3: Fluids. Vol. chapter 2. John Wiley & Sons; 2004.

85. Hsu M-C, Bazilevs Y, Calo VM, Tezduyar TE, Hughes TJR. Improving stability of stabilized and multiscale formulations in flow simulations at small time steps. Computer Methods in Applied Mechanics and Engineering. 2010; 199:828–840.

86. Johnson, C. Numerical solution of partial differential equations by the finite element method. Sweden: Cambridge University Press; 1987.

87. Brenner, SC.; Scott, LR. The Mathematical Theory of Finite Element Methods, 2nd ed. Springer: 2002.

88. Ern, A.; Guermond, JL. Theory and Practice of Finite Elements. Springer: 2004.

89. Evans JA, Hughes TJR. Explicit trace inequalities for isogeometric analysis and parametric hexahedral finite elements. Computer Methods in Applied Mechanics and Engineering. 2013; 123:259–290.

90. Tezduyar TE, Takizawa K, Moorman C, Wright S, Christopher J. Space–time finite element computation of complex fluid–structure interactions. International Journal for Numerical Methods in Fluids. 2010; 64:1201–1218.

91. Wick T. Flapping and contact FSI computations with the fluid–solid interface-tracking/interface-capturing technique and mesh adaptivity. Computational Mechanics. 2014; 53(1):29–43.

92. Taylor CA, Hughes TJR, Zarins CK. Finite element modeling of blood flow in arteries. Computer Methods in Applied Mechanics and Engineering. 1998; 158:155–196.

93. Rispoli F, Corsini A, Tezduyar TE. Finite element computation of turbulent flows with the discontinuity-capturing directional dissipation (DCDD). Computers & Fluids. 2007; 36:121–126.

94. Rispoli F, Saavedra R, Corsini A, Tezduyar TE. Computation of inviscid compressible flows with the V-SGS stabilization and YZβ shock-capturing. International Journal for Numerical Methods in Fluids. 2007; 54:695–706.

95. Rispoli F, Saavedra R, Menichini F, Tezduyar TE. Computation of inviscid supersonic flows around cylinders and spheres with the V-SGS stabilization and YZβ shock-capturing. Journal of Applied Mechanics. 2009; 76:021209.

96. Harari, Isaac; Hughes, Thomas JR. What are C and *h*?: Inequalities for the analysis and design of finite element methods. Computer Methods in Applied Mechanics and Engineering. 1992; 97:157–192.

97. Embar A, Dolbow J, Harari I. Imposing Dirichlet boundary conditions with Nitsche's method and spline-based finite elements. International Journal for Numerical Methods in Engineering. 2010; 83(7):877–898.

98. Ruess M, Schillinger D, Özcan AI, Rank E. Weak coupling for isogeometric analysis of non-matching and trimmed multi-patch geometries. Computer Methods in Applied Mechanics and Engineering. 2014; 269:46–731.

99. Bazilevs Y, Gohean JR, Hughes TJR, Moser RD, Zhang Y. Patient-specific isogeometric fluid-structure interaction analysis of thoracic aortic blood flow due to implantation of the Jarvik 2000 left ventricular assist device. Computer Methods in Applied Mechanics and Engineering. 2009; 198:3534–3550.

100. Esmaily-Moghadam M, Bazilevs Y, Hsia T-Y, Vignon-Clementel IE, Marsden AL. and Modeling of Congenital Hearts Alliance (MOCHA). A comparison of outlet boundary treatments for prevention of backflow divergence with relevance to blood flow simulations. Computational Mechanics. 2011; 48:277–291.

101. Babuška I. Error-bounds for finite element method. Numerische Mathematik. 1971; 16(4):322–333.

102. Brezzi F. On the existence, uniqueness and approximation of saddle-point problems arising from Lagrangian multipliers. ESAIM: Mathematical Modelling and Numerical Analysis - Modélisation Mathématique et Analyse Numérique. 1974; 8:129–151.

103. Hartmann F. The discrete Babuška-Brezzi condition. Ingenieur-Archiv. 1986; 56(3):221–228.

104. Benk, J.; Ulbrich, M.; Mehl, M. The Nitsche method of the Navier–Stokes equations for immersed and moving boundaries. Proceedings of the Seventh International Conference on

NIH-PA Author Manuscript

NIH-PA Author Manuscript

NIH-PA Author Manuscript

Computational Fluid Dynamics, ICCFD7; International Conference on Computational Fluid Dynamics; 2012.

105. Düster A, Parvizian J, Yang Z, Rank E. The finite cell method for three-dimensional problems of solid mechanics. Computer Methods in Applied Mechanics and Engineering. 2008; 197(45–48): 3768–3782.
106. Schillinger D, Ruess M, Zander N, Bazilevs Y, Düster A, Rank E. Small and large deformation analysis with the p- and B-spline versions of the Finite Cell Method. Computational Mechanics. 2012; 50(4):445–478.
107. Schillinger D, Ruess M. The Finite Cell Method: A review in the context of higher-order structural analysis of CAD and image-based geometric models. Archives of Computational Methods in Engineering, accepted for publication. 2014
108. Parvizian J, Düster A, Rank E. Finite cell method. Computational Mechanics. 2007; 41(1):121–133.
109. Hughes, TJR. The finite element method: Linear static and dynamic finite element analysis. Englewood Cliffs, NJ: Prentice Hall; 1987.
110. Stay, PR. Fourth USENIX Computer Graphics Workshop. USENIX Association; 1987. The definition and ray-tracing of B-spline objects in a combinatorial solid geometric modeling system.
111. Chung J, Hulbert GM. A time integration algorithm for structural dynamics with improved numerical dissipation: The generalized-α method. Journal of Applied Mechanics. 1993; 60:371–375.
112. Jansen KE, Whiting CH, Hulbert GM. A generalized-α method for integrating the filtered Navier-Stokes equations with a stabilized finite element method. Computer Methods in Applied Mechanics and Engineering. 2000; 190:305–319.
113. Hsu M-C, Akkerman I, Bazilevs Y. High-performance computing of wind turbine aerodynamics using isogeometric analysis. Computers & Fluids. 2011; 49:93–100.
114. Behr M, Hastreiter D, Mittal S, Tezduyar TE. Incompressible flow past a circular cylinder: Dependence of the computed flow field on the location of the lateral boundaries. Computer Methods in Applied Mechanics and Engineering. 1995; 123:309–316.
115. Ye T, Mittal R, Udaykumar HS, Shyy W. An accurate cartesian grid method for viscous incompressible flows with complex immersed boundaries. Journal of Computational Physics. 1999; 156(2):209–240.
116. Mittal S, Raghuvanshi A. Control of vortex shedding behind circular cylinder for flows at low reynolds numbers. International Journal for Numerical Methods in Fluids. 2001; 35(4):421–447.
117. Lima E Silva ALF, Silveira-Neto A, Damasceno JJR. Numerical simulation of two-dimensional flows over a circular cylinder using the immersed boundary method. Journal of Computational Physics. 2003; 189(2):351–370.
118. Russell D, Wang ZJ. A cartesian grid method for modeling multiple moving objects in 2D incompressible viscous flow. Journal of Computational Physics. 2003; 191:177–205.
119. Wu M-H, Wen C-Y, Yen R-H, Weng M-C, Wang A-B. Experimental and numerical study of the separation angle for flow around a circular cylinder at low Reynolds number. Journal of Fluid Mechanics. 2004; 515:233–260.
120. Chiu PH, Lin RK, Sheu TWH. A differentially interpolated direct forcing immersed boundary method for predicting incompressible Navier–Stokes equations in time-varying complex geometries. Journal of Computational Physics. 2010; 229(12):4476–4500.
121. Rüberg T, Cirak F. Subdivision-stabilised immersed B-spline finite elements for moving boundary flows. Computer Methods in Applied Mechanics and Engineering. 2012; 209–212(0): 266–283.
122. van Brummelen EH, van der Zee KG, Garg VV, Prudhomme S. Flux evaluation in primal and dual boundary-coupled problems. Journal of Applied Mechanics. 2011; 79:010904.
123. Trefethen, LN. Approximation Theory and Approximation Practice. Vol. chapter 9. Philadelphia, Pennsylvania, USA: SIAM; 2012. Gibbs phenomenon.
124. Angot P, Bruneau C-H, Fabrie P. A penalization method to take into account obstacles in incompressible viscous flows. Numerische Mathematik. 1999; 81(4):497–520.

NIH-PA Author Manuscript

NIH-PA Author Manuscript

NIH-PA Author Manuscript

125. Tezduyar TE. Interface-tracking and interface-capturing techniques for finite element computation of moving boundaries and interfaces. Computer Methods in Applied Mechanics and Engineering. 2006; 195:2983–3000.
126. Barbosa HJC, Hughes TJR. The finite element method with Lagrange multipliers on the boundary: circumventing the Babuška-Brezzi condition. Computer Methods in Applied Mechanics and Engineering. 1991; 85(1):109–128.
127. Court S, Fournié M, Lozinski A. A fictitious domain approach for the Stokes problem based on the extended finite element method. International Journal for Numerical Methods in Fluids. 2014; 74(2):73–99.
128. Hestenes MR. Multiplier and gradient methods. Journal of Optimization Theory and Applications. 1969; 4(5):303–320.
129. Powell, MJD. A method for nonlinear constraints in minimization problems. In: Fletcher, R., editor. Optimization. New York: Academic Press; 1969. p. 283-298.
130. Uzawa, H.; Arrow, KJ. Preference, production, and capital. Cambridge University Press; 1989. Iterative methods for concave programming; p. 135-148.Cambridge Books Online.
131. Bacuta C. A unified approach for Uzawa algorithms. SIAM Journal on Numerical Analysis. 2006; 44(6):2633–2649.
132. Stadler G. Path-following and augmented Lagrangian methods for contact problems in linear elasticity. Journal of Computational and Applied Mathematics. 2007; 203(2):533–547.
133. Ito K, Kunisch K. Augmented Lagrangian methods for nonsmooth, convex optimization in Hilbert spaces. Nonlinear Analysis: Theory, Methods & Applications. 2000; 41(5–6):591–616.
134. Chorin AJ. A numerical method for solving incompressible viscous flow problems. Journal of Computational Physics. 1967; 135(2):118–125.
135. Goldstein D, Handler R, Sirovich L. Modeling a no-slip flow boundary with an external force field. Journal of Computational Physics. 1993; 105(2):354–366.
136. Goldstein DB, Tuan T-C. Secondary flow induced by riblets. Journal of Fluid Mechanics. 1998; 363:115–151.
137. Fadlun EA, Verzicco R, Orlandi P, Mohd-Yusof J. Combined immersed-boundary finite-difference methods for three-dimensional complex flow simulations. Journal of Computational Physics. 2000; 161(1):35–60.
138. Uther JB, Peterson KL, Shabetai R, Braunwald E. Measurement of ascending aortic flow patterns in man. Journal of Applied Physiology. 1973; 34(4):513–518. [PubMed: 4698610]
139. Kiendl J, Bazilevs Y, Hsu M-C, Wüchner R, Bletzinger K-U. The bending strip method for isogeometric analysis of Kirchhoff–Love shell structures comprised of multiple patches. Computer Methods in Applied Mechanics and Engineering. 2010; 199:2403–2416.
140. Kiendl, J. PhD thesis. Lehrstuhl für Statik, Technische Universität München; 2011. Isogeometric Analysis and Shape Optimal Design of Shell Structures.
141. Holzapfel, GA. Nonlinear Solid Mechanics: A Continuum Approach for Engineering. Chichester: Wiley; 2000.
142. Saad Y, Schultz M. GMRES: A generalized minimal residual algorithm for solving nonsymmetric linear systems. SIAM Journal of Scientific and Statistical Computing. 1986; 7:856–869.
143. Hestenes MR, Stiefel E. Methods of conjugate gradients for solving linear systems. Journal of Research of the National Bureau of Standards. 1952; 49(6):409–436.
144. van Brummelen EH. Added mass effects of compressible and incompressible flows in fluid–structure interaction. Journal of Applied Mechanics. 2009; 76:021206.
145. Gil AJ, Arranz Carreño A, Bonet J, Hassan O. An enhanced immersed structural potential method for fluid–structure interaction. Journal of Computational Physics. 2013; 250:178–205.
146. Tezduyar T, Aliabadi S, Behr M, Johnson A, Mittal S. Parallel finite-element computation of 3D flows. Computer. 1993; 26(10):27–36.
147. Johnson AA, Tezduyar TE. Mesh update strategies in parallel finite element computations of flow problems with moving boundaries and interfaces. Computer Methods in Applied Mechanics and Engineering. 1994; 119:73–94.

NIH-PA Author Manuscript

NIH-PA Author Manuscript

NIH-PA Author Manuscript

148. Stein K, Tezduyar T, Benney R. Mesh moving techniques for fluid–structure interactions with large displacements. Journal of Applied Mechanics. 2003; 70:58–63.

149. Stein K, Tezduyar TE, Benney R. Automatic mesh update with the solid-extension mesh moving technique. Computer Methods in Applied Mechanics and Engineering. 2004; 193:2019–2032.

150. Aggarwal A, Ferrari G, Joyce E, Daniels MJ, Sainger R, Gorman JH III, Gorman R, Sacks MS. Architectural trends in the human normal and bicuspid aortic valve leaflet and its relevance to valve disease. Annals of Biomedical Engineering. 2014; 42(5)

151. Dimitri R, De Lorenzis L, Scott MA, Wriggers P, Taylor RL, Zavarise G. Isogeo-metric large deformation frictionless contact using T-splines. Computer Methods in Applied Mechanics and Engineering. 2014; 269:394–414.

152. Sauer RA, De Lorenzis L. A computational contact formulation based on surface potentials. Computer Methods in Applied Mechanics and Engineering. 2013; 253(0):369–395.

153. Kenner T. The measurement of blood density and its meaning. Basic Research in Cardiology. 1989; 84(2):111–124. [PubMed: 2658951]

154. Rosencranz R, Bogen SA. Clinical laboratory measurement of serum, plasma, and blood viscosity. Am. J. Clin. Pathol. 2006; 125(Suppl):78–86.

155. Bellhouse BJ, Bellhouse FH. Mechanism of closure of the aortic valve. Nature. 1968; 217(5123): 86–87. [PubMed: 5635642]

156. Vignon-Clementel IE, Figueroa CA, Jansen KE, Taylor CA. Outflow boundary conditions for three-dimensional finite element modeling of blood flow and pressure in arteries. Computer Methods in Applied Mechanics and Engineering. 2006; 195:3776–3796.

157. Felner, JM. Clinical Methods: The History, Physical, and Laboratory, 3rd edition. Vol. chapter 23. Boston, USA: Butterworths; 1990. The second heart sound.

158. Sabbah HN, Stein PD. Relation of the second sound to diastolic vibration of the closed aortic valve. American Journal of Physiology - Heart and Circulatory Physiology. 1978; 234(6):H696–H700.

159. Sugimoto H, Sacks MS. Effects of leaflet stiffness on in vitro dynamic bioprosthetic heart valve leaflet shape. Cardiovascular Engineering and Technology. 2013; 4(1):2–15. [PubMed: 23646095]

160. Leo HL, Simon H, Carberry J, Lee SC, Yoganathan AP. A comparison of flow field structures of two tri-leaflet polymeric heart valves. Annals of Biomedical Engineering. 2005; 33(4):429–443. [PubMed: 15909649]

161. Leo HL, Dasi LP, Carberry J, Simon HA, Yoganathan AP. Fluid dynamic assessment of three polymeric heart valves using particle image velocimetry. Annals of Biomedical Engineering. 2006; 34(6):936–952. [PubMed: 16783650]

162. Stein PD, Sabbah HN, Lakier JB, Goldstein S. Frequency spectrum of the aortic component of the second heart sound in patients with normal valves, aortic stenosis and aortic porcine xenografts: Potential for detection of porcine xenograft degeneration. The American Journal of Cardiology. 1980; 46(1):48–52. [PubMed: 7386393]

163. Westerhof N, Lankhaar J-W, Westerhof BE. The arterial Windkessel. Medical & Biological Engineering & Computing. 2009; 47:131–141. [PubMed: 18543011]

164. Stein PD, Sabbah HN. Turbulent blood flow in the ascending aorta of humans with normal and diseased aortic valves. Circ. Res. 1976; 39(1):58–65. [PubMed: 776437]

165. Evans JA, Hughes TJR. Isogeometric divergence-conforming B-splines for the unsteady Navier-Stokes equations. Journal of Computational Physics. 2013; 241:141–167.

166. Hsu M-C, Kamensky D, Bazilevs Y, Sacks MS, Hughes TJR. Fluid–structure interaction analysis of bioprosthetic heart valves: significance of arterial wall deformation. Computational Mechanics. 2014; 54(4):1055–1071.

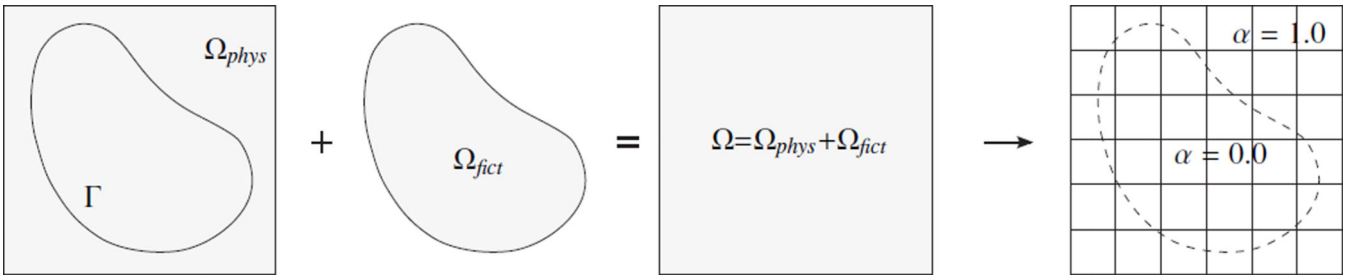

Figure 1.

The physical domain of interest Ω_{phys} is extended by the fictitious domain Ω_{fict} into an embedding domain Ω to allow easy meshing of complex geometries. The influence of Ω_{fict} is penalized by α.

NIH-PA Author Manuscript NIH-PA Author Manuscript NIH-PA Author Manuscript

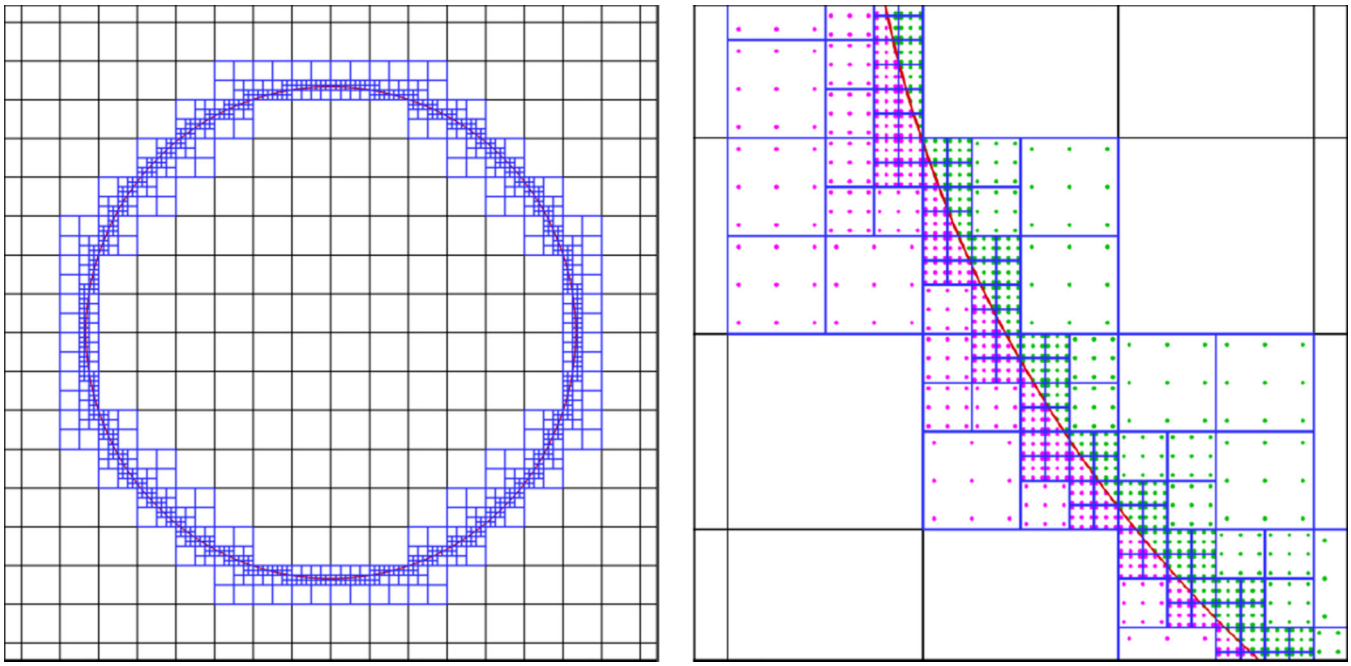

Figure 2.

The sub-cells (blue lines) used to generate an adaptive quadrature rule for a circular boundary, with $l = 3$ levels of recursion. The adaptive quadrature points outside the cylinder (marked in pink) belong to the physical domain of interest and are used in the numerical integration. The quadrature points inside the cylinder (marked in green) belong to the fictitious domain extension and are discarded.

NIH-PA Author Manuscript NIH-PA Author Manuscript NIH-PA Author Manuscript

NIH-PA Author Manuscript
NIH-PA Author Manuscript
NIH-PA Author Manuscript

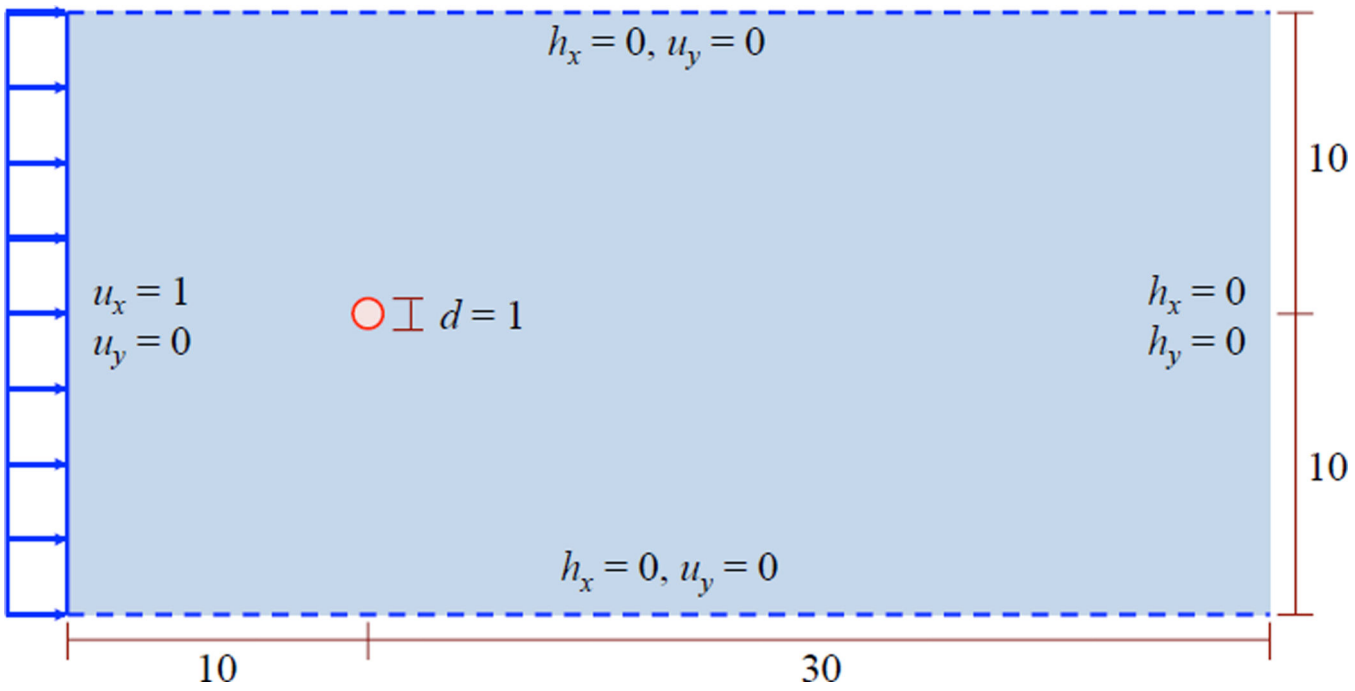

Figure 3.
The domain and boundary conditions for the benchmark problem of 2D flow past a circular cylinder.

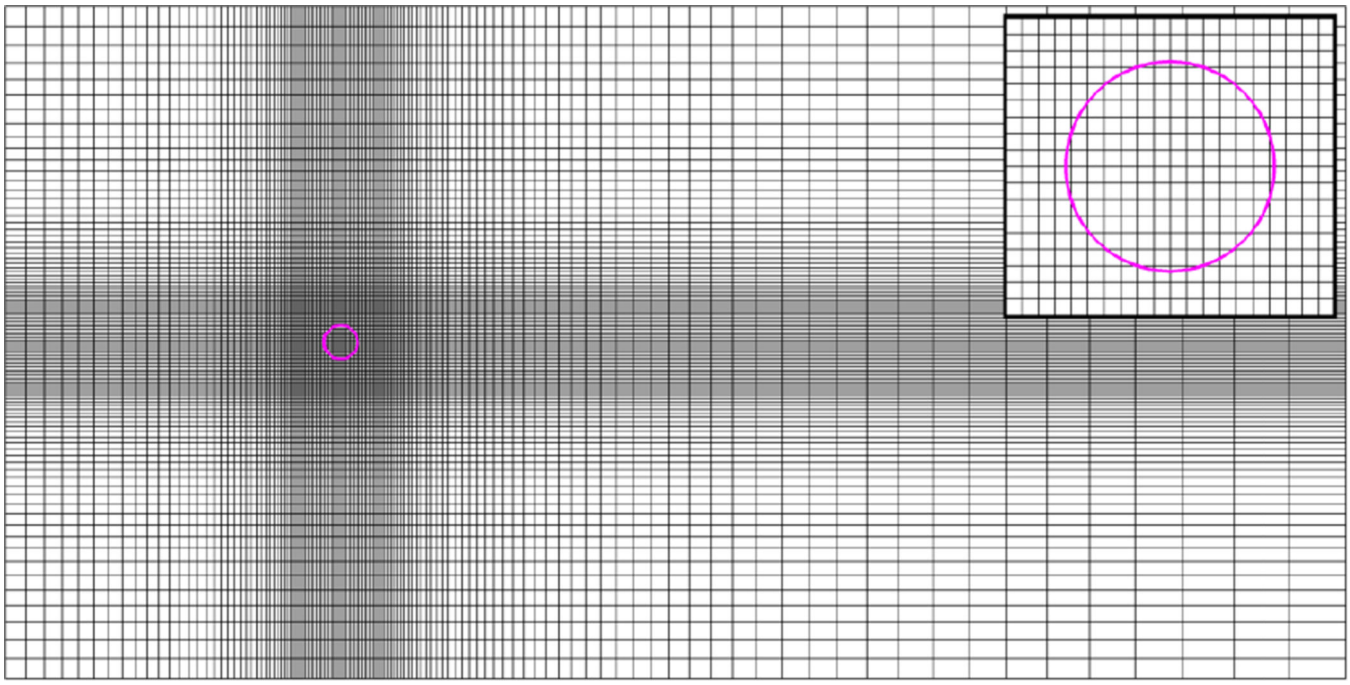

Figure 4.
The non-boundary-fitted, immersogeometric discretization M1.

NIH-PA Author Manuscript
NIH-PA Author Manuscript
NIH-PA Author Manuscript

NIH-PA Author Manuscript
NIH-PA Author Manuscript
NIH-PA Author Manuscript

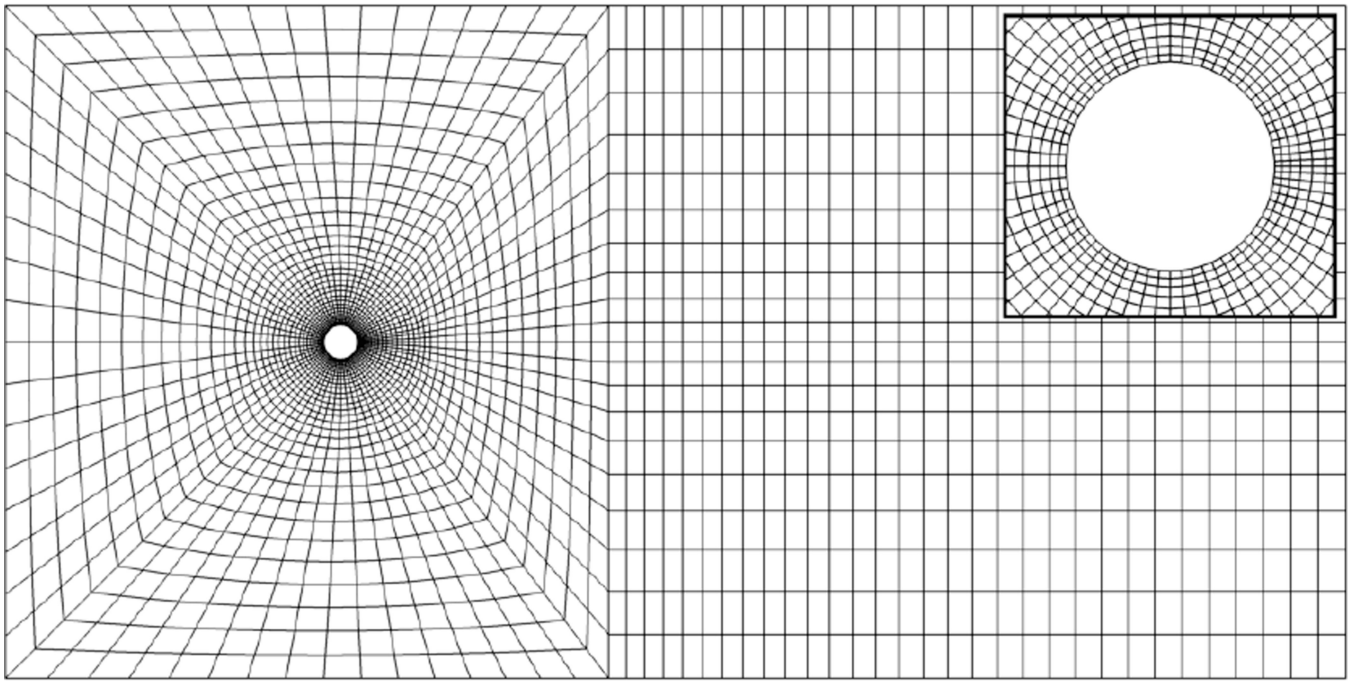

Figure 5.
Boundary-fitted mesh BM1. The reference solutions are computed on BM2, which is a uniform refinement of this mesh.

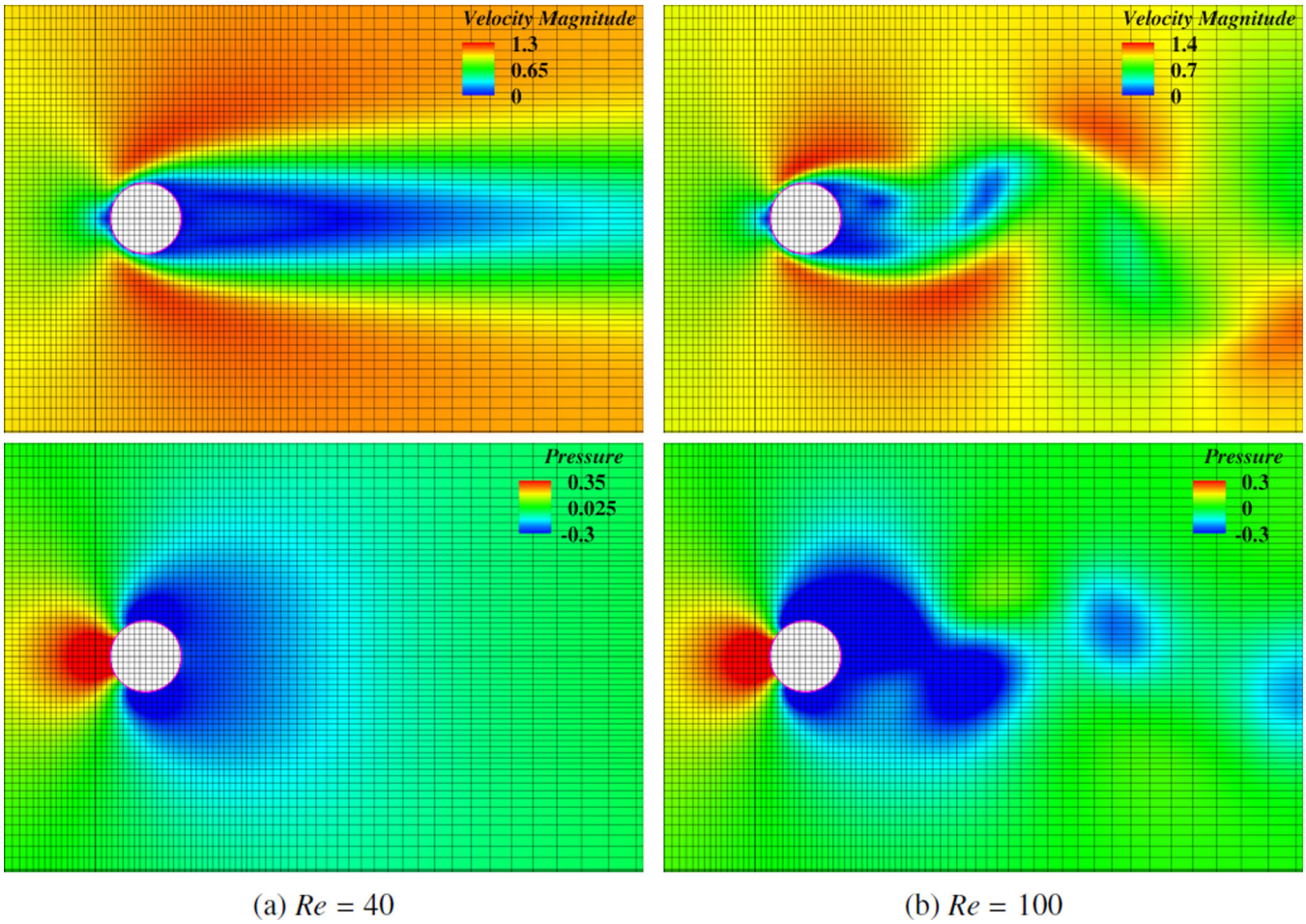

Figure 6.

Visualizations of velocity and pressure fields about a cylinder immersed in M1, showing both steady ($Re = 40$) and time-periodic ($Re = 100$) solutions. Results are obtained using $\tau^B = 10^2$ and $l = 3$.

NIH-PA Author Manuscript
NIH-PA Author Manuscript
NIH-PA Author Manuscript

NIH-PA Author Manuscript

NIH-PA Author Manuscript

NIH-PA Author Manuscript

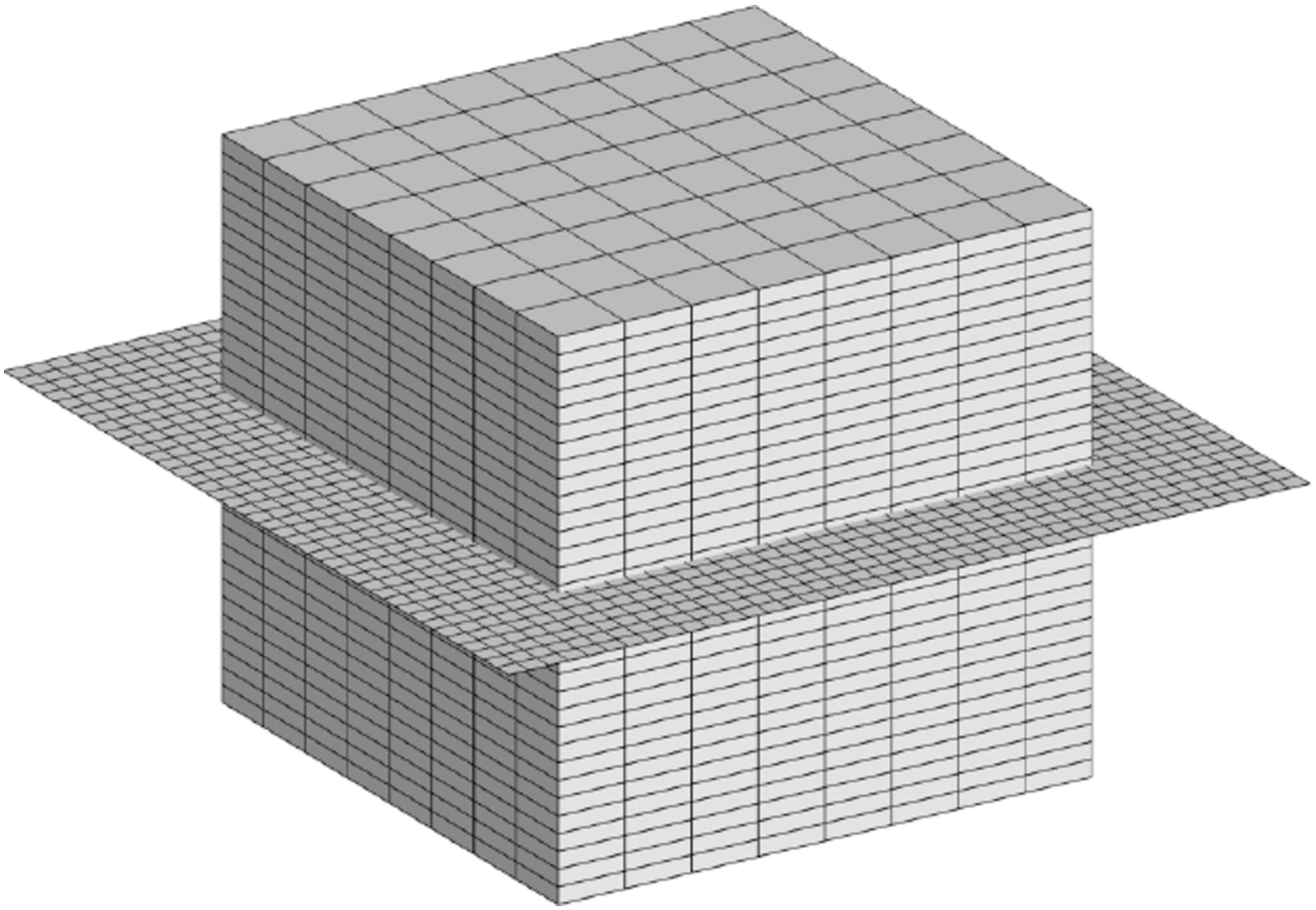

Figure 7.
The computational mesh used for the closed-valve model problem.

NIH-PA Author Manuscript
NIH-PA Author Manuscript
NIH-PA Author Manuscript

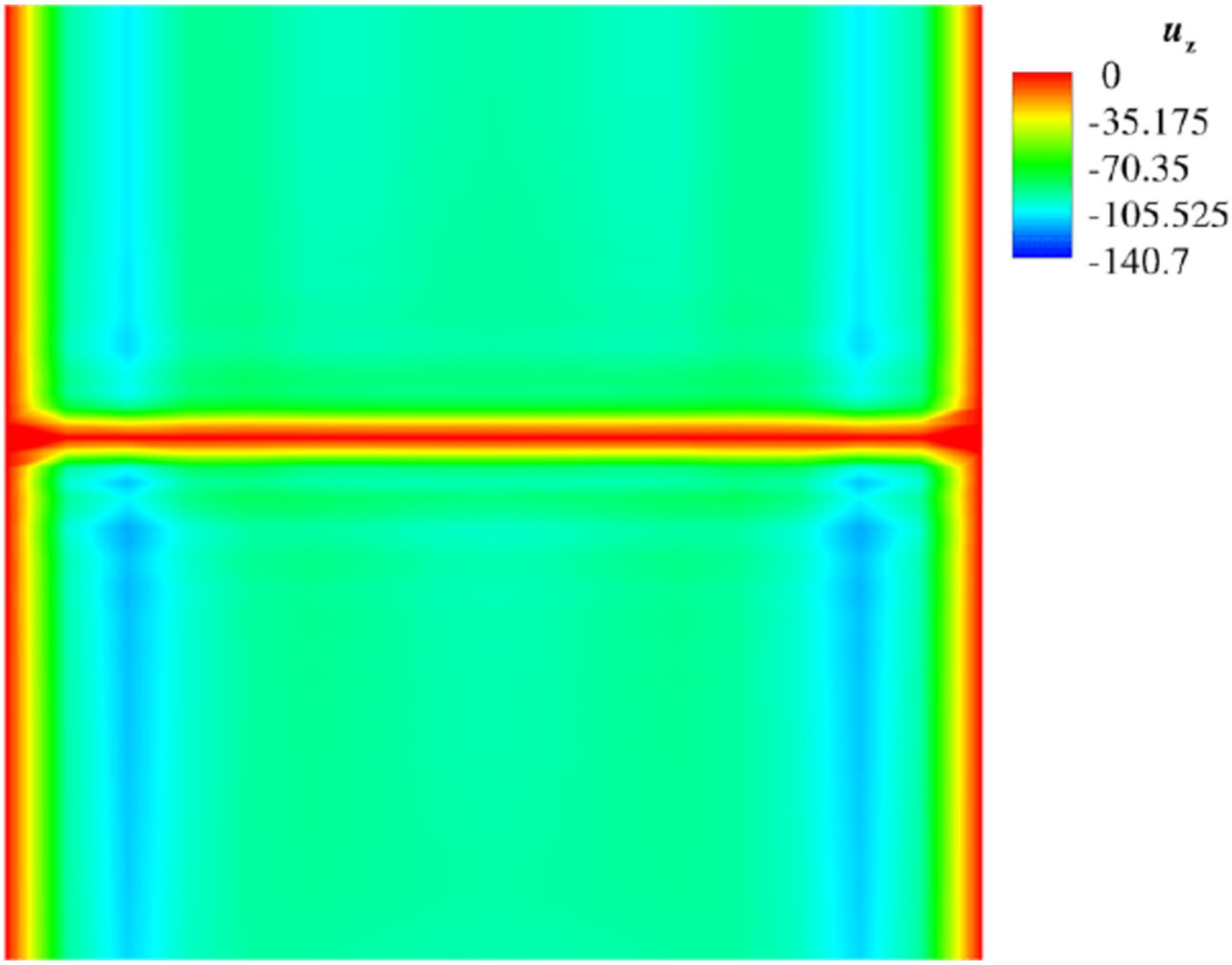

Figure 8.

The *z*-component of velocity, in cm/s, for a highly unphysical steady-state flow solution through a blocked channel, as computed with $\Delta t = 10^{-4}$ s and no modifications to fluid stabilization terms. The fluid spuriously compresses to meet the velocity constraint imposed by the barrier while maintaining a large downward flow through the channel.

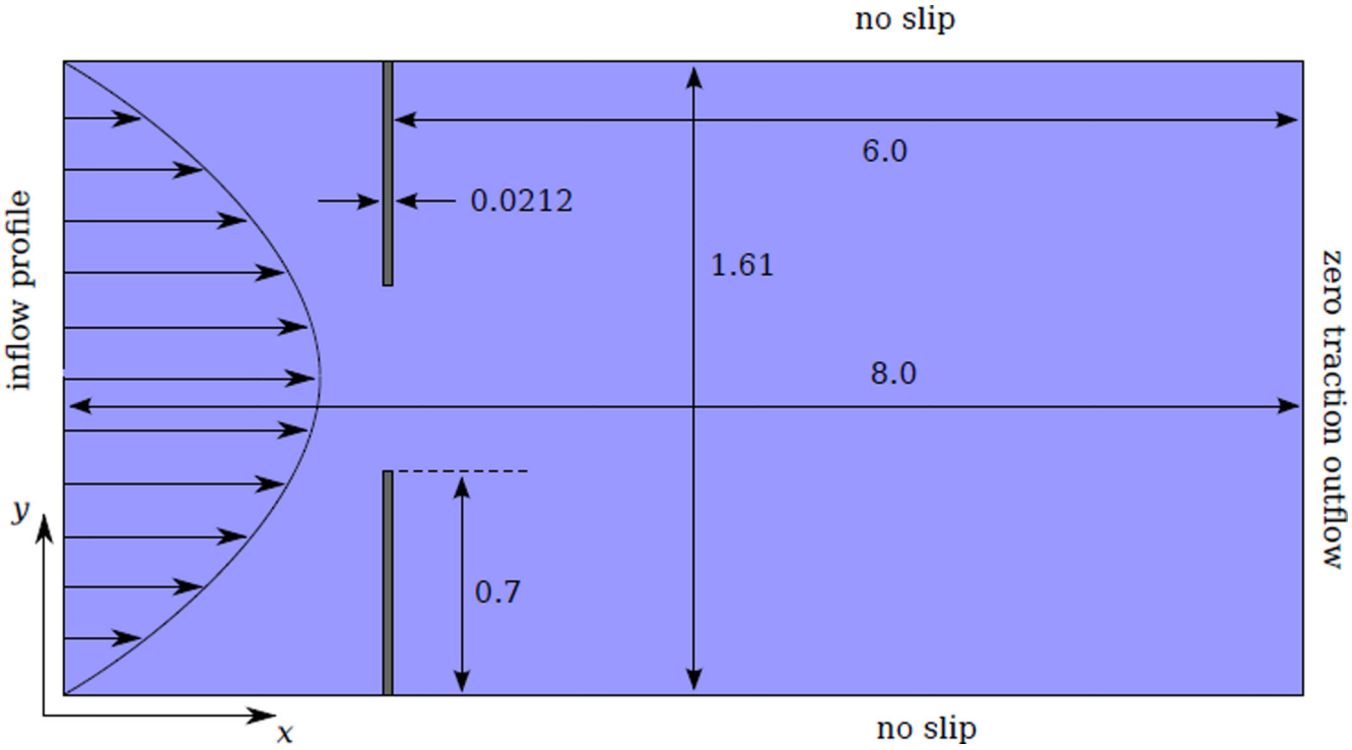

Figure 9.
Geometry and boundary conditions of the 2D heart valve benchmark. Not to scale. The inflow profile is given by Eq. (55).

NIH-PA Author Manuscript
NIH-PA Author Manuscript
NIH-PA Author Manuscript

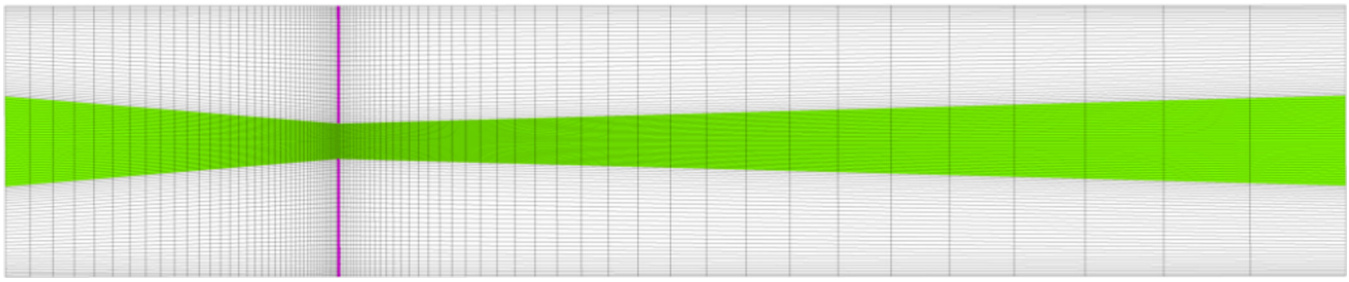

Figure 10.
The reference configuration of the boundary-fitted mesh for the 2D valve problem, with leaflets highlighted in magenta and areas of softened mesh highlighted in green.

NIH-PA Author Manuscript
NIH-PA Author Manuscript
NIH-PA Author Manuscript

NIH-PA Author Manuscript
NIH-PA Author Manuscript
NIH-PA Author Manuscript

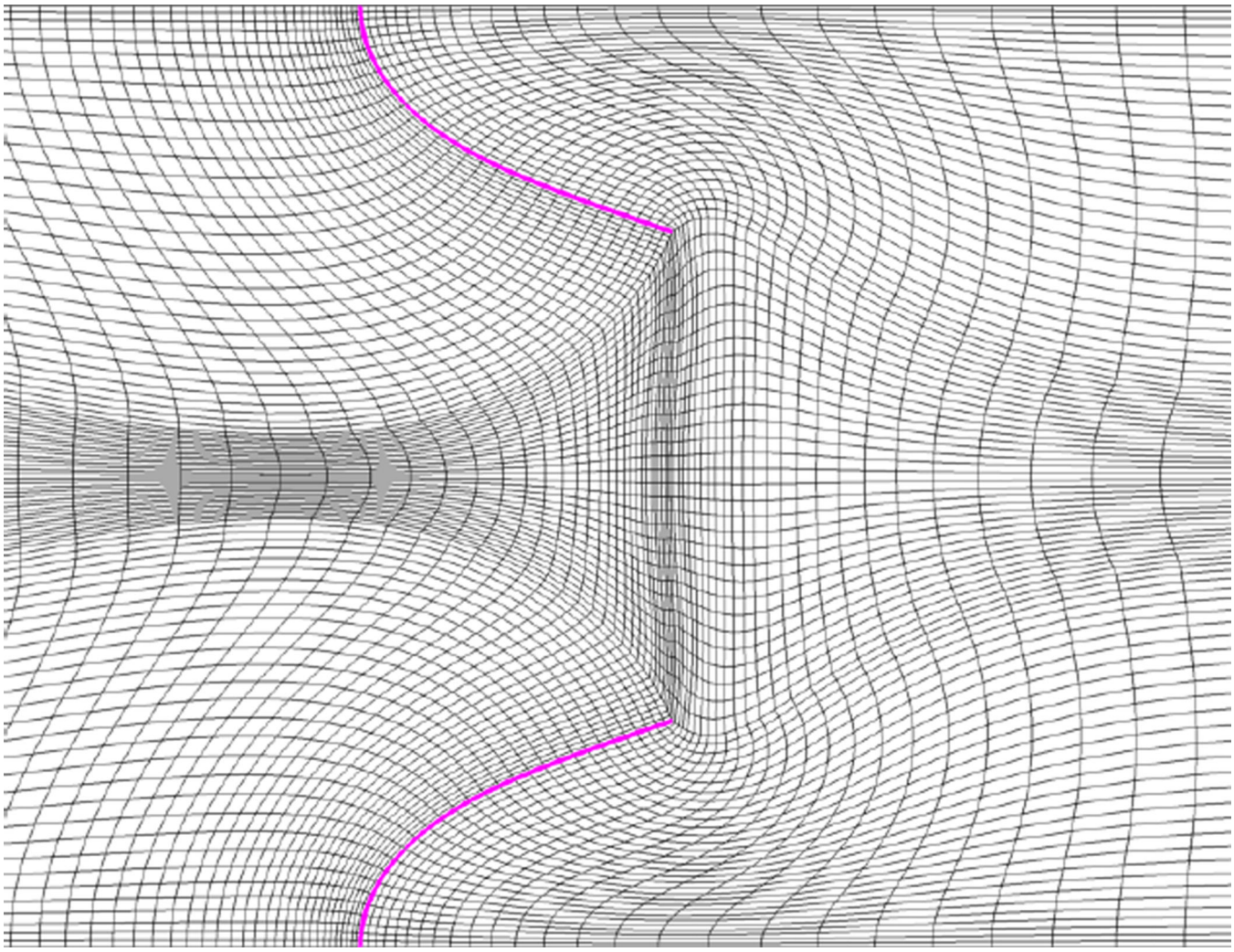

Figure 11.
The deformation of the boundary-fitted fluid mesh at $t = 0.5$.

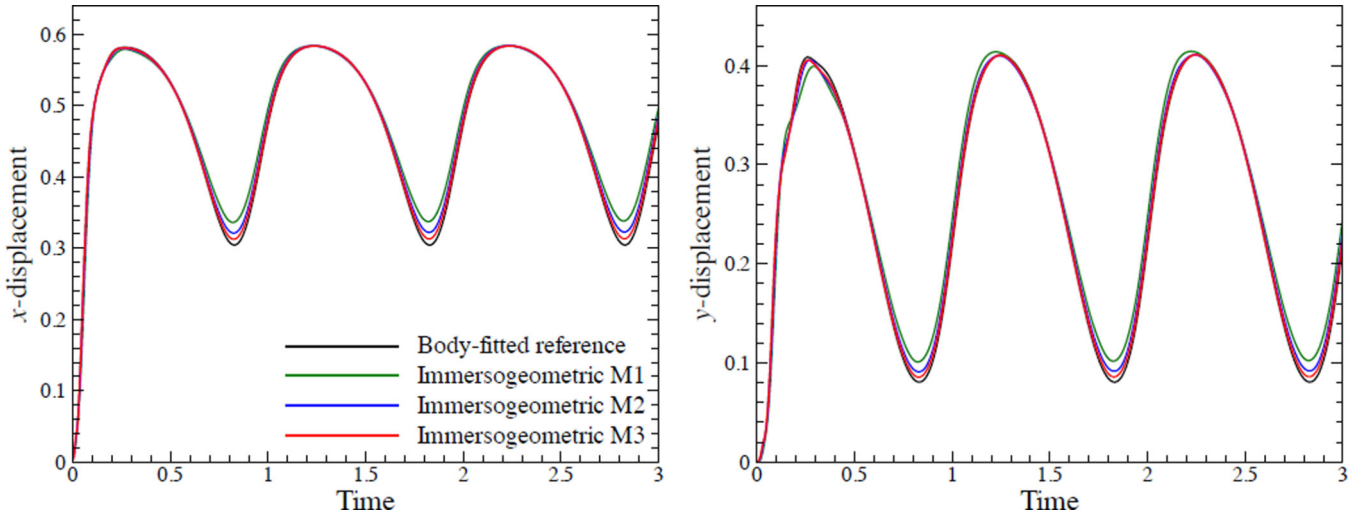

Figure 12.

The *x*- and *y*-displacements of the upper leaflet tip, computed on the immersed and boundary-fitted meshes.

NIH-PA Author Manuscript
NIH-PA Author Manuscript
NIH-PA Author Manuscript

NIH-PA Author Manuscript

NIH-PA Author Manuscript

NIH-PA Author Manuscript

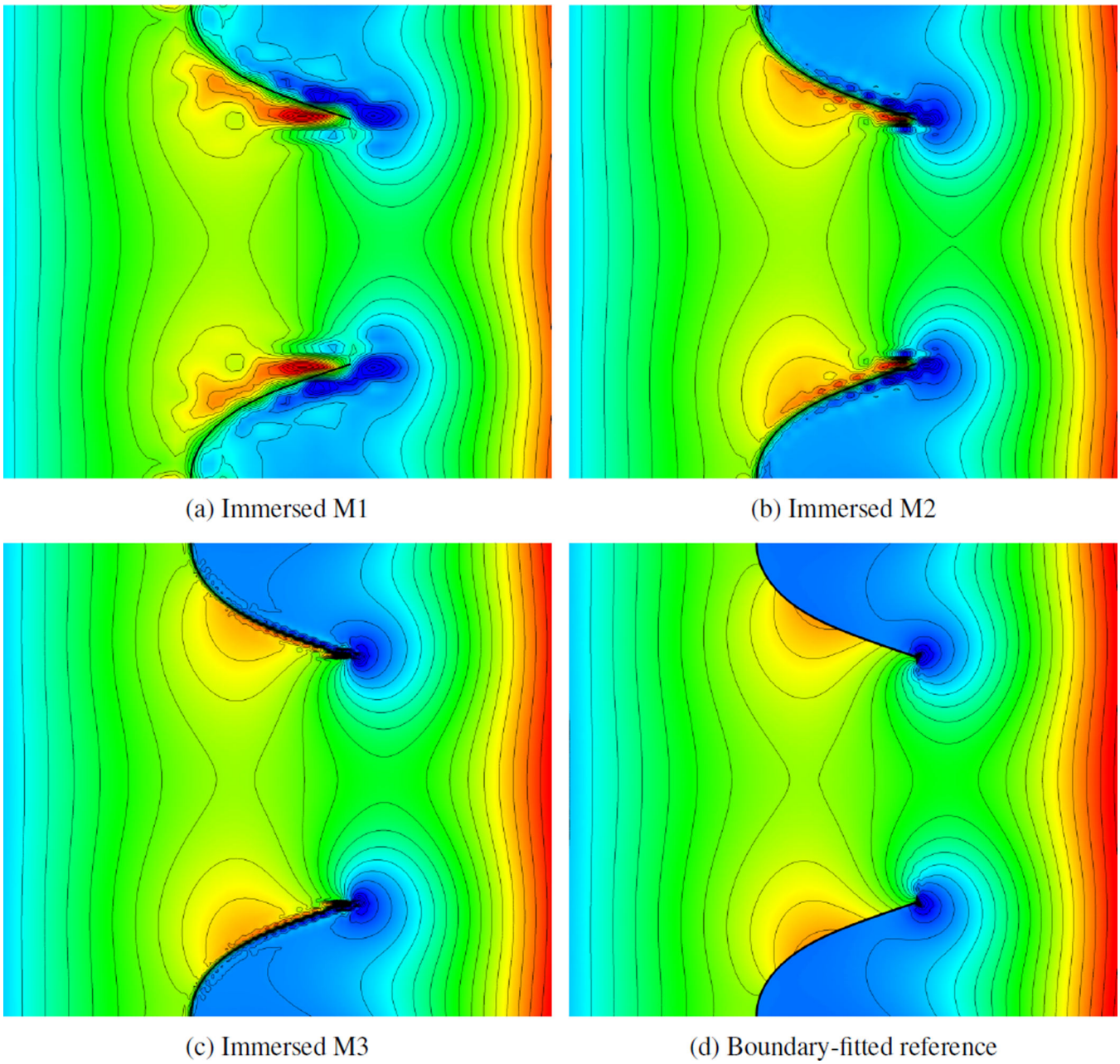

Figure 13.

Pressure contours at $t = 0.5$, from immersogeometric computations on M1, M2, and M3, along with the boundary-fitted reference. Large pointwise pressure errors are confined to an $\mathcal{O}(h)$ neighborhood of the immersed structure, becoming increasingly localized with spatial refinement.

NIH-PA Author Manuscript
NIH-PA Author Manuscript
NIH-PA Author Manuscript

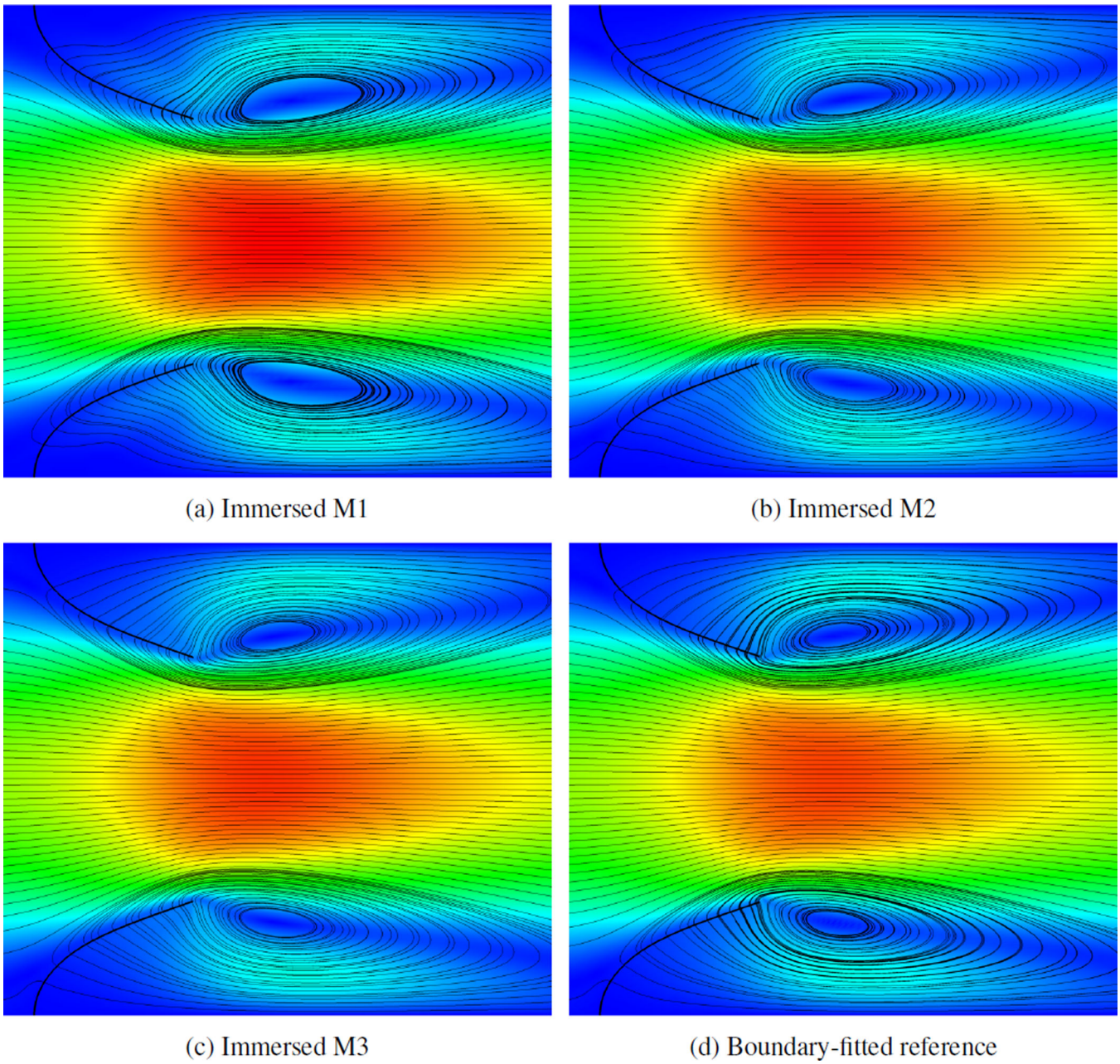

Figure 14.

Velocity streamlines superimposed on a velocity magnitude contour plot, at $t = 0.5$, from immersogeometric computations on M1, M2, and M3, and the boundary-fitted reference.

NIH-PA Author Manuscript

NIH-PA Author Manuscript

NIH-PA Author Manuscript

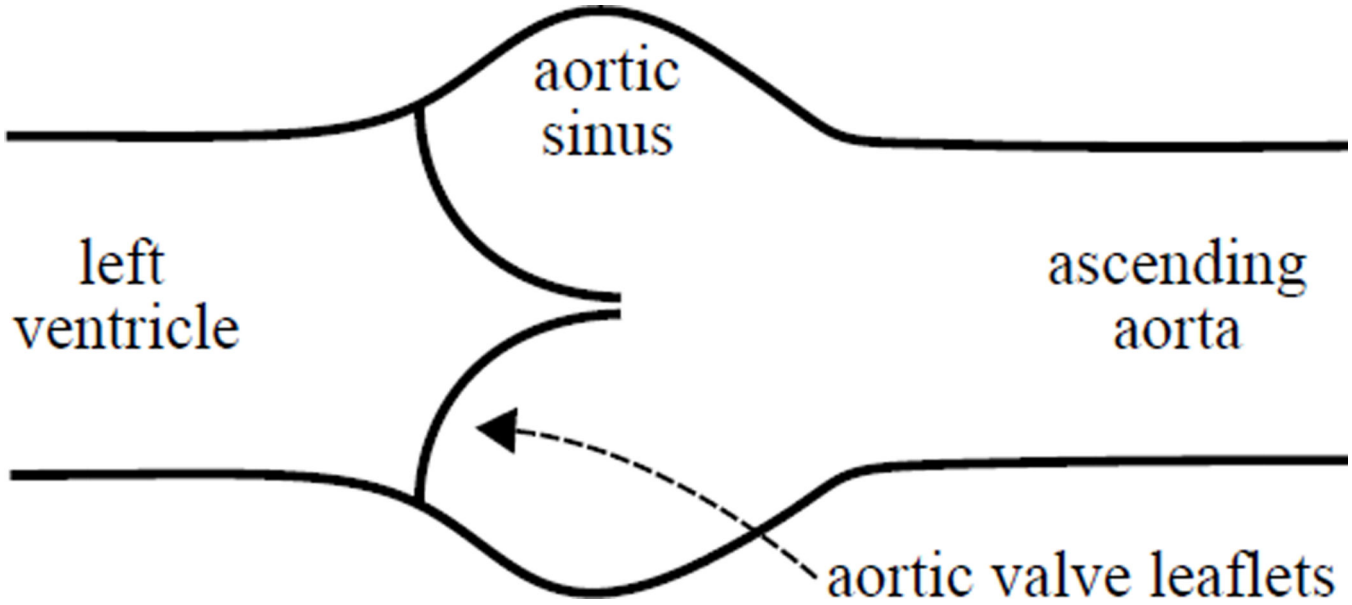

Figure 15.
A schematic drawing illustrating the position of the aortic valve relative to the left ventricle of the heart and the ascending aorta.

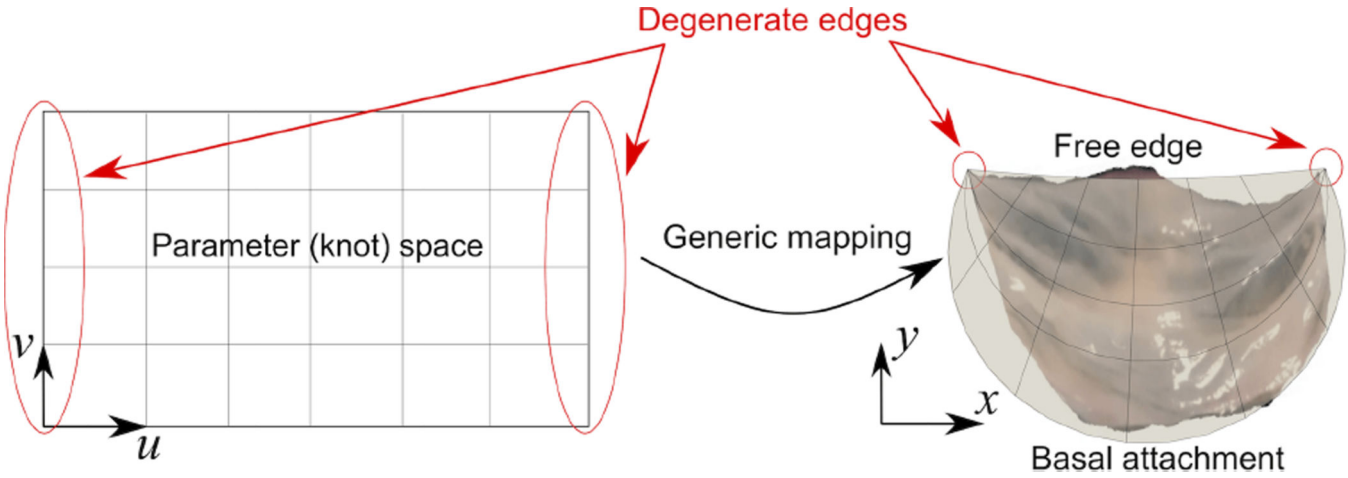

Figure 16.
Generic mapping for an aortic valve leaflet using a B-spline patch, where two edges in the parametric space are degenerated to commissure points.

NIH-PA Author Manuscript
NIH-PA Author Manuscript
NIH-PA Author Manuscript

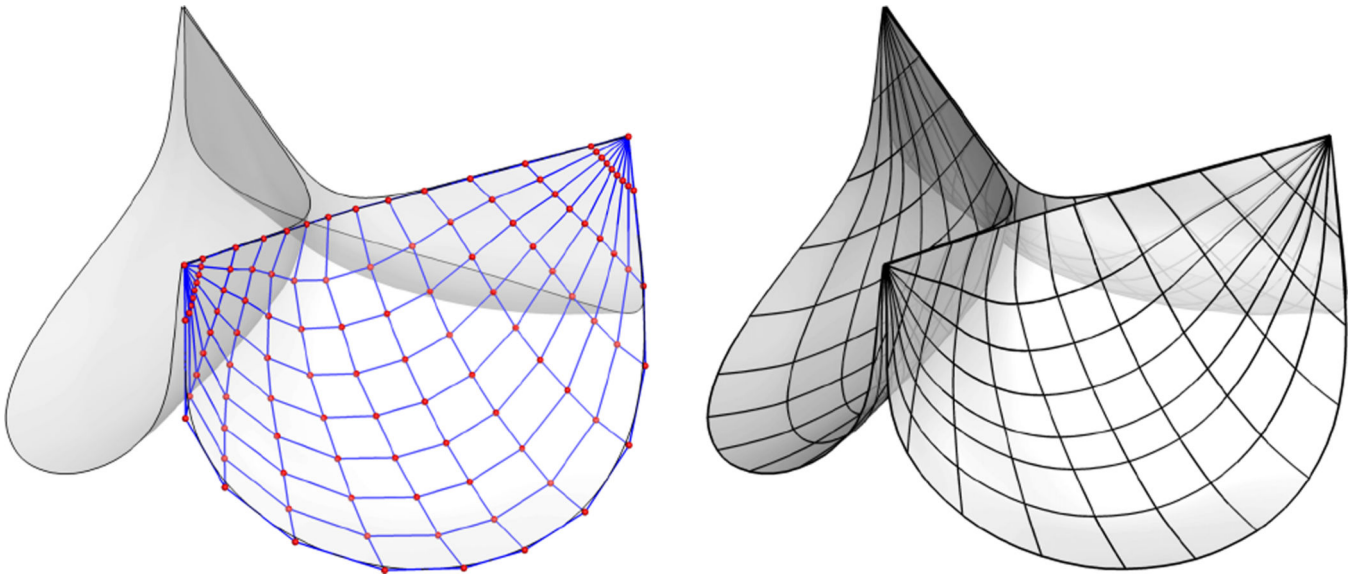

Figure 17.
Left: Control mesh. Right: The physical images of knot spans in the BHV mesh, prior to analysis refinements.

NIH-PA Author Manuscript
NIH-PA Author Manuscript
NIH-PA Author Manuscript

NIH-PA Author Manuscript

NIH-PA Author Manuscript

NIH-PA Author Manuscript

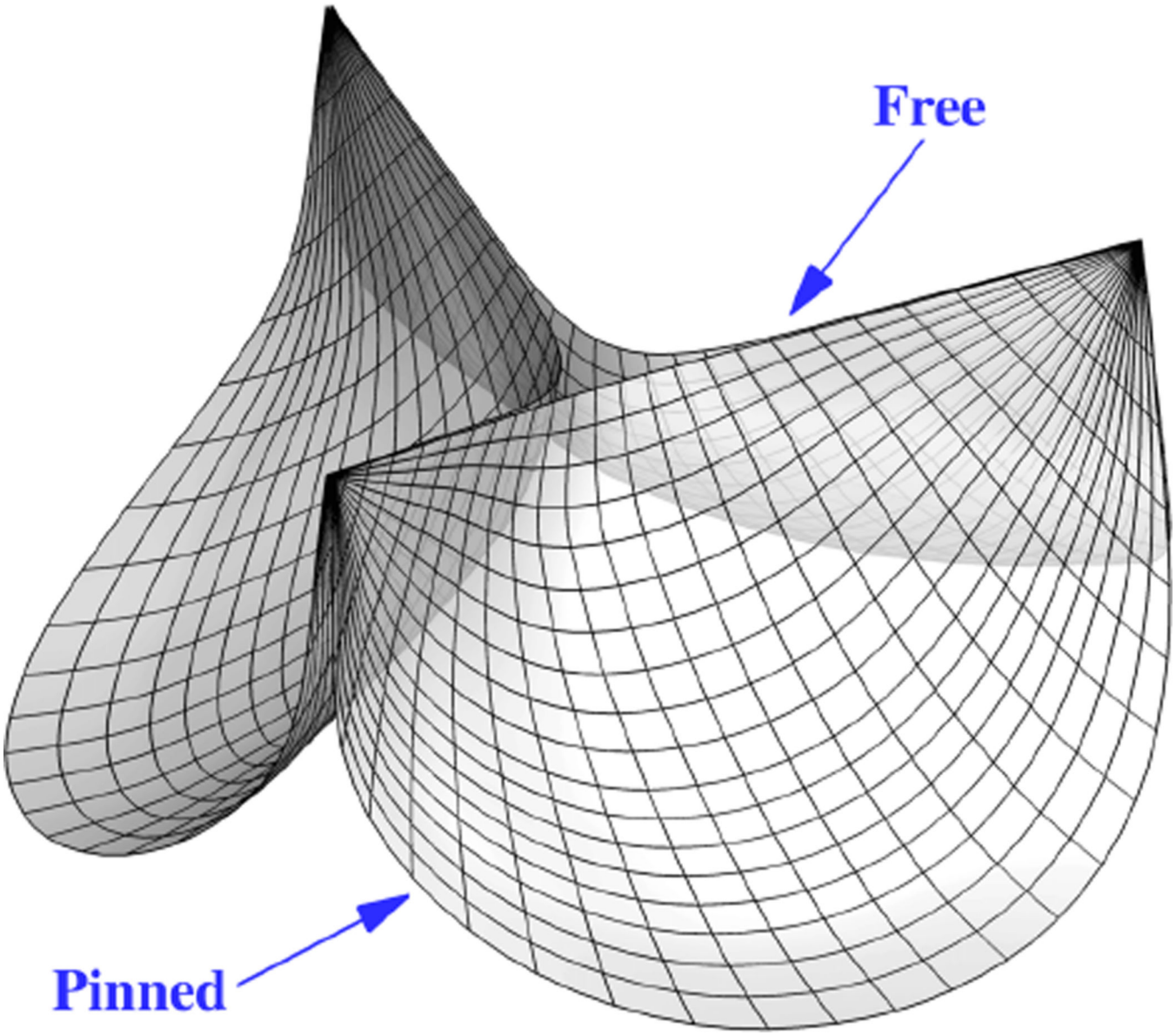

Figure 18.

Refined B-spline mesh for analysis purposes. It is comprised of 1404 quadratic elements. The pinned boundary condition is applied to the leaflet attachment edge.

NIH-PA Author Manuscript

NIH-PA Author Manuscript

NIH-PA Author Manuscript

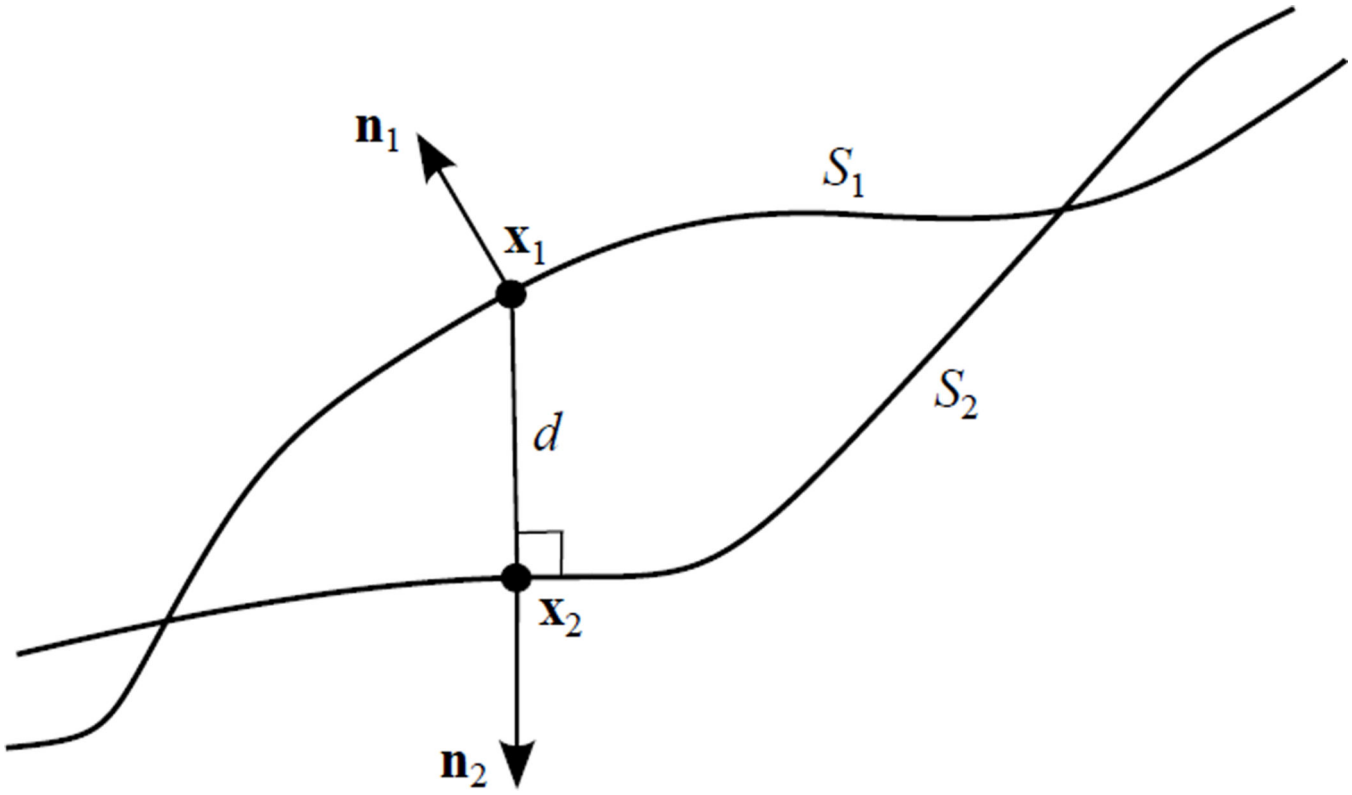

Figure 19.
Illustration of contact notation.

NIH-PA Author Manuscript
NIH-PA Author Manuscript
NIH-PA Author Manuscript

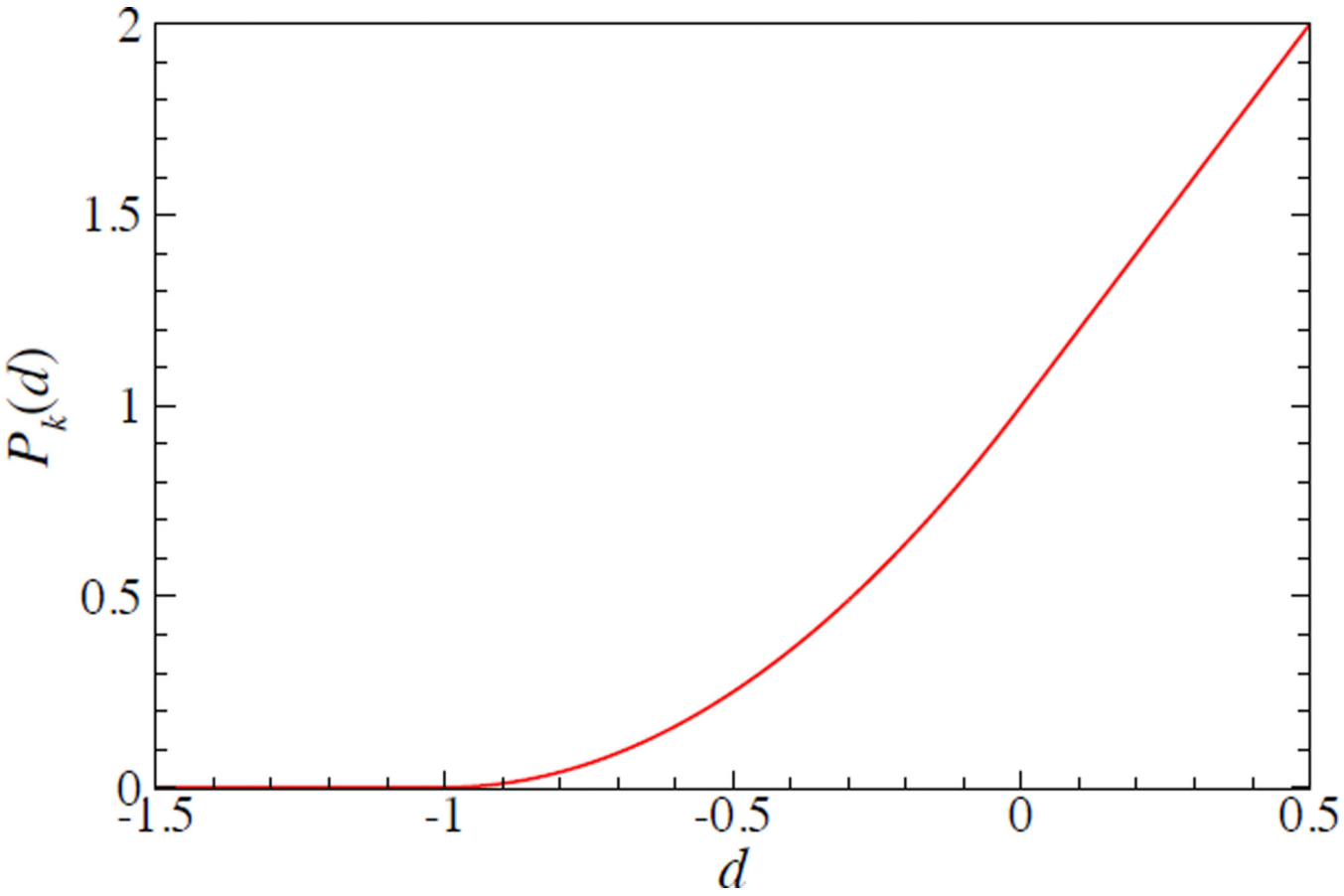

Figure 20.
The function $P_k(d)$ for $k = 2$ and $h = 1$.

NIH-PA Author Manuscript

NIH-PA Author Manuscript

NIH-PA Author Manuscript

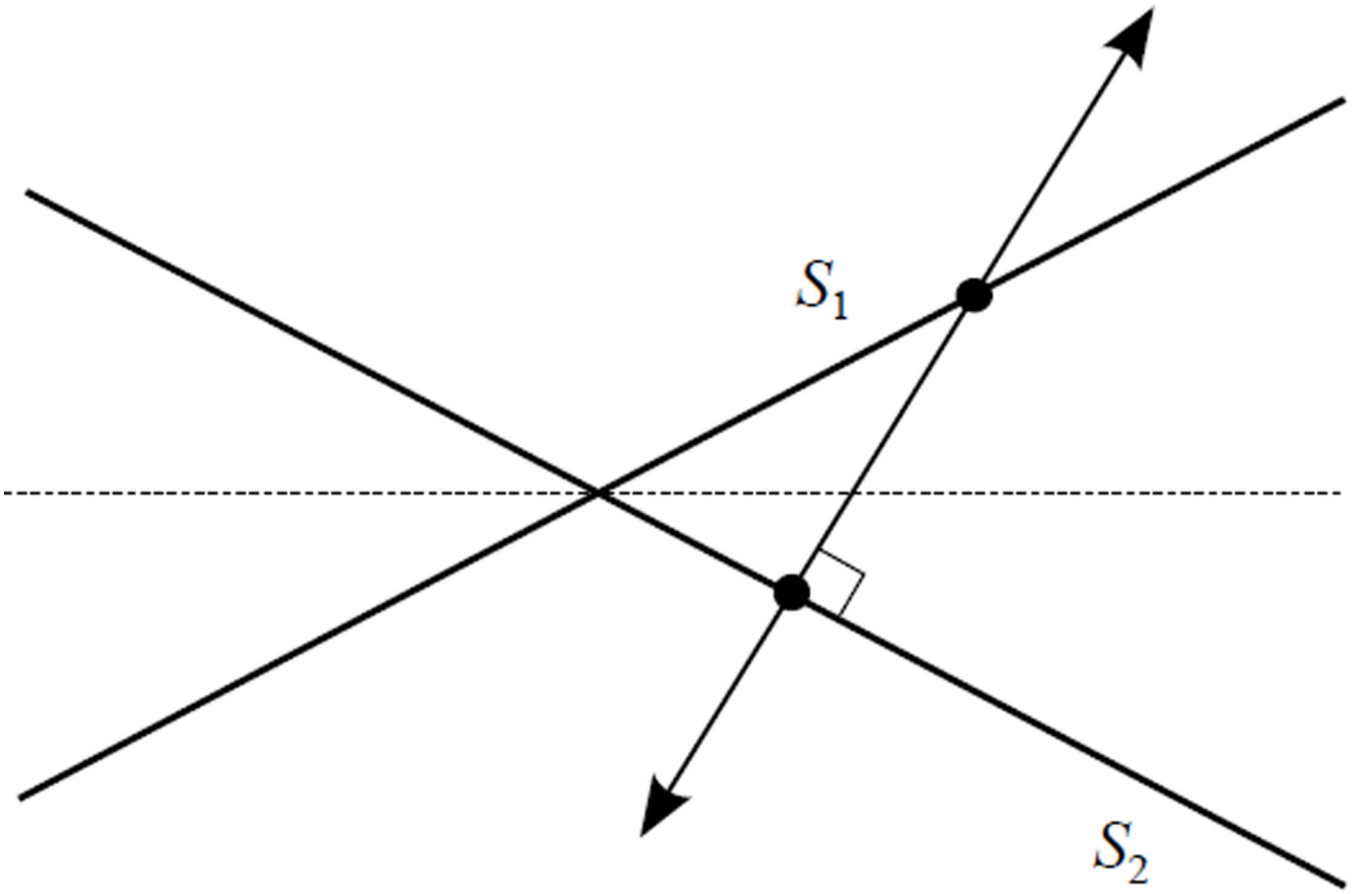

Figure 21.
Symmetrical geometry results in asymmetrical contact forces.

NIH-PA Author Manuscript

NIH-PA Author Manuscript

NIH-PA Author Manuscript

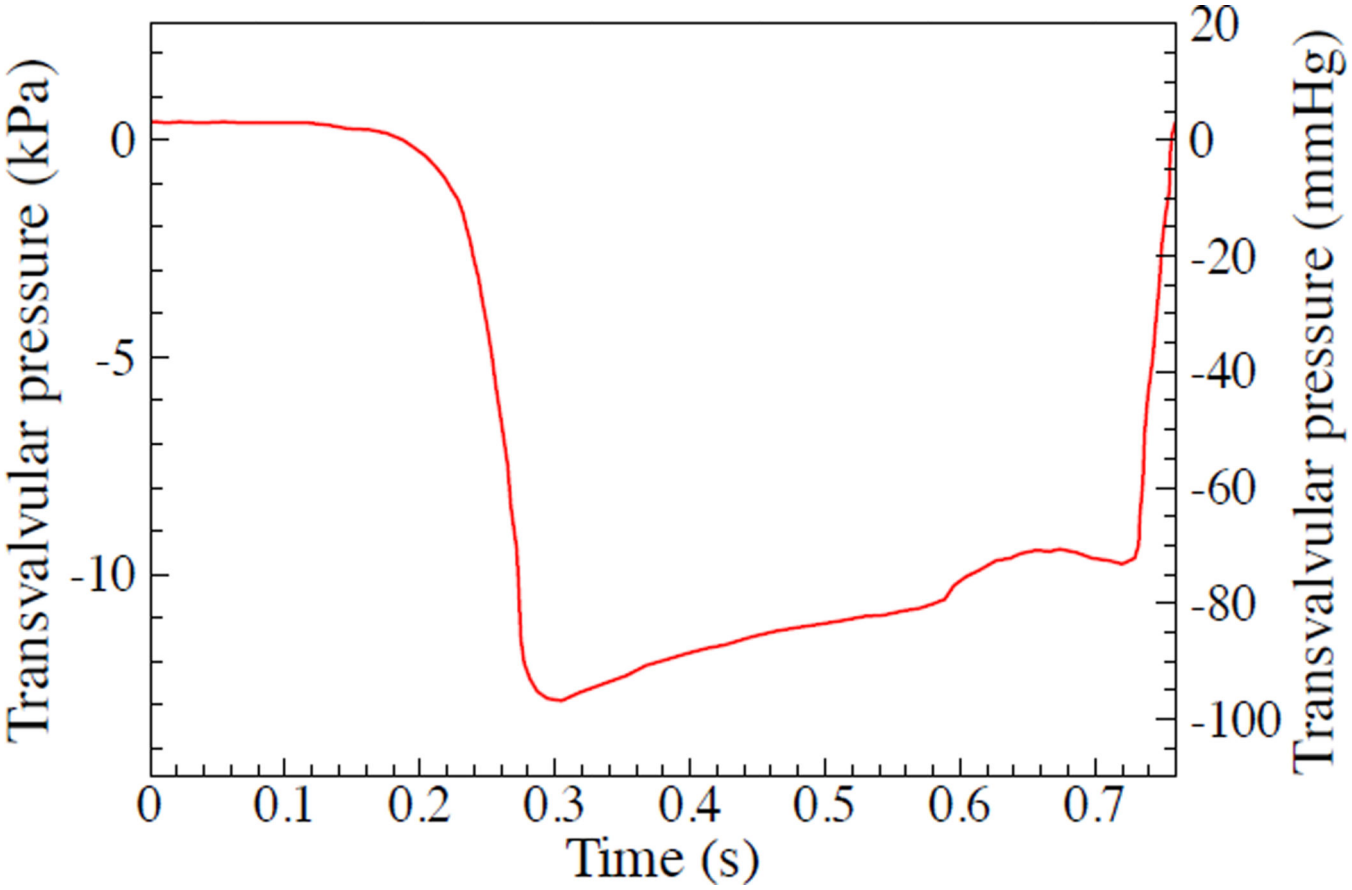

Figure 22.
Transvalvular pressure applied to the leaflets as a function of time. The duration of a single cardiac cycle is 0.76 s.

NIH-PA Author Manuscript
NIH-PA Author Manuscript
NIH-PA Author Manuscript

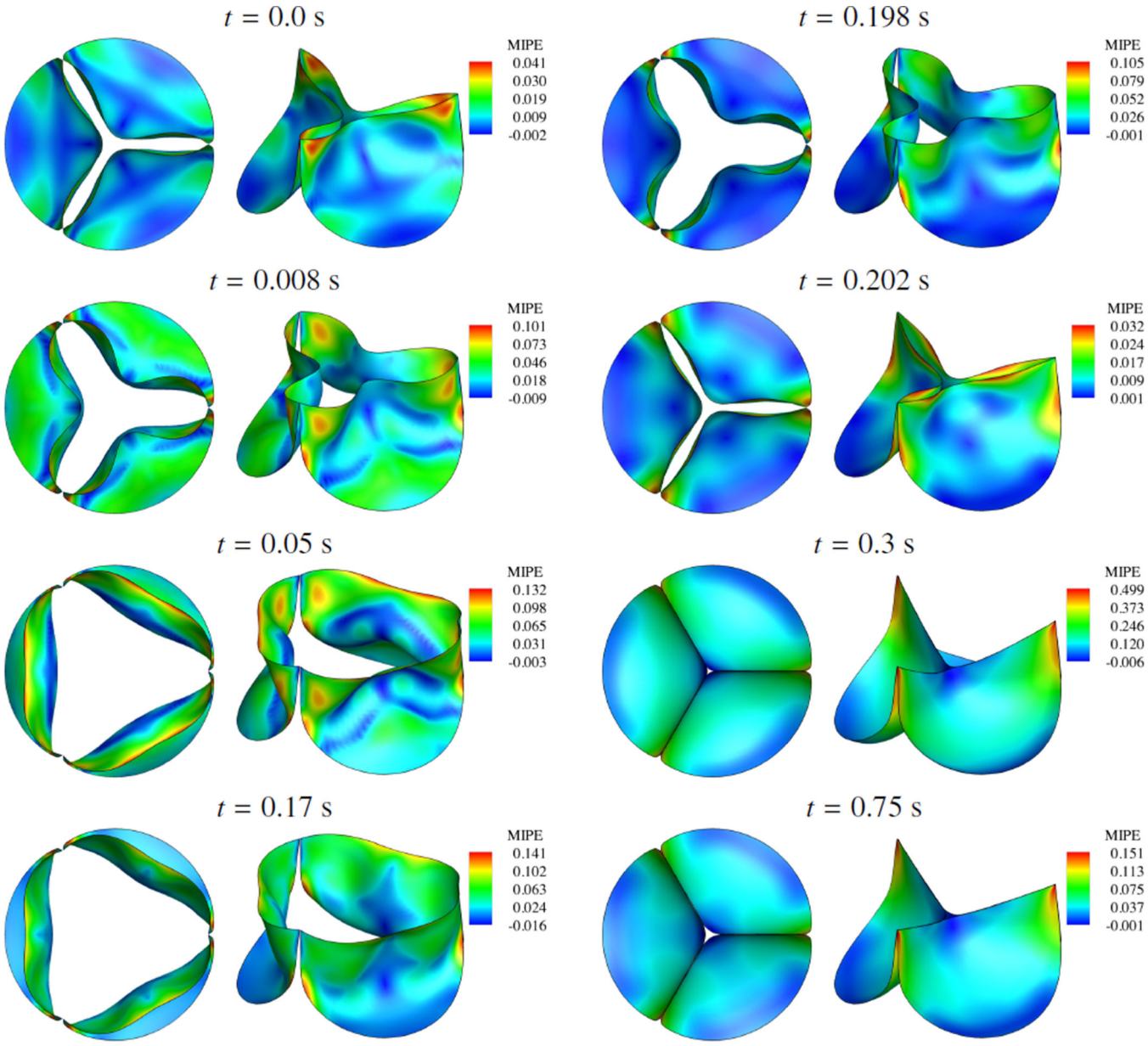

Figure 23.

Deformations of the valve from a cycle of the dynamic computation, colored by maximum in-plane principal Green-Lagrange strain (MIPE, the largest eigenvalue of **E**), evaluated on the aortic side of the leaflet. Note the different scale for each time. Time is synchronized with Figure 22. The initial condition at $t = 0$ s comes from the preceding cycle and is not the stress-free configuration.

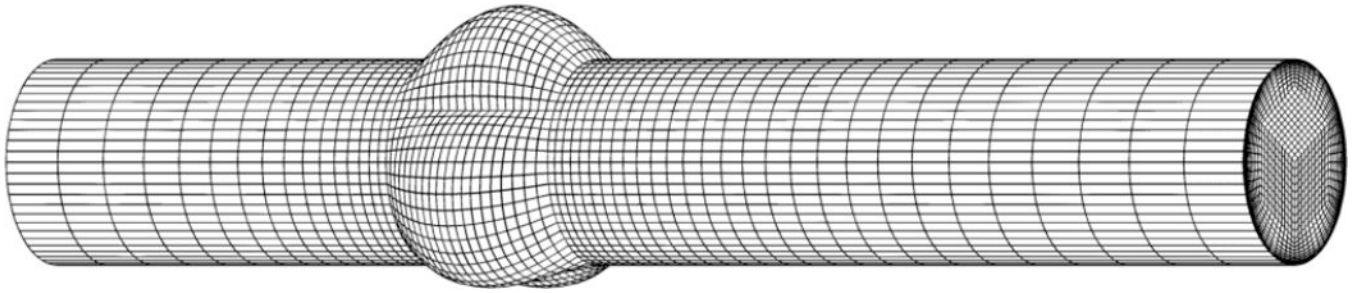

Figure 24.
A view of the fluid domain into which the valve is immersed.

NIH-PA Author Manuscript
NIH-PA Author Manuscript
NIH-PA Author Manuscript

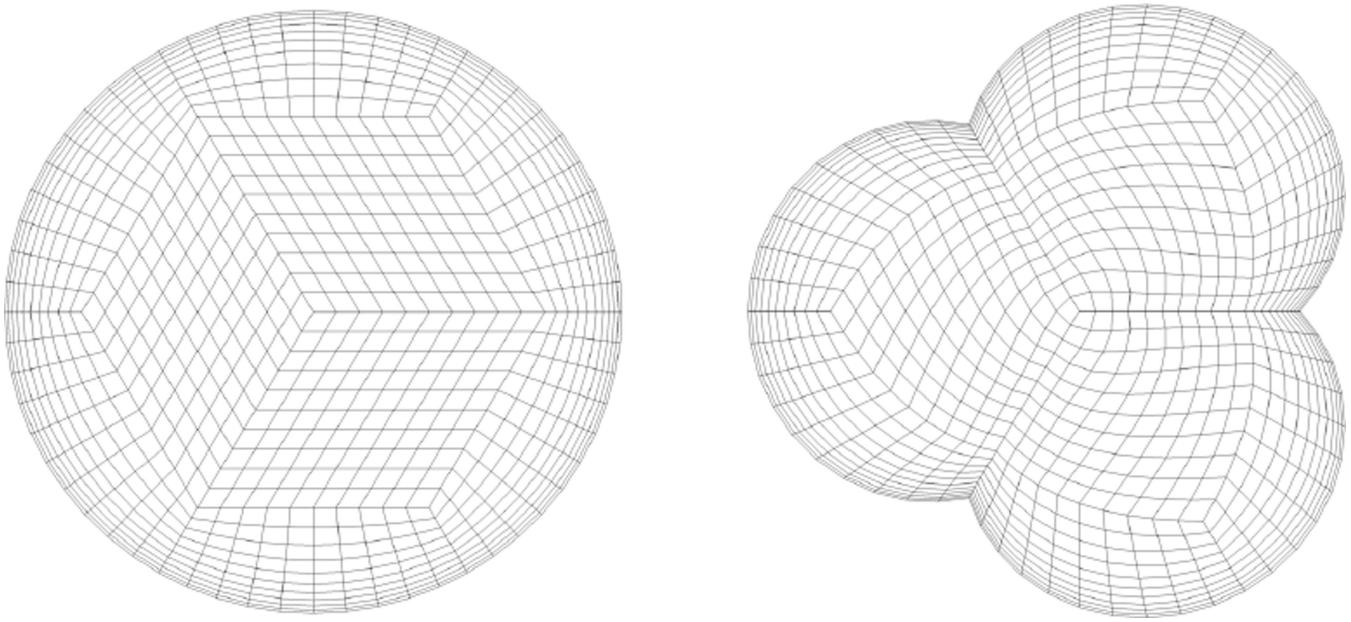

Figure 25.
Cross-sections of the fluid mesh, taken from the cylindrical portion and from the sinus.

NIH-PA Author Manuscript
NIH-PA Author Manuscript
NIH-PA Author Manuscript

NIH-PA Author Manuscript

NIH-PA Author Manuscript

NIH-PA Author Manuscript

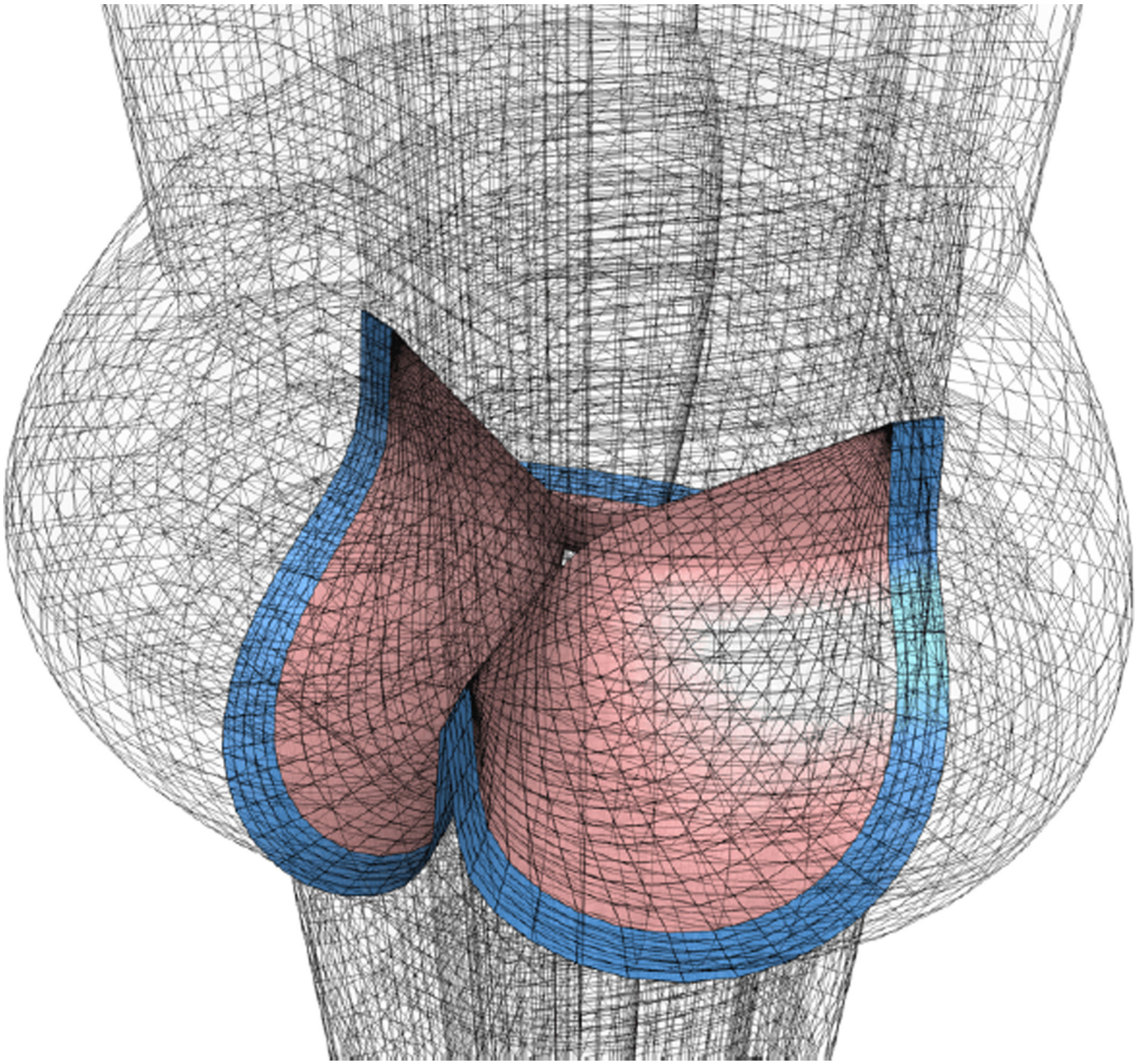

Figure 26.
The sinus, magnified and shown in relation to the valve leaflets (pink) and rigid stent (blue).

NIH-PA Author Manuscript

NIH-PA Author Manuscript

NIH-PA Author Manuscript

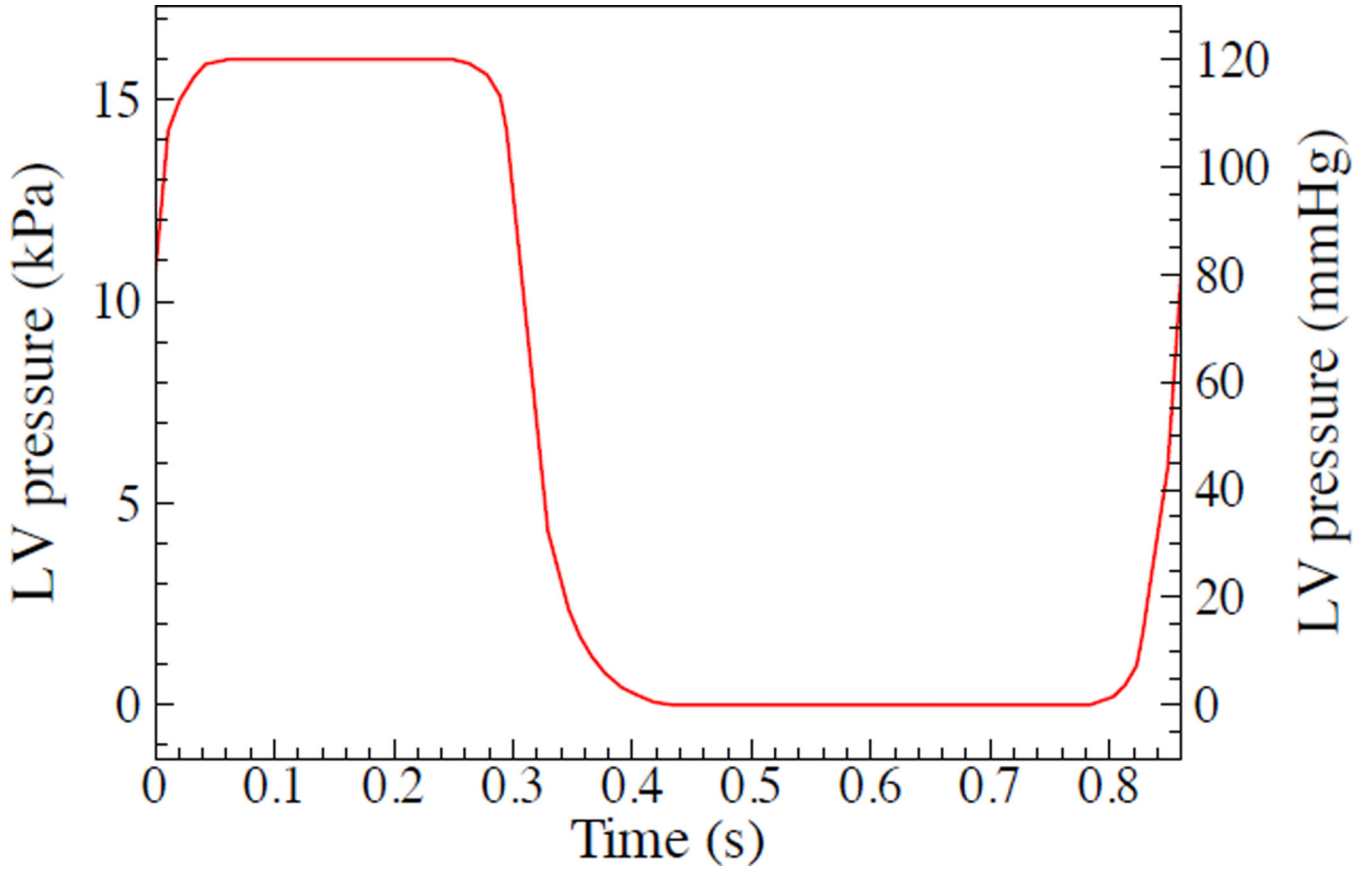

Figure 27.
The idealized left ventricular (LV) pressure profile applied to the nominal inflow of the fluid domain. The duration of a single cardiac cycle is 0.86 s.

NIH-PA Author Manuscript

NIH-PA Author Manuscript

NIH-PA Author Manuscript

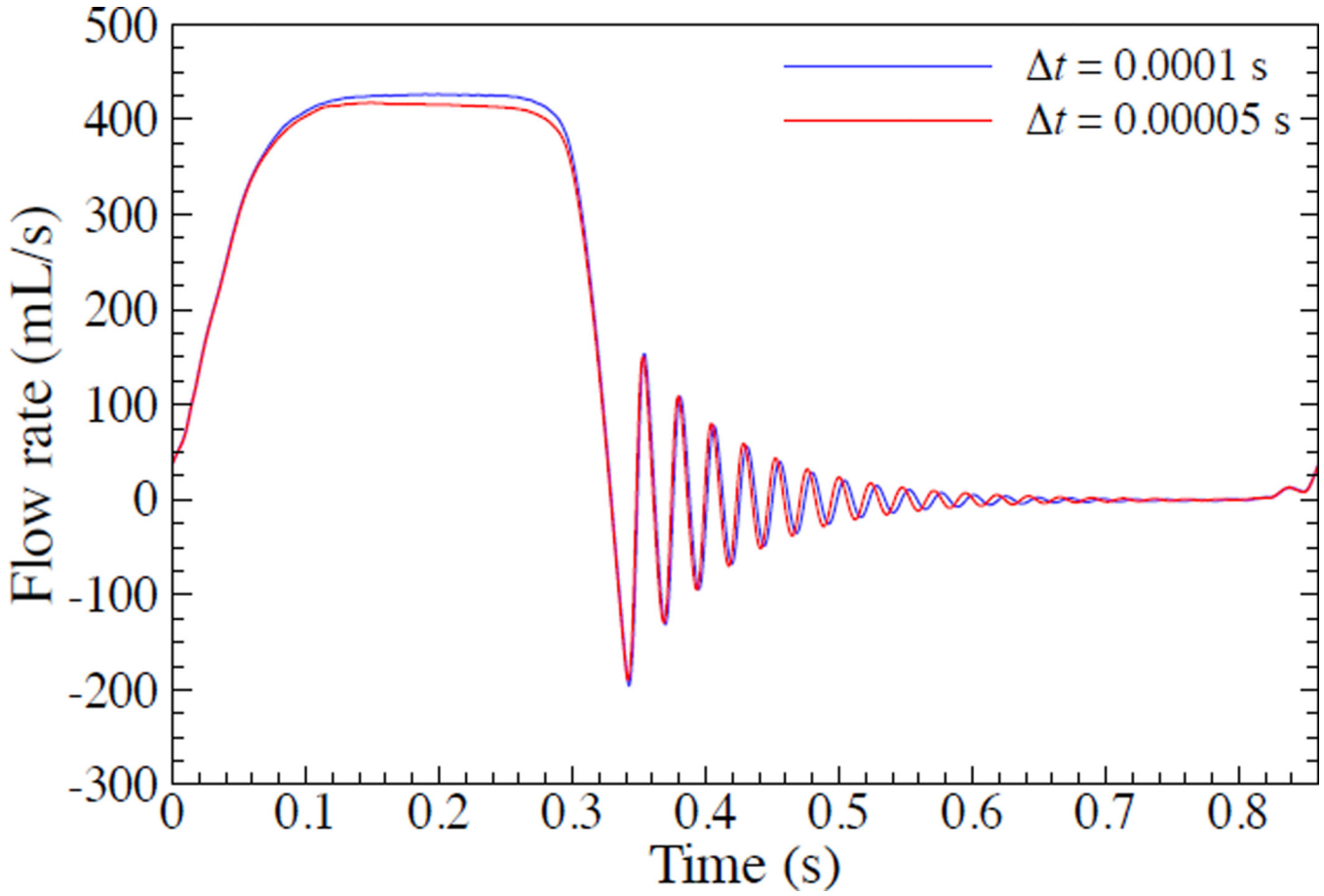

Figure 28.
Computed volumetric flow rate through the top of the fluid domain, during a full cardiac cycle of 0.86 s, with $\Delta t = 1.0 \times 10^{-4}$ s and $\Delta t = 0.5 \times 10^{-4}$ s.

NIH-PA Author Manuscript

NIH-PA Author Manuscript

NIH-PA Author Manuscript

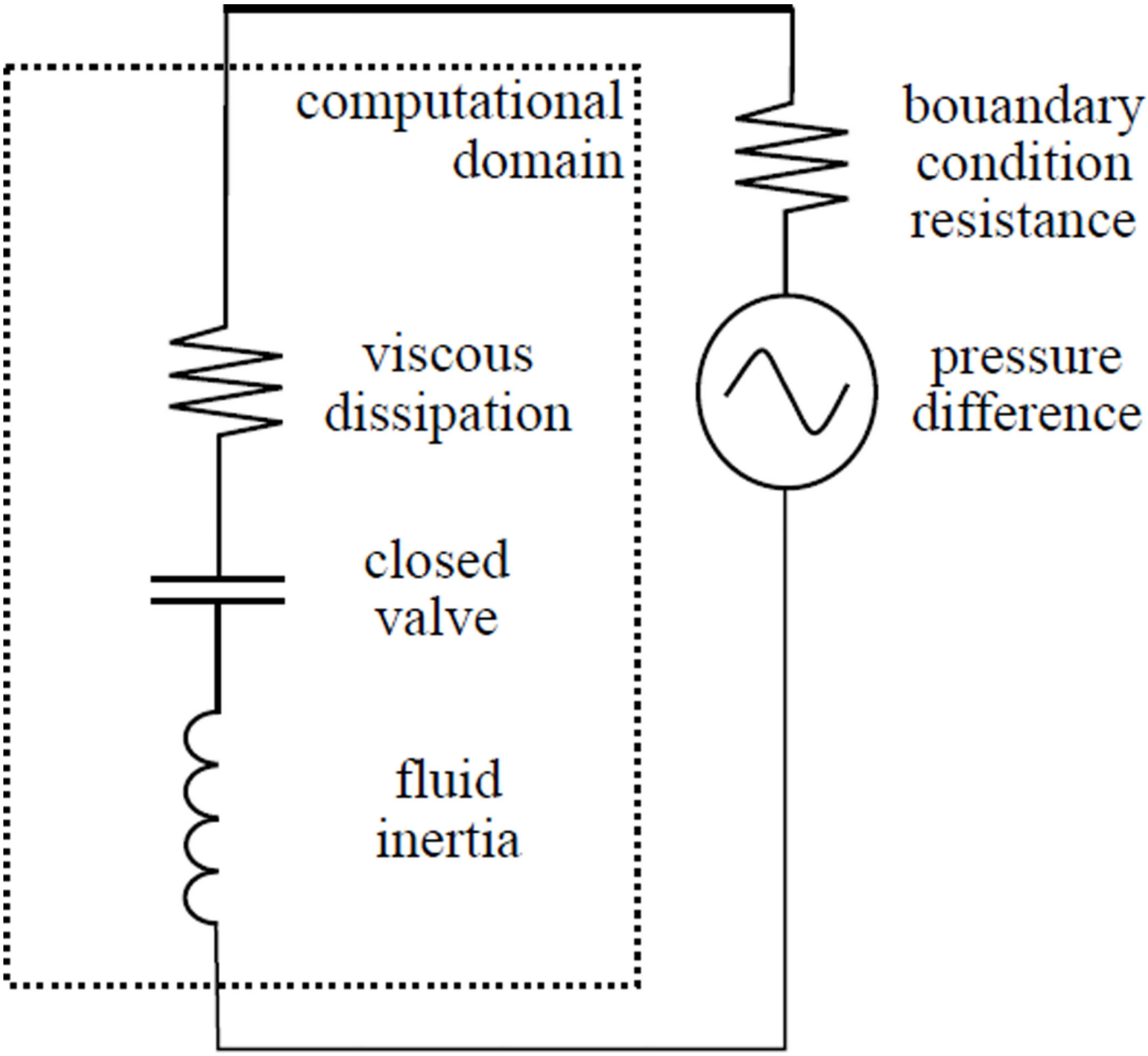

Figure 29.
The electrical circuit that is analogous to the valve model of this paper (when the valve is closed).

NIH-PA Author Manuscript

NIH-PA Author Manuscript

NIH-PA Author Manuscript

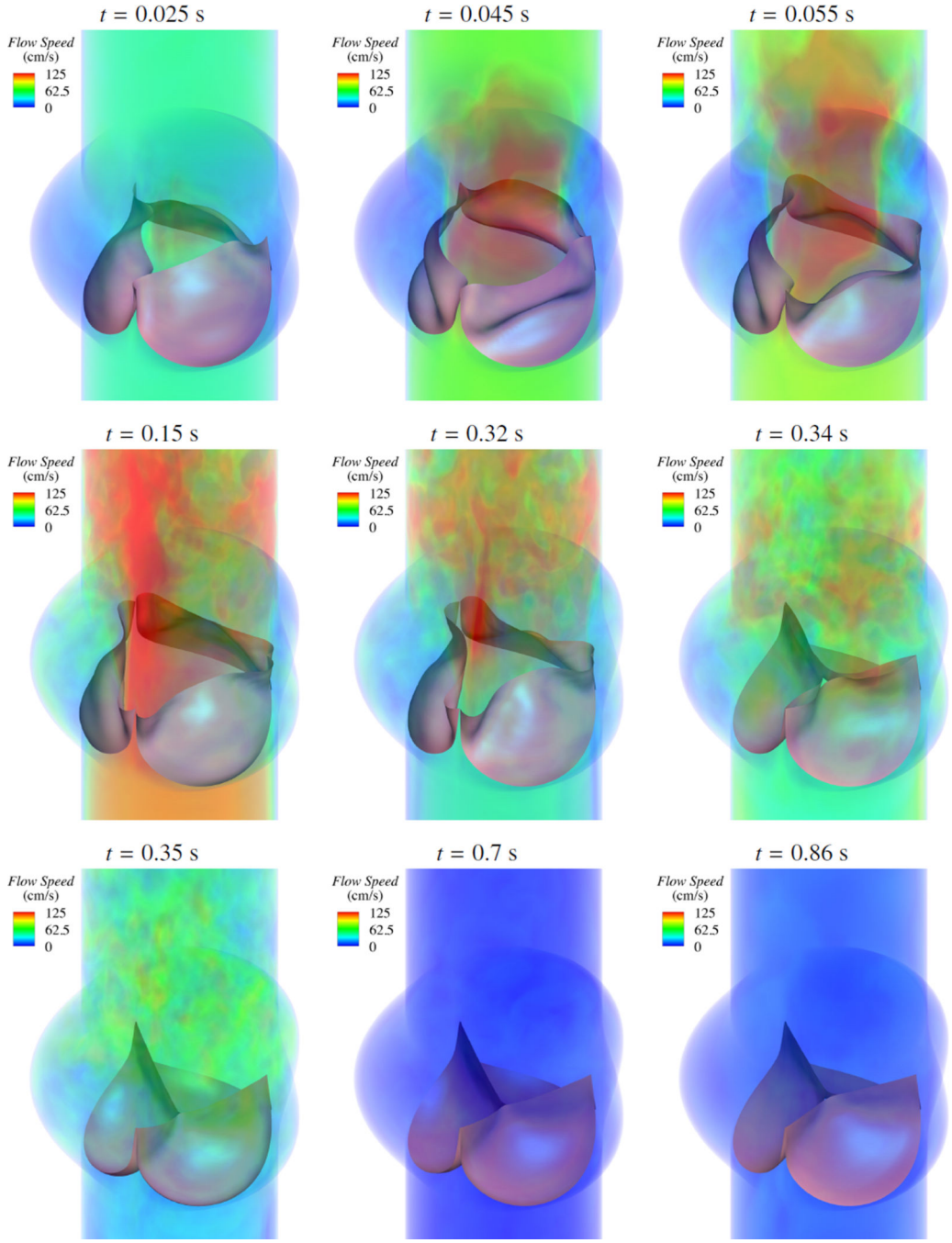

Figure 30.

Volume-renderings of the fluid velocity field at several points during a cardiac cycle. The time *t* is synchronized with Figure 27 for the current cycle.

NIH-PA Author Manuscript

NIH-PA Author Manuscript

NIH-PA Author Manuscript

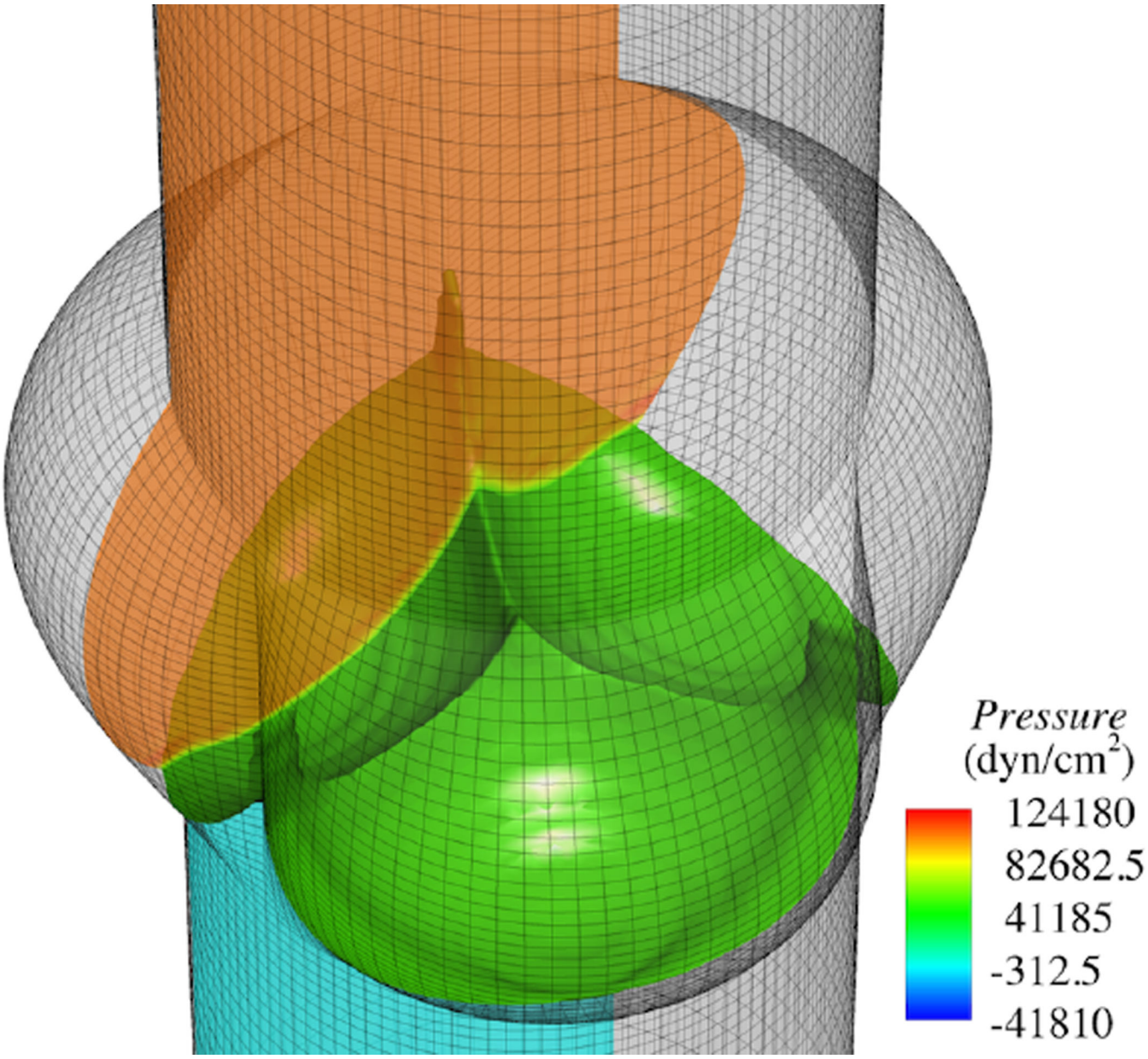

Figure 31.
Pressure at time $t = 0.7$ s, shown on a slice and with an iso-surface at $p = 40$ mmHg.

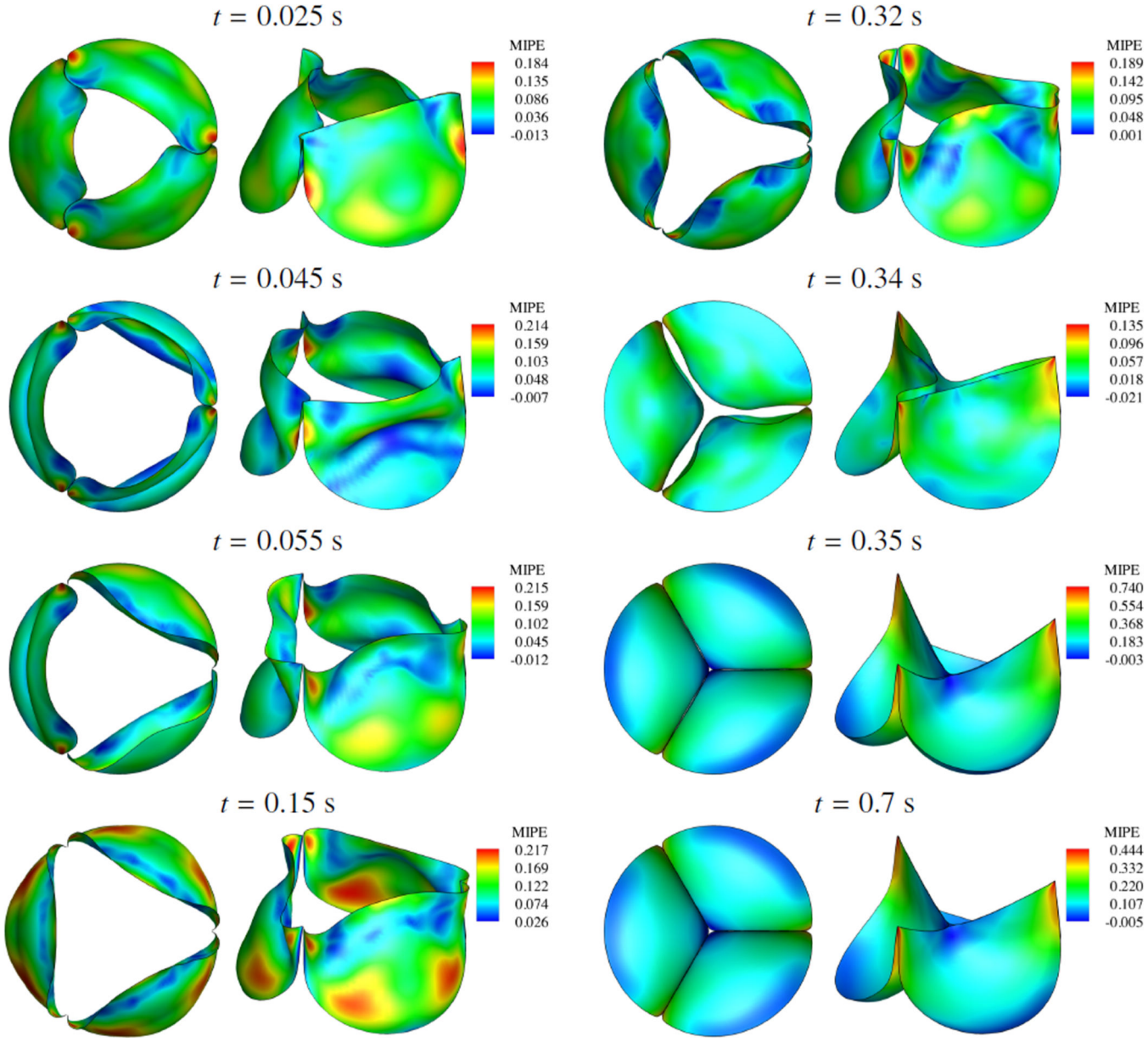

Figure 32.

Deformations of the valve from the FSI computation, colored by maximum in-plane principal Green-Lagrange strain (MIPE, the largest eigenvalue of **E**), evaluated on the aortic side of the leaflet. Note the different scale for each time.

NIH-PA Author Manuscript NIH-PA Author Manuscript NIH-PA Author Manuscript

NIH-PA Author Manuscript

NIH-PA Author Manuscript

NIH-PA Author Manuscript

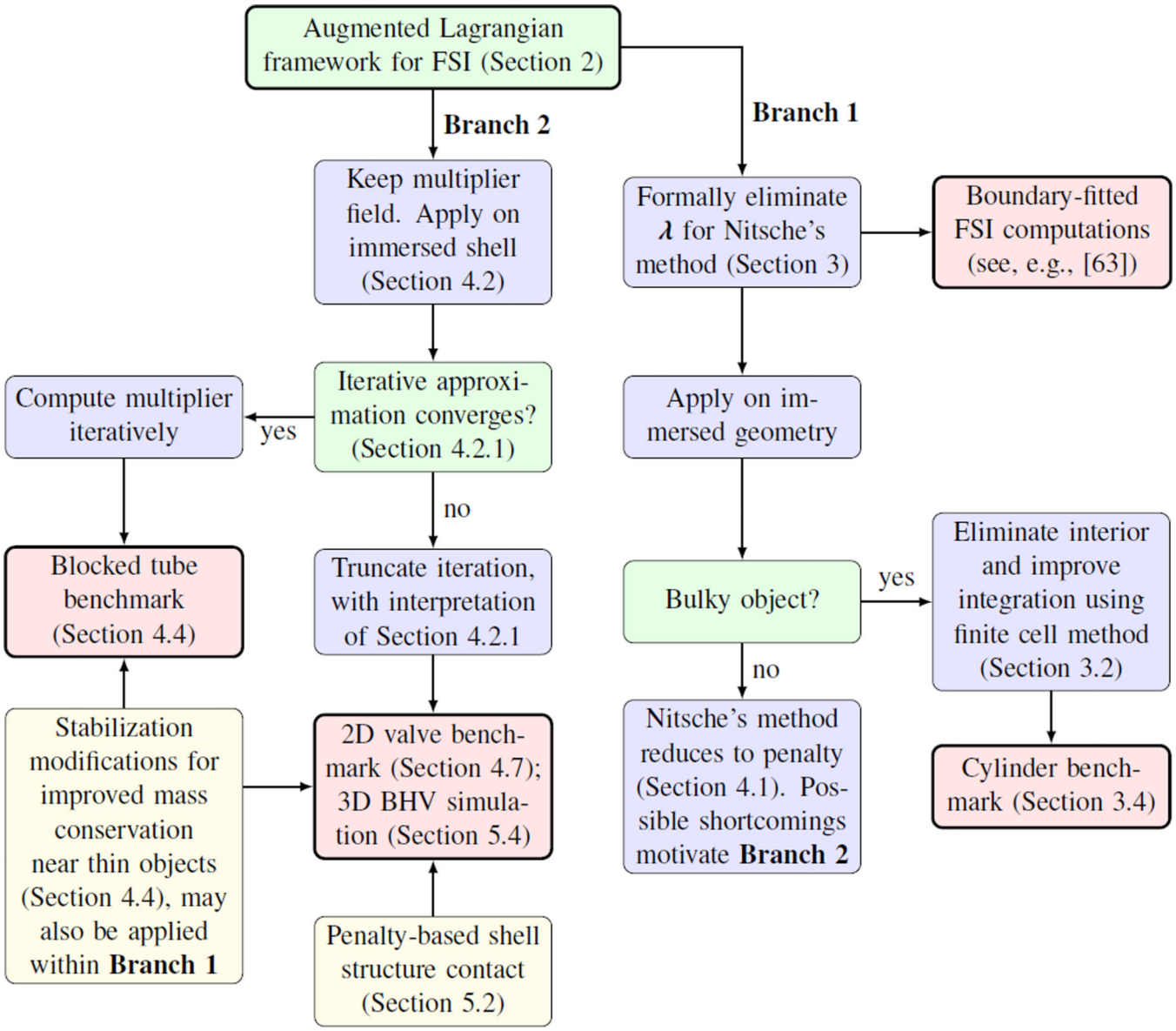

Figure 33.

A graphical map of the interrelated ideas, methods, and results of this paper. Arrows indicate conceptual flow from ideas to numerical methods to specific computations. Branch-points in this flow are highlighted in green and computations are highlighted in red.

NIH-PA Author Manuscript
NIH-PA Author Manuscript
NIH-PA Author Manuscript

Table 1

Comparison of quantities of interest with various penalty values and $l = 3$ levels of adaptive quadrature on mesh M1.

M1						
	$Re = 40$			$Re = 80$		
	C_D	L_W		C_D	C_L	St
$\tau^B = 10^2$	1.611	2.26		1.413	±0.252	0.159
$\tau^B = 10^3$	1.611	2.26		1.411	±0.250	0.159
Boundary-fitted	1.612	2.27		1.415	±0.254	0.159
	$Re = 100$			$Re = 200$		
	C_D	C_L	St	C_D	C_L	St
$\tau^B = 10^2$	1.384	±0.338	0.170	1.369	±0.694	0.200
$\tau^B = 10^3$	1.381	±0.336	0.171	1.369	±0.696	0.200
Boundary-fitted	1.386	±0.341	0.170	1.378	±0.706	0.200

Comput Methods Appl Mech Eng. Author manuscript; available in PMC 2016 February 01.

NIH-PA Author Manuscript
NIH-PA Author Manuscript
NIH-PA Author Manuscript

Table 2

Comparison of quantities of interest with various penalty values and $l = 3$ levels of adaptive quadrature on mesh M2.

M2						
	$Re = 40$			$Re = 80$		
	C_D	L_W		C_D	C_L	St
$\tau^B = 10^2$	1.612	2.27		1.415	±0.254	0.159
$\tau^B = 10^3$	1.612	2.27		1.415	±0.253	0.158
Boundary-fitted	1.612	2.27		1.415	±0.254	0.159
	$Re = 100$			$Re = 200$		
	C_D	C_L	St	C_D	C_L	St
$\tau^B = 10^2$	1.386	±0.341	0.170	1.378	±0.706	0.200
$\tau^B = 10^3$	1.386	±0.341	0.170	1.378	±0.705	0.200
Boundary-fitted	1.386	±0.341	0.170	1.378	±0.706	0.200

NIH-PA Author Manuscript
NIH-PA Author Manuscript
NIH-PA Author Manuscript

Table 3

Ranges of typical values of quantities of interest from the CFD literature [114–121]

	Re = 40			*Re* = 80		
	C_D	L_W		C_D	C_L	St
Literature	1.52–1.63	2.24–2.32		1.34–1.44	± 0.26	0.15–0.16
	Re = 100			*Re* = 200		
	C_D	C_L	St	C_D	C_L	St
Literature	1.33–1.43	± 0.30–0.34	0.16–0.17	1.31–1.45	±0.64–0.71	0.19–0.20

NIH-PA Author Manuscript NIH-PA Author Manuscript NIH-PA Author Manuscript

Table 4

Comparison of quantities of interest with penalty $\tau^B = 10^2$ and different levels, l, of adaptive quadrature. The $l = 3$ results are repeated from Table 2 for the reader's convenience.

M2						
	Re = 40			*Re* = 80		
	C_D	L_W		C_D	C_L	*St*
$l = 0$	1.620	2.31		1.473	±0.247	0.158
$l = 3$	1.612	2.27		1.415	±0.254	0.159
Boundary-fitted	1.612	2.27		1.415	±0.254	0.159
	Re = 100			*Re* = 200		
	C_D	C_L	*St*	C_D	C_L	*St*
$l = 0$	1.477	±0.335	0.169	1.613	±0.631	0.199
$l = 3$	1.386	±0.341	0.170	1.378	±0.706	0.200
Boundary-fitted	1.386	±0.341	0.170	1.378	±0.706	0.200

Comput Methods Appl Mech Eng. Author manuscript; available in PMC 2016 February 01.

NIH-PA Author Manuscript

NIH-PA Author Manuscript

NIH-PA Author Manuscript

Table 5

The effect of s^{shell} on apparent leakage due to volume loss.

s^{shell}	Volumetric flow rate
1	355.2 mL/s
10^4	4.037 mL/s
10^8	4.048×10^{-2} mL/s